

THERMAL MANAGEMENT OF FIBER-COUPLED-DIODE PUMPED  
Tm:YLF LASER CRYSTAL SLAB

A THESIS SUBMITTED TO  
THE GRADUATE SCHOOL OF NATURAL AND APPLIED SCIENCES  
OF  
MIDDLE EAST TECHNICAL UNIVERSITY

BY

MERT BALTACIOĞLU

IN PARTIAL FULFILLMENT OF THE REQUIREMENTS  
FOR  
THE DEGREE OF MASTER OF SCIENCE  
IN  
MECHANICAL ENGINEERING

NOVEMBER 2014



Approval of the thesis:

**THERMAL MANAGEMENT OF FIBER-COUPLED-DIODE PUMPED  
Tm:YLF LASER CRYSTAL SLAB**

submitted by **MERT BALTACIOĞLU** in partial fulfillment of the requirements  
for the degree of **Master of Science in Mechanical Engineering Department,**  
**Middle East Technical University** by,

Prof. Dr. Gülbin Dural Ünver  
Dean, Graduate School of **Natural and Applied Sciences**

\_\_\_\_\_

Prof. Dr. Tuna Balkan  
Head of Department, **Mechanical Engineering**

\_\_\_\_\_

Assoc. Prof. Dr. Tuba Okutucu Özyurt  
Supervisor, **Mechanical Engineering Dept., METU**

\_\_\_\_\_

**Examining Committee Members:**

Prof. Dr. Zafer Dursunkaya  
Mechanical Engineering Dept., METU

\_\_\_\_\_

Assoc. Prof. Dr. Tuba Okutucu Özyurt  
Mechanical Engineering Dept., METU

\_\_\_\_\_

Asst. Prof. Dr. Cüneyt Sert  
Mechanical Engineering Dept., METU

\_\_\_\_\_

Asst. Prof. Dr. Özgür Bayer  
Mechanical Engineering Dept., METU

\_\_\_\_\_

Dr. Oktay Onur Kuzucu  
ASELSAN

\_\_\_\_\_

**Date:** 07.11.2014

**I hereby declare that all information in this document has been obtained and presented in accordance with academic rules and ethical conduct. I also declare that, as required by these rules and conduct, I have fully cited and referenced all material and results that are not original to this work.**

Name, Last Name: Mert Baltacıođlu

Signature :

## ABSTRACT

### **THERMAL MANAGEMENT OF FIBER-COUPLED-DIODE PUMPED Tm:YLF LASER CRYSTAL SLAB**

Baltacıoğlu, Mert  
M.S., Department of Mechanical Engineering  
Supervisor : Assoc Prof. Dr. Tuba Okutucu Özyurt

November 2014, 142 pages

In end-pumped solid-state lasers, thermal effects in the lasing medium are important factors in determining the limits of the maximum achievable power and the laser beam quality. In the present study, thermal effects such as the maximum and average temperatures, thermal lens radius and thermally induced stress on a fiber-coupled-diode pumped Thulium(Tm)-doped-YLiF<sub>4</sub>(YLF) laser crystal slab with unity aspect ratio are investigated for different cooling geometries. The thermal effects are simulated and compared for the laser crystal slab pumped by Gaussian and top-hat incident pump profiles with one side surface, two parallel opposite side surfaces and all four side surfaces being used as the heat dissipating surfaces. The case with four heat dissipating side surfaces yielded significantly better results in terms of thermo-optical effects compared to those of the other two cooling cases. Also the top-hat pump profile outperformed the Gaussian profile in all cooling conditions. The introduction of crystal holders with different thermal conductivities on the steady-state thermal and thermo-optical performance of the slab is also investigated for all cooling cases. It is observed that the crystal holder acts as a constant steady-state conductive thermal resistance throughout the length of the crystal. Simulations favored the asymmetrically cooled 4-side cooling method. Accordingly, setups using two-stage holders are designed and experimented. The experimental data is found to be in agreement with the simulations.

Keywords: Double-End-Pumped Laser Crystal Slab, Thermo-Optical Effects in Solid-State Lasers, Laser Crystal Slab, Thermal Lens, Cooling Optical Devices

## ÖZ

### FİBER-AKUPLE-DİYOT POMPALI Tm:YLF LAZER KRİSTAL BLOĞUNUN ISIL YÖNETİMİ

Baltacıođlu, Mert  
Yüksek Lisans, Makina Mühendisliđi Bölümü  
Tez yöneticisi : Doç. Dr. Tuba Okutucu Özyurt

Kasım 2014, 142 sayfa

Sondan pompalı katı-hal lazerlerinde kristal içi ısıl etkiler, azami lazer çıkış gücü ve ışın kalitesini sınırlayan önemli etkilerdendir. Bu çalışmada, fiber-akuple-di-yot pompalı Thulium(Tm)-katkılı-YLiF<sub>4</sub>(YLF) lazer kristal bloğunun azami ve ortalama kristal sıcaklıkları, ısıl mercek yarıçapı ve ısıl kaynaklı stres oluşumu gibi ısıl etkileri, farklı soğutma geometrileri için incelenmiştir. Lazer kristali üzerindeki ısıl etkiler, Gauss ve “top-hat” pompa profilleri ile tek yan yüzey, iki karşılıklı paralel yan yüzey ve dört yan yüzeyin ısı atma yüzeyi olarak kullanılma durumları için benzetimlenerek karşılaştırılmıştır. Dört yan yüzeyin ısı atma yüzeyi olarak kullanılma durumu diğer iki duruma göre kristalin ısıl ve ısıl-optik özelliklerinde önemli ölçüde iyileştirme sağlamıştır. Aynı şekilde Gauss profilli ısı üretimi, “top-hat” ısı üretim profiline göre, tüm soğutma durumlarında daha iyi ısıl ve ısıl-optik performans göstermiştir. Isıl problemde, lazer kristalinin yanı sıra kristal tutucuların da sisteme katılmasının, sisteme yalnızca kristal uzunluğu boyunca sabit, kararlı hal iletimsel ısıl direncinin eklenmesi olarak etki ettiği görülmüştür. Lazer kristal tutuculu sistemler aynı şekilde tüm soğutma koşullarında ısıl ve ısıl-optik özellikleri benzetimlenip karşılaştırılmıştır. Tüm benzetim sonuçları ele alındığında, dört yan yüzey soğutmasının, alternatiflerine göre daha iyi sonuçlar verdiği görülmüş ve bu sisteme uygun deneysel düzenek tasarlanıp uygulanmıştır. Deneysel sonuçların, benzetim sonuçları ile uyduğu görülmektedir.

Anahtar Kelimeler: Çift-Sondan-Pompalı Lazer Kristal Blođu, Katı-Hal Lazerlerinde Termo-Optik Etkiler, Lazer Kristal Blođu, Termal Mercek, Optik Cihaz Soğutma

*To my family...*

## ACKNOWLEDGEMENTS

I am deeply grateful to my advisor Assoc.Prof.Dr. Tuba Okutucu Özyurt for her informative guidance, advice and understanding throughout the study. I appreciate her steadfast encouragement and boundless help for making this dissertation possible.

I would like to particularly acknowledge the invaluable contribution and inspiring suggestions of Dr. Oktay Onur Kuzucu.

I am thankful to my superior Murat Şahin for his original ideas, guidance and mentoring.

I would like to thank my colleagues Kubilay Sezgin for his help in OPD calculations and for ZEMAX analyses, Yüksel Yüksel for his support on TEC implementation, and Dr. Kuthan Yelen for his mentoring in thermo-optical effects.

I am indebted to my previous manager Birol Erentürk and current manager Atakan Dura for their understanding and inspiring ideas throughout the study. I want to thank also all my colleagues in ASELSAN Inc. MGEO Division for providing a pleasant and productive working atmosphere.

I would like to state my deepest gratitude to all the members of my family for their infinite support and to Aysel Yasemin Göl who encouraged me for completing the study and making life enjoyable.

Finally, I am very thankful to ASELSAN Inc. MGEO Division for providing the experimental setups and computational facilities.

## TABLE OF CONTENTS

ABSTRACT .....	v
ÖZ.....	vi
ACKNOWLEDGEMENTS .....	viii
TABLE OF CONTENTS .....	ix
LIST OF TABLES .....	xii
LIST OF FIGURES.....	xiii
ABBREVIATIONS.....	xix
CHAPTERS	
1. INTRODUCTION.....	1
1.1. Objectives and Challenges of the Present Study .....	1
1.2. Working Principle of Lasers and the Need for Their Cooling.....	2
1.3. Laser Crystal Material, Geometry and Pumping Structures in Solid-State Lasers.....	9
1.4. Thermal Effects in Solid-State Lasers .....	11
1.5. Literature Survey .....	14
1.6. Outline of the Thesis.....	17
2. SYSTEM CONFIGURATION AND HEAT LOAD CALCULATIONS ...	19
2.1. Configuration of the Laser Resonator.....	19

2.2. Calculation of Heat Generation in the Laser Slab .....	21
2.3. Conceptual Design of Laser Crystal Slab Holders .....	27
3. VALIDATION OF THE FINITE ELEMENT MODEL AND THE THERMAL SIMULATIONS OF THE LASER CRYSTAL SLAB.....	33
3.1. Analytical Thermal Model to Validate the Finite Element Model .....	34
3.2. ANSYS Workbench Finite Element Model of Laser Crystal Slab.....	40
3.3. Temperature Dependent Optical Path Difference (OPD) and Calculation of the Thermal Lens Radius .....	46
3.4. Comparison of the Analytical and Finite Element Solutions for the 4-Face Cooling Case and Validation of the Finite Element Model .....	49
3.5. Comparison of the Temperature Distribution for Different Cooling Geometries of the Laser Crystal Slab.....	54
4. LASER CRYSTAL HOLDER GEOMETRIES AND FINITE ELEMENT ANALYSIS OF THE COMPOSITE SYSTEM .....	61
4.1. 1-Side Contact Laser Crystal Slab Holder System .....	62
4.2. 2-Side Contact Laser Crystal Slab Holder System .....	68
4.3. 4-Side Contact Laser Crystal Holder Slab.....	72
4.4. The Effects of the Holder Geometry and the Material on 4-Side Contact Cooling.....	77
5. DESIGN AND CONSTRUCTION OF THE EXPERIMENTAL SETUP AND THE MEASUREMENTS.....	83
5.1. Design of the TEC Experimental Setup.....	83

5.2. Design of the Water-Cooled Experimental Setup .....	88
5.3. Assembly and the Components of the TEC Experimental System .....	92
5.4. Experimental Results from the TEC Setup.....	99
5.4.1. Experimental Data.....	99
5.4.2. Experimental Heat Load Determination .....	103
5.4.3. Laser Beam Profile.....	106
5.5. Problems Encountered in the Water Cooled Experimental Setup .....	112
6. CONCLUSIONS AND FUTURE RECOMMENDATIONS .....	115
6.1. Summary and Conclusions .....	115
6.2. Future Recommendations .....	119
REFERENCES .....	121
APPENDICES	
A- DATA SHEET OF DIODE PUMPS.....	131
B- INCOHERENT IRRADIANCE PLOTTED IN THE X-AXIS.....	132
C- MATLAB CODE FOR THE ANALYTICAL SOLUTION.....	135
D- SAMPLE CALCULATION OF THE EXPERIMENTAL RESULTS.....	136
E- EXPERIMENTAL ERROR ANALYSIS .....	139

## LIST OF TABLES

Table 3.1 Volumetric Heat Generation Values Used in the Finite Element Model with Gaussian Distribution. ....	44
Table 3.2 Comparison of the Single Crystal Cooling Cases .....	57
Table 4.1 The Mean Values of the Temperature Profile Differences Between 1-Side Contact Crystal Holder and Single Crystal with the Average Deviations .....	65
Table 4.2 The Mean Values of the Temperature Profile Differences Between 2-Side Contact Crystal Holder and Single Crystal with Average Deviations .....	71
Table 4.3 The Mean Values of the Temperature Profile Differences Between 4-Side Contact Crystal Holder and Single Crystal with Average Deviations .....	75
Table 5.1 Measurements from the Symmetrically Cooled TEC Setup .....	100
Table 5.2 Measurements from the Asymmetrically Cooled TEC Setup .....	100
Table 5.3 Results of Asymmetrical Cooling Experiments .....	104
Table 5.4 Laser Beam Profile Data for 25 A Diode Supply Current .....	110
Table D.1 Current and Discharged Heat Data for the TEC at 31°C Temperature Difference .....	138
Table E.1 Temperature Measurement Errors in Asymmetrical Cooling Experiments.....	140
Table E.2 Uncertainty in the Results of Asymmetrical Cooling Experiments.....	142

## LIST OF FIGURES

Figure 1.1 Absorption, Spontaneous and Stimulated Emission [1] .....	3
Figure 1.2 Amplification by Stimulated Emission [1] .....	5
Figure 1.3 Production of the Laser Beam [2] .....	7
Figure 1.4 Electron Transitions in Four-Level Laser Pumping System.....	8
Figure 1.5 Laser System Representations: (a) End-Pumped Disk Laser (b) Side-Pumped Slab Laser (c) End-Pumped Rod Laser (d) End- Pumped Slab Laser. ....	11
Figure 1.6 Lensing Effect effect in a Media with a Parabolic Variation of Refractive Index in the $x$ -axis [16] .....	12
Figure 1.7 Deformation Occurring at the End-Surface of the End-Pumped Laser Crystal Slab.....	13
Figure 2.1 The Layout of Tm:YLF Laser System Cavity .....	20
Figure 2.2 The Geometry of Tm:YLF Laser Crystal Slab and Pumped Region.....	20
Figure 2.3 The Heat Generation Through Fast-Axis of the 4% Tm:YLF Laser Slab with Double End-Pumping. ....	23
Figure 2.4 The Pump Illumination Profile on the Laser Crystal at the End Surfaces $z = 0$ and 12 mm.....	24
Figure 2.5 The Pump Illumination Profile on the Laser Crystal Slab at $z =$ 2 mm and 10 mm .....	25
Figure 2.6 The Pump Illumination Profile on the Laser Crystal Slab at $z =$ 4 mm and 8 mm .....	25
Figure 2.7 The Pump Illumination Profile on the Laser Crystal Slab at the Middle Surface, $z = 6$ mm.....	26
Figure 2.8 Different Cooling Configurations in End-Pumped System of Nd:YAG [51] .....	28

Figure 2.9 The Conceptual Holders for the Laser Slab Side-Contact Cooling.....	29
Figure 2.10 The Conceptual Holders for the Laser Slab with 4-Side-Contact Cooling .....	32
Figure 3.1 The Illustration of the Analytical Solution Domain for the (a) Full domain and (b) Quarter Domain. ....	38
Figure 3.2 Continuous and Discretized Heat Generation Through Fast-Axis (Z-Axis).....	41
Figure 3.3 Discretized Elements in $z$ -Direction. ....	41
Figure 3.4 Discretized Elements in $xy$ -Plane, $r$ -Direction.....	42
Figure 3.5 Continuous and Discretized Heat Generation in $xy$ -Plane .....	43
Figure 3.6 The Mesh Structure Used in Laser Crystal Slab for Gaussian Heat Generation. ....	45
Figure 3.7 Paths and Mapping Used to Determine the Temperature Profiles in the Laser Crystal Slab. ....	50
Figure 3.8 Comparison of Temperature Profiles Obtained from Analytical and Finite Element Solutions .....	51
Figure 3.9 Analytically Obtained Vertical OPD Profile for the 4-Face Laser Crystal Slab Cooling. ....	51
Figure 3.10 Analytically Obtained Horizontal OPD Profile for the 4-Face Laser Crystal Slab Cooling. ....	52
Figure 3.11 Vertical OPD Profile Obtained by FEM for the 4-Face Laser Crystal Slab Cooling. ....	52
Figure 3.12 Horizontal OPD Profile Obtained by FEM for the 4-Face Laser Crystal Slab Cooling. ....	53
Figure 3.13 Illustration of (a) 1-Face, (b) 2-Face, and (c) 4-Face Cooling Geometries .....	55
Figure 3.14 End Surface Temperature Profiles for the 1-Face Cooling Case with (a) Gaussian and (b) Uniform Heat Generation Profile.....	55
Figure 3.15 End Surface Temperature Profiles for the 2-Face Cooling Case with (a) Gaussian and (b) Uniform Heat Generation Profile.....	56

Figure 3.16 End Surface Temperature Profiles for the 4-Face Cooling Case with (a) Gaussian and (b) Uniform Heat Generation Profile.....	56
Figure 4.1 Geometry of the 1-Face Cooling Case and the Corresponding 1-Side Contact Cooling Case. ....	62
Figure 4.2 Comparison of the End Surface Temperature Profiles for 1-Side Cooled Crystal with Al and Cu Holders, and 1-Face Cooled Crystal.....	63
Figure 4.3 Comparison of the Middle Surface Temperature Profiles for 1-Side Cooled Crystal with Al and Cu Holders, and 1-Face Cooled Crystal.....	64
Figure 4.4 Heat Transfer Region in the 1-Side Contact Crystal Holder .....	66
Figure 4.5 2-Face Cooling Geometry and the Corresponding 2-Side Cooling Geometry.....	69
Figure 4.6 Comparison of the End Surface Temperature Profiles for 2-Side Cooled Crystal with Al and Cu Holders, and 2-Face Cooled Crystal.....	69
Figure 4.7 Comparison of the Middle Surface Temperature Profiles for 2-Side Cooled Crystal with Al and Cu Holders, and 2-Face Cooled Crystal.....	70
Figure 4.8 4-Face Cooling Geometry and the Corresponding 4-Side Symmetrical Cooling Geometry .....	73
Figure 4.9 Comparison of the End Surface Temperature Profiles: 4-Side Cooled Crystal with Al and Cu Holders, 4-Face Cooled Crystal .....	73
Figure 4.10 Comparison of the Middle Surface Temperature Profiles: 4-Side Cooled Crystal with Al and Cu Holders, 4-Face Cooled Crystal.....	74
Figure 4.11 Dimensional Variables of 4-Side Contact Holder Used in the Analysis. ....	77
Figure 4.12 Variation of the Maximum Temperature Difference in the Laser Slab with the Half-Width for 4-Side Contact Holders.....	78

Figure 4.13 Variation of the Average Temperature Difference in the Laser Slab with the Half-Width for 4-Side Contact Holders.....	79
Figure 4.14 Heat Transfer Region in One of the 4-Side Contact Crystal Holder for the Symmetric Cooling Case.....	81
Figure 5.1 The Cavity Design of the Double-End-Pumped Tm:YLF System.....	84
Figure 5.2 Experimental Laser Crystal Holder Design for the Thermoelectric Cooling .....	85
Figure 5.3 Comparison of the Numerical and Experimental Results for the End Surface Temperature Profiles: 4-Side Asymmetrically Cooled Crystal with Al and Cu Holders, 4-Face Cooled Crystal .....	87
Figure 5.4 Experimental Laser Crystal Holder Design for Water Cooling.....	88
Figure 5.5 Crystal Holders for the Water Cooling Setup and the Path of the Cooling Water.....	89
Figure 5.6 Comparison of the Numerically Obtained End Surface Temperature Profiles for the Water Cooled and Thermoelectrically Cooled Experimental Setups with 4-Face Cooling.....	92
Figure 5.7 The Components of the Laser Crystal Holder Assembly for Thermoelectric Cooling Setup .....	93
Figure 5.8 Tm:YLF Laser Crystal Slab Wrapped in Indium TIM .....	94
Figure 5.9 The Assembly of the First-Stage Holders.....	94
Figure 5.10 The Assembled Crystal Holders .....	95
Figure 5.11 Experimental Setup for the Asymmetrical Thermoelectric Cooling System.....	96
Figure 5.12 Experimental Setup for the Symmetrical Thermoelectrically Cooled System .....	97
Figure 5.13 793 nm Pump Diodes.....	98
Figure 5.14 Thermal Imaging Camera and the Experimental Setup .....	98
Figure 5.15 The Performance Curves of UT9-12-F2-3030 TEC by Laird [60].....	105

Figure 5.16 Setup for Obtaining the Laser Beam Profile.....	106
Figure 5.17 Rectangular Traverse Mode Patterns, TEM <sub>mn</sub> [61].....	107
Figure 5.18 Laser Beam Profile for Asymmetrical Cooling with 25 A Diode Supply Current .....	108
Figure 5.19 Laser Beam Profile for Symmetrical Cooling with 25 A Diode Supply Current .....	109
Figure 5.20 Moving-Slit Beam Width Analysis [62] .....	111
Figure B.1 Incoherent Irradiance on Laser Crystal at the End Surfaces, $z =$ 0 and 12 mm .....	132
Figure B.2 Incoherent Irradiance on Laser Crystal at $z = 2$ mm and 10 mm ....	133
Figure B.3 Incoherent Irradiance on Laser Crystal at $z = 4$ mm and 8 mm .....	133
Figure B.4 Incoherent Irradiance on Laser Crystal at the Middle Surface $z$ $= 6$ mm .....	134

## SYMBOLS

$k$	Thermal conductivity [W/(m·K)]
$\eta$	Quantum yield
$\alpha_\lambda$	Wavelength dependent absorption coefficient [cm <sup>-1</sup> ]
$n$	Refractive index
$\alpha$	Coefficient of thermal expansion (CTE) [K <sup>-1</sup> ]
$dn/dT$	Temperature coefficient of refractive index [K <sup>-1</sup> ]
$\lambda$	Wavelength [nm]
$c_p$	Specific heat at constant pressure [kJ/(kg·K)]
$\rho$	Density [kg/m <sup>3</sup> ]
$Re_D$	Reynolds number
$k_s$	Surface roughness [μm]
$f$	Friction factor
$Nu_D$	Nusselt number
$Pr$	Prandtl number
$h$	Convective heat transfer coefficient [W/(m <sup>2</sup> ·K)]

## ABBREVIATIONS

Tm:YLF	Thulium-Doped Yttrium Lithium Fluoride
TEC	Thermo-Electric Cooling/Cooler
FEM	Finite Element Method
HR	High Reflective
PR	Partial Reflective
YAG	Yttrium Aluminum Garnet
YLF	Yttrium Lithium Fluoride
YALO	Yttrium Orthoaluminate
LuAG	Lutetium Aluminum Garnet
OPD	Optical Path Difference
Ho:YAG	Holmium-Doped Yttrium Aluminum Garnet
CW	Continuous-Wave
SMA	Sub Miniature A Type Fiber Connector
AR	Anti-Reflection
ZEMAX	Optical design and analysis software
Nd:YAG	Neodymium-Doped Yttrium Aluminum Garnet
TIM	Thermal Interface Material

ANSYS	Engineering simulation software
CTE	Coefficient of Thermal Expansion
MATLAB	Programming environment for algorithm development and numerical computation
HEPA	High Efficiency Particulate Air

# CHAPTER 1

## INTRODUCTION

### 1.1. Objectives and Challenges of the Present Study

The primary objective of the present work is to develop an active cooling system for a fiber-coupled-diode, double end-pumped, 1908 nm wavelength Thulium(Tm)-doped-YLiF<sub>4</sub>(YLF) laser system. The laser system has been designed to operate at a broad temperature range in a commercial laser device, but the scope of this study only consists of the laboratory setup that is to be operated at room-temperature conditions. Thermo-electric cooling (TEC) has been selected as the active cooling method; also a water cooling module has been designed and constructed to compare the expected differences in the laser performance as well as to explore the similarities between these two active cooling methods. This study focuses on the effects of cooling geometries on a square cross-sectioned double end-pumped laser crystal slab and the effects of the crystal holder on the steady-state thermal performance.

End-pumping is one of the optical pumping techniques, where the pumping beam is injected into the laser gain medium along the product laser beam. The common procedure in analytical solutions is to consider the thermal management of the laser crystal slab only by applying the boundary conditions on the cooling surfaces.

In the present study, the mentioned analytical procedure has been repeated and the results have been compared with those obtained for a composite structure with boundary conditions applied on the crystal holder in contact with the

crystal. For the same heat load, the thermal effects of Gaussian and uniform pumping have been investigated.

Due to the nature and the architecture of the laser system in this study, very high volumetric heat generation occurs in the laser crystal. This excess heat must be effectively discharged from the system for stable operation.

Cooling methods and cooling geometries also have effect on the beam quality of the lasers. Inhomogeneous temperature distributions in the laser crystal, causes adverse effects on laser beam quality. These effects should be minimized for better laser quality. Also, estimation of these effects may provide useful and can be countered by optical components.

In the present study, several design alternatives have been developed and analyzed by analytical means and by FEM solutions in order to find the best cooling geometry. For an end-pumped laser crystal slab, four side surfaces are available for the heat discharge. One face, two opposite faces and all four faces have been considered for the heat discharge both with and without holders.

## **1.2. Working Principle of Lasers and the Need for Their Cooling**

The term “laser” is an acronym for Light Amplification by Stimulated Emission of Radiation. The theory behind the laser operation is actually explained by the meanings of these terms, and to comprehend the theory of the laser, one must first understand the meaning and the involved physical mechanisms implied by these terms. Figure 1.1 shows the term “stimulated emission” by explaining both absorption and spontaneous emission in atomic scale using Bohr atom model.

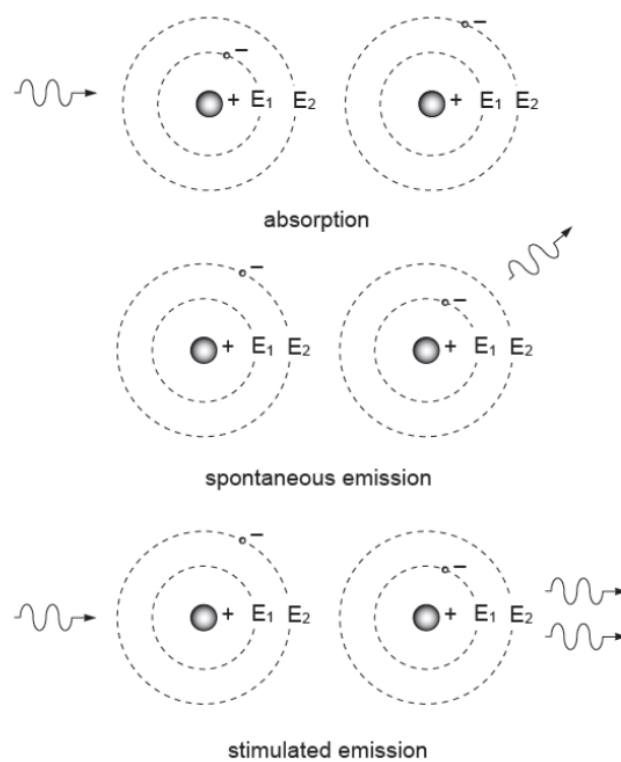


Figure 1.1 Absorption, Spontaneous and Stimulated Emission [1]

For the absorption of an incoming photon to occur, the photon should have a certain energy which is equal to the energy required by the electron to move to a higher discrete energy level from the current energy level. Likewise, spontaneous emission can occur when an excited electron at a higher energy level decays to a lower energy level. For this case the emitted photon has a certain energy that is equal to the energy difference between the two discrete energy levels in electron's decay path. A photon with a certain energy means, it has a certain wavelength, a certain color. This can be observed by equation 1.1 which gives the relation of intrinsic photon energy  $E$  as:

$$E = h\nu = hc/\lambda \tag{1.1}$$

where  $h$  is Planck's constant,  $\nu$ ,  $c$  and  $\lambda$  are the frequency, speed and wavelength of the light, respectively.

For the stimulated emission, a specific type of emission, to occur, the already excited atom, just as the one in the spontaneous emission case, must be stimulated by an incident photon that has a certain energy. The energy of the incident photon must be equal to the energy difference between discrete energy levels in the excited electron's decay path. This incident photon initiates the decay of the excited electron and therefore the emission of a new photon. The newly emitted photon is bound to have the same energy (wavelength) as the incident photon, since it is the prerequisite of the stimulated emission and it is also in the same direction of the incident photon.

The amplification by stimulated emission occurs when the prerequisites for the stimulated emission are met throughout a medium. These prerequisites can be classified as the requirement of the incident photon and atoms with excited electrons in correct energy levels. A population inversion in the system is required so that the population of atoms in the required excited state is larger than the population in lower states. To demonstrate stimulated emission, assume a very long relaxation time so that no spontaneous emission occurs in the media and there is 100% probability for the stimulated emission, when passing, the stimulating photon enters the media and interacts with the first excited atom to initiate stimulated emission, which produces an additional photon with the same wavelength, direction and phase. These two photons also initiate stimulated emission with different excited atoms in the media and produce two additional atoms with the same properties. This process goes on throughout the media and the first stimulating photon is amplified. Figure 1.2 shows the amplification by the stimulated emission.

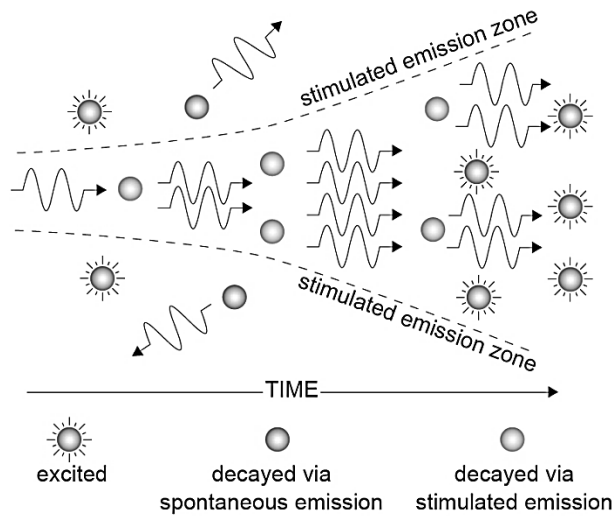


Figure 1.2 Amplification by Stimulated Emission [1]

Due to the nature of the stimulated emission, the product photons of the amplification process have the same wavelength, phase and direction of the stimulating photon. Hence, laser light is monochromatic, coherent and collimated. It should be noted that the spatial mode properties are not due to stimulated emission, but they are dictated by the spatial mode of the laser cavity. Altogether, it is for the mentioned properties that lasers have a wide range of applications.

The case shown in Figure 1.2 represents a single-pass gain of a photon through a medium. Since single-pass gains are usually not enough to generate a laser beam due to the fact that most of the excited atoms decay via spontaneous emission, a resonator structure is required. A resonator structure consists of a two mirror system. Two mirrors reflect undesired photons out of the system while reflecting the desired photons back into the system to be further amplified [1].

Figure 1.3 shows the generation and the basic components required by a laser. The resonator consists of a lasing medium (also called gain medium) in between the two mirrors, one of which is highly reflective (HR) and the other is partially

reflective (PR). Atoms in the lasing medium are excited using a pumping mechanism, and spontaneous emissions take place in all directions in the lasing medium. The spontaneous emissions initiate the stimulated emissions again in all directions in the laser medium. Due to the orientation of the HR and PR mirrors, off-axis generated photons are scattered out of the system not benefiting from the resonant feedback. Only on-axis photons experience the gain due to stimulated emissions along the axis of the mirrors. The PR mirror partially transmits light as usable laser beam to the external environment.

The need for the thermal management of laser systems can be emphasized by explaining the discrete energy levels of atoms. The real situation is more complex and the atom has more energy levels than it is represented in Figure 1.1. Considering a four-level laser pumping system shown in Figure 1.4, the absorption of the pump energy excites an electron from the ground level  $E_0$  to a higher energy level  $E_3$ . The electron then quickly decays to a lower metastable energy level  $E_2$  by releasing heat via electron-phonon scattering. The radiative decay process which results in the emission of a photon occurs between energy levels  $E_2$  and  $E_1$ . The reason for choosing that particular energy level is because of the long transition lifetime. This transition occurs relatively slower than the other transitions so that the population of the excited atoms ready to participate in stimulated emissions can be large. This phenomenon is called population inversion.

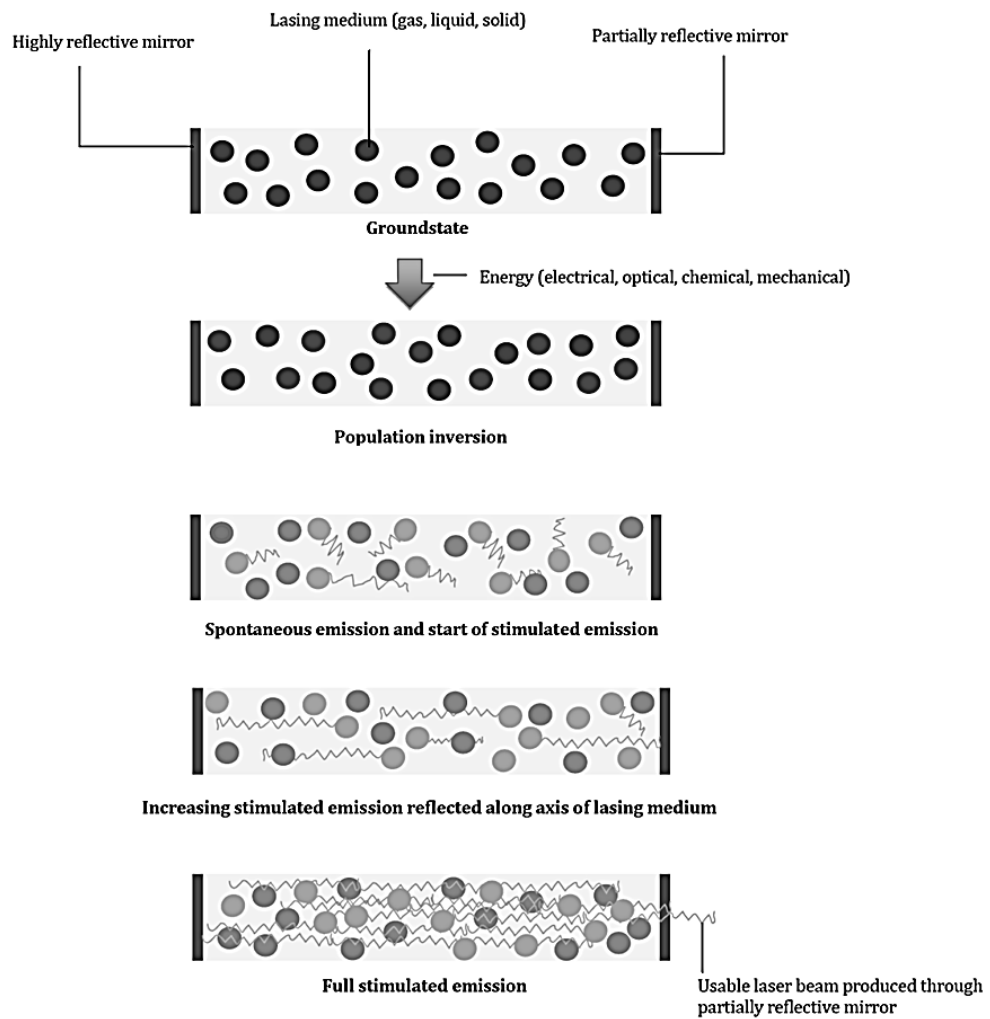


Figure 1.3 Production of the Laser Beam [2]

After the emission, the electron in energy state  $E_1$  quickly decays to ground level by discharging heat, just as that in the decay path from  $E_3$  to  $E_2$ . This is another reason why a population inversion can be achieved. If the transition time from  $E_1$  to  $E_0$  were too long, one could never maintain a population inversion. The absorption (pumping) and the energy level transitions of electrons are illustrated in Figure 1.4.

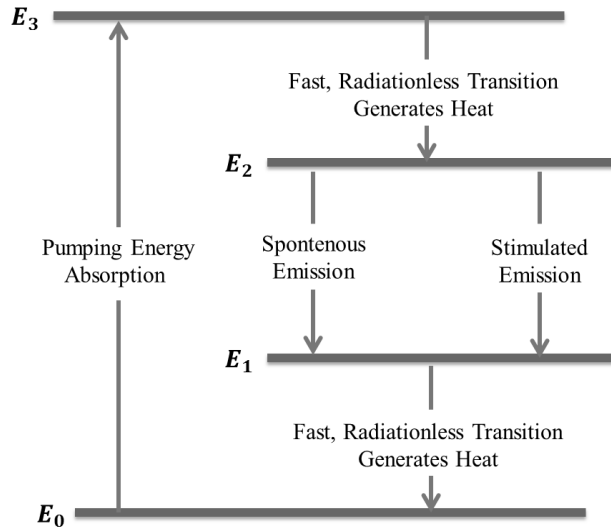


Figure 1.4 Electron Transitions in Four-Level Laser Pumping System

For a laser medium at absolute zero, all the electrons of the atoms are at the ground state; however, for a laser medium at a finite temperature, some of the electrons are expected to jump to higher energy states. These atoms cannot be excited by the pumping energy which is equal to the difference between the energy levels  $E_4$  and  $E_0$ . The unused atoms result in absorption losses in the system, therefore reducing the output laser power. Then, it can be concluded that the cooler is the lasing medium, the better is the laser efficiency. Though absolute zero is unfeasible, considering the fact that increasing temperature has an adverse effect on the efficiency, some sort of temperature control is required. Electron transitions from  $E_3$  to  $E_2$  and from  $E_1$  to  $E_0$  generate phonon-dominated (radiationless) excess heat in the system which should be discharged out of the system.

### 1.3. Laser Crystal Material, Geometry and Pumping Structures in Solid-State Lasers

As the term “Solid-State” implies, solid lasing media are used in solid-state lasers. For the selection of a lasing medium for solid-state lasers, a host material is doped by rare earth ions. The most common host materials are crystals such as yttrium aluminum garnet (YAG), yttrium lithium fluoride (YLF), yttrium orthoaluminate (YALO), lutetium aluminum garnet (LuAG) [3]. The thermal and optical parameters of the crystal host have a direct impact on the design and operation of the laser system.

Theoretically, a laser can be produced from any laser crystal material and/or geometry for a high enough pumping power. However, only a few material hosts and ions with certain geometry lead to feasible systems. Rod, slab and disk geometries are the most commonly used laser crystal geometries. The selection of the laser crystal geometry is based on the cooling and pumping method of the laser crystal, and the optical requirements. When the infinite length laser slabs and rods are compared (neglecting the end effects), the slab geometry is found to be superior to the rod geometry in terms of the laser parameters such as, the thermally and stress induced birefringence, biaxial focusing and thermal stress fracture limit which is subjected to certain dimensional parameters given in (1.2) below [4]

$$\frac{(P_a/L)_{rod}}{(P_a/L)_{slab}} = \frac{2\pi}{3} \left( \frac{t}{w} \right) \quad (1.2)$$

where  $(P_a/L)$  is the absorbed power per unit length at the thermal stress fracture limit, and  $(w/t)$  is the aspect ratio of the laser crystal slab of width,  $w$ , and thickness,  $t$ . For a superior fracture limit relative to the rod, a slab must have an aspect ratio higher than  $3/(2\pi)$ .

Considering a finite length crystal with end-effects, it is also studied that for the slab laser geometry, the thermal focusing and depolarization effects throughout the crystal are significantly lower than those for the rod laser geometry [5].

The disk shaped laser crystals have significantly less thermal lensing, the lensing effect caused by inhomogeneous temperature distributions in the media, due to the reduction in the radial temperature gradients compared to rod lasers. This is achieved by cooling the disk laser crystal from one of the axial surfaces rather than the curved surface, which is the case with laser rod crystals. The cooling surface to volume ratio is very high in disk shaped crystals when compared with the other geometries. Only a weak lensing occurs due to two effects: the reduced bending of the disk caused by thermal expansion, and the pumped region diameter being smaller than the disk diameter [6]. The disk shaped laser crystal provides a higher efficiency, better output power and beam quality compared to the rod lasers with a similar pumping power [7].

The heat generated in the laser crystal is a fraction of the absorbed pumping energy in the medium. The heat generation in the laser crystal is due to quantum defect and additional loss mechanisms such as impurity absorption. The aim of the design is to increase the absorbed power in the optical path to improve the gain zone of the produced laser. This can be achieved by side pumping or by end pumping in axis with the generated laser beam [3]. Both side and end pumping methods have advantages over each other. The end pumping yields better beam quality and more laser power output than the side pumping for low power operations due to the good overlap between pumping and lasing volume [8]. On the other hand, focusing the pump beam to a small cross-section, in the end pumping, leads to high volumetric heat generations. This results in a high refractive index gradient due to the temperature gradients and high thermal stresses at increased pumping powers. These refractive index gradients cause thermal lensing, which has an adverse effect in the beam quality and divergence [9].

The laser crystal geometries and the pumping methods considered in the literature are illustrated in Figure 1.5.

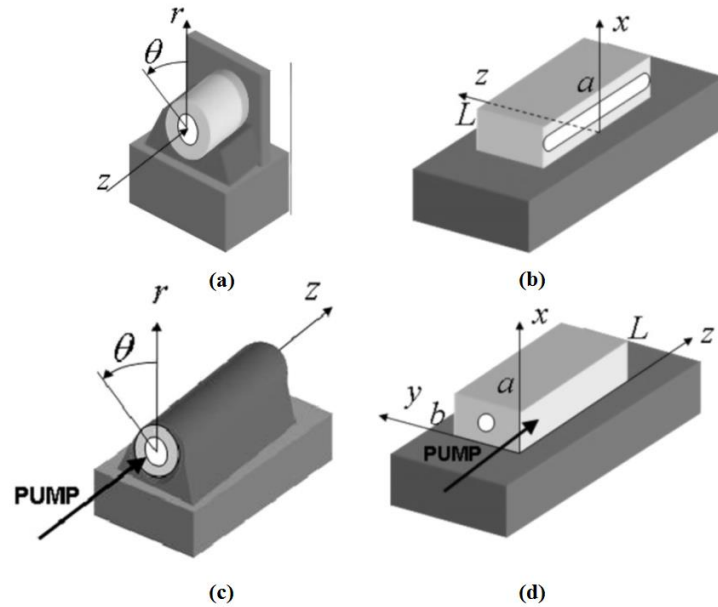


Figure 1.5 Laser System Representations: (a) End-Pumped Disk Laser (b) Side-Pumped Slab Laser (c) End-Pumped Rod Laser (d) End-Pumped Slab Laser.

#### 1.4. Thermal Effects in Solid-State Lasers

For the end-pumped solid-state lasers, thermal effects in the lasing medium are important factors for determining the limits of maximum achievable power. The pumping power is limited by the thermal fracture point of the lasing medium. Optical distortions caused by the thermal effects leads to losses in the output laser power and the beam quality. These thermal effects are widely studied in the literature and the studies on mitigation of thermal effects in solid-state lasers played an important role on the modern laser technology [10].

The main classifications of the thermal effects are: Thermal lensing [11], thermal fracture [8], thermally-induced stress birefringence and bifocusing [12-14]

The temperature of the crystal medium has a direct effect on the efficiency of the system, due to increasing absorption losses with increasing temperature of the laser crystal medium [15]. The temperature profile on the laser crystal medium yields other effects such as thermal lensing due to temperature dependent refractive index, thermal lensing due to the thermal expansion along the optical path in the laser crystal medium, thermal stresses in the laser crystal medium and stress related effects such as, stress induced birefringence. Birefringence is an optical property of non-isotropic transparent material whose refractive index is dependent on polarization and propagation direction of light. Inhomogeneous stress induces birefringence in an isotropic medium or alters the effect of existing birefringence in non-isotropic medium, which is called stress induced birefringence.

The refractive index of a crystal is a function of temperature. Therefore, a temperature gradient in a laser crystal medium generates a refractive index gradient. This gradient along the optical path causes a thermal lens effect as shown in Figure 1.6.

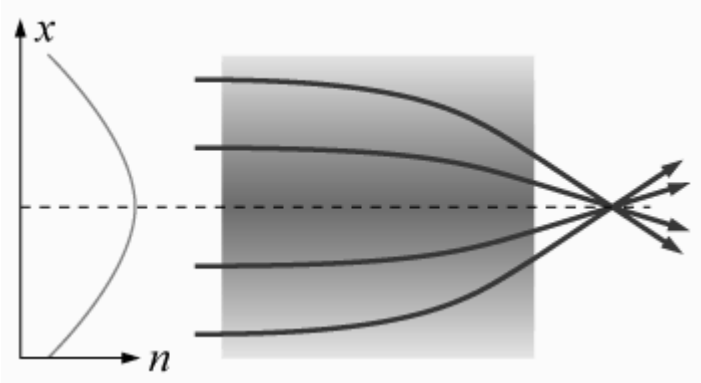


Figure 1.6 Lensing Effect effect in a Media with a Parabolic Variation of Refractive Index in the  $x$ -axis [16]

The other thermal lensing effect is due to the thermal expansion of the laser crystal medium. Thermal expansion causes the flat end-surfaces of the laser

crystal to assume a convex shape for the end-pumped configuration shown in Figure 1.7. Also the optical paths are inhomogeneously increased due to inhomogeneous thermal profiles. These effects are going to be extensively covered in the optical path difference (OPD) analysis section of this study.

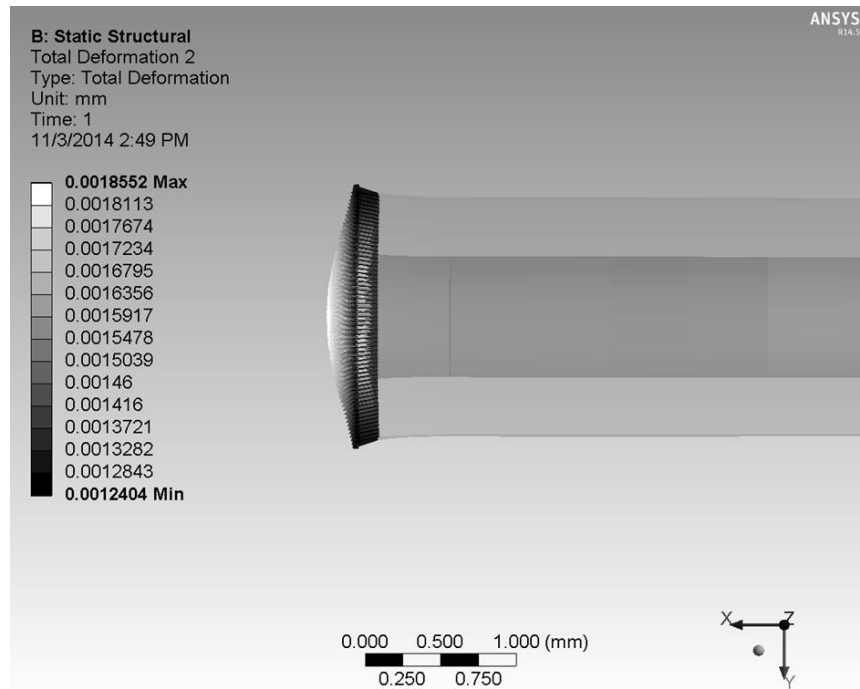


Figure 1.7 Deformation Occurring at the End-Surface of the End-Pumped Laser Crystal Slab

Temperature gradients in the laser crystal medium also lead to thermal stresses. As the aim of the laser cavity design is to increase the absorbed power in the optical path to improve the gain zone of the produced laser, the heat generation zone is always in close proximity of the optical path. The heat generated zone being in the laser crystal slab and the fact that the external surfaces are used to discharge heat, build a temperature gradient from the axis of the optical path to the external surfaces. The heat-generated zone of the crystal is bound to be warmer and to expand more than the zone closer to the external surfaces. Hence, there is in close proximity of the optical path, and tension in close proximity of

the external surfaces, since the external zone expands less than the inner zone of the laser crystal. The thermal stresses limit the maximum allowable pumping power due to the thermal fracture limit of the gain medium.

Considering the fact that the refractive index is also a function of stress [17], the thermal stresses have a direct effect on the thermal lensing of the laser crystal. The thermally induced stress birefringence and thermal aberrations are other thermal effects that need to be mitigated [10].

### **1.5.Literature Survey**

There have been various studies aiming to obtain temperature profiles in solid-state laser crystals for different crystal geometries, host materials and pumping configurations. Using the temperature distribution, thermal stress, thermal lens effect and thermally induced birefringence analyses can be conducted. Tilleman [3, 18] analytically obtained the steady-state temperature distribution and thermo-optical effects of end-pumped and side-pumped rod, slab and thin-disk laser crystals with Gaussian pumping profile. The thermal problem of the study involved an inverse linear temperature dependent thermal conductivity approximation and constant temperature boundary conditions. Other analytical steady-state thermal and thermo-optical solutions are presented for the double-end-pumping of the laser slab by diode pumping [19] or by multibar diode stack pumping [20]. The thermal and thermo-optical profiles of single end-pumped and side-pumped laser slabs and comparison of the theoretical results with the experimental ones are presented in the literature [21-26]. In the literature, both analytical and numerical thermal analyses for laser rods have been performed, extensively [27- 34].

Transient thermal and stress analyses on double-end-pumped laser crystal rods indicated that the maximum temperature, temperature gradient and thermal stresses occur at thermal equilibrium [35, 36]. It is for this reason that, the

steady-state approach can be validly used in thermal and thermo-optical analyses and design.

The symmetric double-end-pumping of a laser slab is reported to perform better than the single-end-pumping in terms of thermal and thermo-optical effects for the same amount of total pumping power [37]. There is effort in the literature to generate a more uniform illumination pump profile for fiber-optic-coupled [38] and for high-power diode lasers [39]. These beam shaping methods aim to generate a uniform pumping profile, consequently, a more uniform heat generation in the laser crystal rather than the highly non-uniform Gaussian distribution. Uniform heat distributions yield more parabolic temperature profiles and the thermal effects of these profiles are easier to compensate with standard optical components for the end-pumping configurations [31].

Studies also focus on the estimation of the thermal fracture limits of laser crystals [40] since thermally induced stresses not only affect the output power and the beam profile of the laser, but also cause fracture in the laser crystal medium when the ultimate strength of the crystal material is exceeded [8]. Uses of composite crystals with undoped host material brazed on pumping face have been shown to prevent thermal stress fracture [29, 41]. Also multiple resonator configurations are compared to find the improvements in preventing the thermal stress fracture and other thermal effects on slab laser systems [21, 41, 42].

The effect of the crystal geometry has also been investigated in the context of opto-thermal effects. It has been reported that higher aspect ratios of the crystal slabs reduce the thermal effects on the system due to larger cooling surfaces available on the slab [4, 5, 43, 44].

There are a few studies reported in the literature on Tm:YLF laser system, the selected gain material for the present study. Tm:YLF laser systems are used to pump Ho:YAG systems due to the fact that the Ho:YAG crystal does not have any absorption band that coincides with commercially available diodes [44]. Thulium has a broad and substantially strong absorption band at around 800 nm

making it ideal for diode pumping. Yttrium lithium fluoride (YLF) is a desired host for thulium when it is used as a pump source for 2100 nm Ho:YAG laser system because of the very good overlap of emission peaks with absorption band in Ho:YAG [44]. Thulium benefits from cross-relaxation which is an efficiency enhancing process that can lead to two ions in the upper laser level for one pump photon when pumped around 790 nm [45]. Tm:YLF lasers have been utilized as a pump for Ho:YAG laser both for end-pumping [44, 46], and for side pumping [47].

Since 1970's the development of efficient laser sources operating at around 2  $\mu\text{m}$  has been an active area of research because this wavelength region has many features that is attractive for laser sensing applications in high-energy-per-pulse mode, and medical applications [48]. The 2  $\mu\text{m}$  wavelength region corresponds to eye-safe region of the spectrum and atmospheric constituents such as,  $\text{CO}_2$  and water vapor have a matched absorption wavelength. Laser sources operating at around 2  $\mu\text{m}$  are used in lidar applications to measure atmospheric constituents, mid-infrared remote sensing applications, medical applications such as cutting tools for the tissue in surgical procedures and eye surgery [48].

YLF is an attractive host material due to the fact that it has a negative temperature coefficient of refractive index leading to a negative thermal lensing. When combined with the positive thermal lensing effect of thermal expansion, it decreases the overall thermal lensing effect[46]. Another advantage of the YLF crystal is the strong birefringence property that can be used to produce linearly polarized lasers with minimum depolarization loss [44]. The downside of the YLF is its low tensile strength and a stress-fracture limit of 40 MPa, about five times lower than that of YAG [40, 48]. Because of the low stress-fracture limit, average powers from single pass gains are limited [46]. It has been reported that for the end-pumping of Tm:YLF crystal rod with 790 nm diodes, thermally induced fracture occurs when the beam-waist pump intensities are around 5  $\text{kW}/\text{cm}^2$  [49].

## **1.6. Outline of the Thesis**

In this thesis, an active cooling system for a fiber-coupled-diode double end-pumped 1908 nm wavelength Tm:YLF laser system is designed. Conceptual designs are made for the crystal holding and the cooling geometries. The designs are compared in terms of the temperature profiles using analytical methods as well as finite element analyses. A prototype for the best performing conceptual design is assembled and experimental data regarding optical and thermo-optical properties of the product laser is obtained. The outline of the thesis in this respect is as follows.

In Chapter 2, the generated heat load in the Tm:YLF laser crystal slab due to optical pumping by a fiber-coupled laser diode is calculated for the laser cavity design. The pumping beam profile is studied to obtain the heat generation profile throughout the laser crystal. In addition, conceptual designs for the laser crystal holders for cooling the crystal are discussed.

An analytical thermal solution for the 4-face cooling case and a finite element model used in all cooling cases are presented in Chapter 3. OPD analysis details for all cooling cases considered are first presented. Then finite element solution of the 4-face cooling case is validated using the analytical thermal solution. The temperature distribution, thermal lens radii and thermally induced stress properties of all face cooling cases are compared.

In Chapter 4, the same crystal cooling cases are numerically investigated for the crystal and the crystal holder composite system and compared with the corresponding face cooling cases. The effects of the holder geometry, material and symmetry of the cooling are studied for the 4-side cooling case which yields the best thermal performance among the investigated cases.

Design considerations for the experimental setup, the experimental procedure, and the obtained data are presented in Chapter 5. Two experimental setups are investigated: one with thermo-electric cooling (TEC) and one with water cooling, for the 4-side contact case. Also for the TEC case, the effects of the symmetry in cooling are also investigated experimentally.

Finally, conclusions and closing remarks with suggestions for future work are presented in Chapter 6.

## CHAPTER 2

### SYSTEM CONFIGURATION AND HEAT LOAD CALCULATIONS

#### 2.1. Configuration of the Laser Resonator

The layout of the laser cavity is presented in Figure 2.1. Two identical commercial 793 nm continuous-wave (CW) diode modules with SMA fiber coupling manufactured by DILAS GmbH are used to excite a Tm:YLF laser crystal slab. The diode-coupled fiber laser output is focused on the lasing gain media by two focusing lenses. A highly reflective dichroic mirror is set at an angle of 45° to transmit the pump output beam of 793 nm wavelength into the laser cavity while reflecting back the 1908 nm laser beam to resonate between the output coupler and the reflector. The reflector on the right-hand side in Figure 2.1 of the Tm:YLF crystal is highly reflective (HR) at 1908 nm, and anti-reflective (AR) at 793 nm allowing the pump beam to pass through while fully reflecting the 1908 nm laser beam. The laser beam exits the cavity from the other output coupler which is partially reflective (PR) at 1908 nm. The cavity length is about 24 cm, but the position of the HR output coupler is adjustable.

Tm:YLF crystal slabs of dimensions 1.5×1.5×12 mm with different doping percentages are used in the experiments. However, the 4% thulium doped YLF crystal is the main selection and the focus of this study.

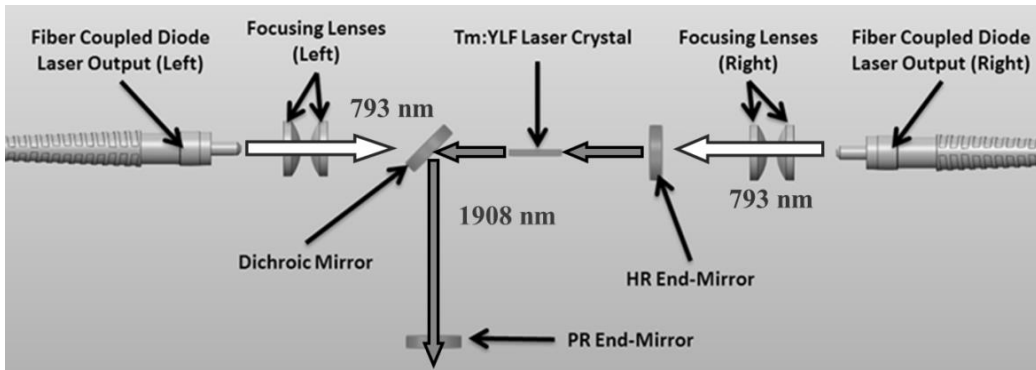


Figure 2.1 The Layout of Tm:YLF Laser System Cavity

The thermal analysis, simulations and experimentation in this study are based on this doping level. The two end-surfaces of the Tm:YLF crystal are polished while the four side surfaces are left ground to prevent parasitic lasing. The end surfaces are coated with anti-reflection for both pumping and laser wavelengths, since double end-pumping is used. The geometry of the Tm:YLF laser crystal is given in Figure 2.2. The Tm:YLF crystal holder and the cooling geometries with the crystal holder materials are going to be discussed in the following sections.

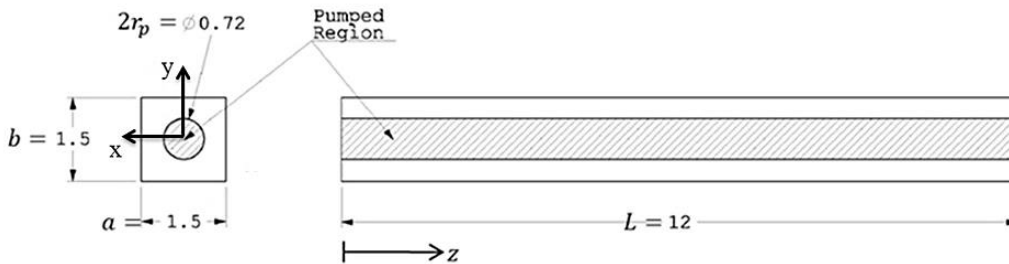


Figure 2.2 The Geometry of Tm:YLF Laser Crystal Slab and Pumped Region.

## **2.2. Calculation of Heat Generation in the Laser Slab**

The heat generation in the Tm:YLF laser crystal depends on numerous parameters. The first one is the incident pumping power. The greater it is, the greater the absorption in the lasing medium, resulting in a greater total heat load and laser power. The spot size of the pump beam also affects the volumetric heat generation since it is a measure of the incident pump flux. The wavelength of the pump laser is another factor due to both quantum efficiency and incident wavelength dependent absorption coefficient. The quantum efficiency is the fraction of the absorbed pump photons, contributing to the population of the upper laser [50]. The temperature of the laser crystal is also a factor in heat generation since it affects the overall efficiency of the system, which is one of the reasons why strict thermal management is required.

Thulium doping level of the YLF crystal and the pump profile are the other parameters influencing the heat generation in the lasing medium. The doping level affects the absorption through the path of pumping beam in the laser crystal medium. For the end pumping case, since the pump beam also propagates along the optical path, heat generation through the optical path changes with doping levels. If the lasing medium does not absorb all the incident pumping power, increasing the doping level can increase the total absorbed power, hence the efficiency. In the scope of this thesis, only 4% doped Tm:YLF crystals are studied.

By setting the maximum optical output of the two diode lasers to 30 W and using the experimental value of the absorbed pumping power fraction converted into heat as 0.34, the total heat load on the laser crystal has been calculated to be 20.1W assuming that all the incident pumping power is absorbed by the laser crystal. The 30 W diode pumping power has been selected as the maximum due to the damage thresholds of the optics. Also, selecting the total heat load as 20.1 W was a conservative approach since for the real operations a laser output power

of 17 W can be obtained by lower optical pumping powers. The pump optical power as a function of the current supply data is given in Appendix A.

In this study, the heat load term is used for the total excess heat generation occurring in the laser slab and has a unit of W. On the other hand, the heat generation profile is used for the profile of the volumetric heat generation in  $x$ ,  $y$ , and  $z$  coordinates with a unit of  $\text{W}/\text{mm}^3$ . The heat generation profile of a single end-pumped laser slab through the  $z$ -axis proposed by Tilleman [18] has been modified for symmetric double-end-pumping with identical pump beams as

$$Q(x, y, z) = \frac{\eta P_{abs}}{\pi r_p^2} \cdot \frac{\alpha_\lambda [\exp(-\alpha_\lambda z) + \exp(-\alpha_\lambda (L-z))]}{1 - \exp(-\alpha_\lambda L)} f_0(x, y), \quad (2.1)$$

where  $P_{abs}$ ,  $\eta$ ,  $r_p$  and  $L$  are the pumping power absorbed in the laser medium, the fraction of the absorbed power converted into heat, the radius of the optical pump beam in the laser medium, and the effective length of the laser medium respectively.  $f_0$  is the spatial distribution function of the absorbed power and is dependent on the laser medium geometry and the beam profile of the optical pump inside the crystal.

The heat generation profile along the fast-axis ( $z$ -axis in Figure 2.2) of the crystal for 20.1 W total heat generation calculated using equation 2.1 is given in Figure 2.3.

Comparing the heat generation profiles caused by a single end-pumping and by a symmetric double end-pumping, a more homogenous profile has been obtained in the case of symmetric double-end-pumping. Since the double end-pump profile is symmetric, the total absorbed power due to a single diode pump is half of the total absorbed power. When only one diode pump is utilized (rather than two symmetric ones) in order to achieve the same total absorbed pump power, the maximum heat generation through the fast-axis increases significantly, increasing also the temperature gradient. The pump profile and its incident illumination on the crystal are also very important in heat generation.

The pumping illumination profiles directly affect the heat generation profiles in the  $x$ - $y$  plane which is the cross-section plane perpendicular to the laser beam and the pumping beam propagation.

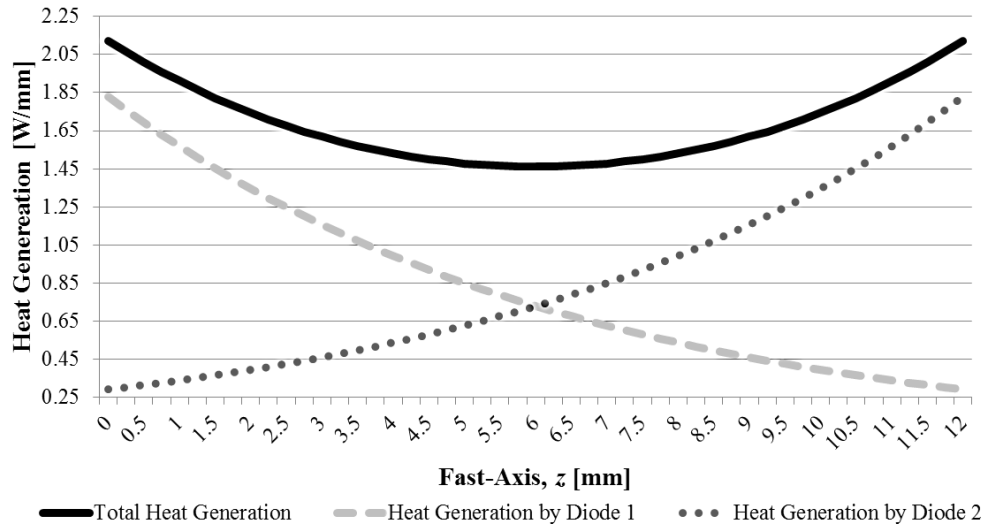


Figure 2.3 The Heat Generation Through Fast-Axis of the 4% Tm:YLF Laser Slab with Double End-Pumping.

A ray tracing analysis has been conducted using the commercial simulation software ZEMAX to determine the incident illumination on the crystal. It is aimed to focus the fiber output at a distance of 4 mm from both crystal end-surfaces. The results of the ZEMAX analysis for the pump illumination on the laser crystal are given in Figure 2.4 to Figure 2.7. It can be observed that the diameter of the pump illumination varies along the fast-axis of the crystal. The illumination data is plotted for 1 mm  $\times$  1 mm detector centered in the optical path. The plots of incoherent irradiance along the  $x$ -axis are given in Appendix B. When these plots and the figures are investigated, it may be observed that the radius of the pumping beam was about 0.3 mm and even though the uniformity of the profile changes, the radius of the pumping beam does not vary significantly. For the present study, a cylinder with constant diameter 720  $\mu$ m

and length of 12 mm has been considered for the pumped volume in the laser crystal slab.

Considering the ZEMAX analysis provided in Figure 2.4 to Figure 2.7, it can be said that the pump profile is neither Gaussian as in the case of direct diode pumping nor a total top-hat profile. It can be concluded that the profile is in between Gaussian and top-hat but is close to top-hat. Hence, the uniform heat generation assumption in the cross-section perpendicular to the fast-axis ( $xy$ -plane) has been validated.

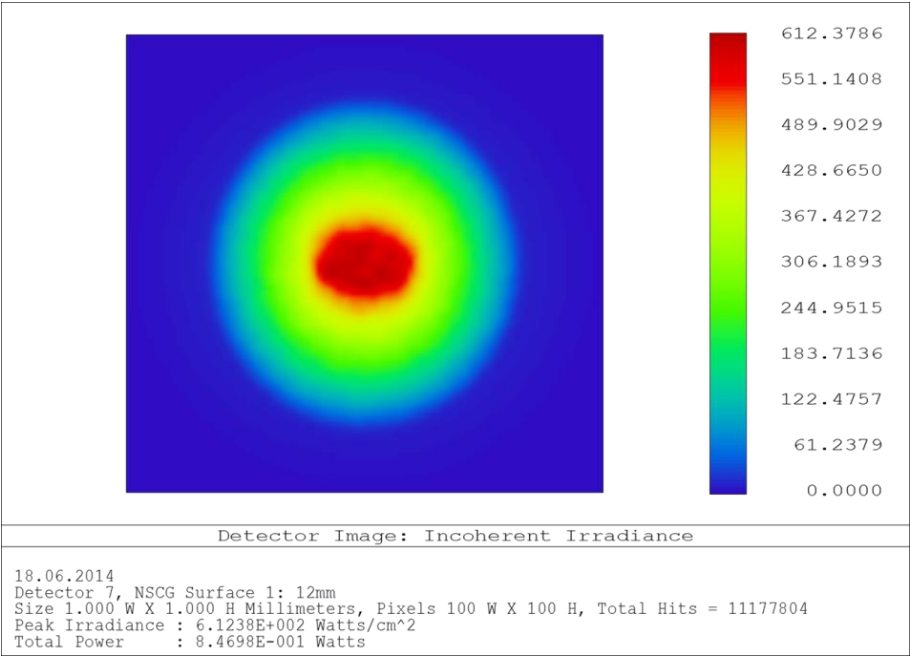


Figure 2.4 The Pump Illumination Profile on the Laser Crystal at the End Surfaces  $z = 0$  and 12 mm

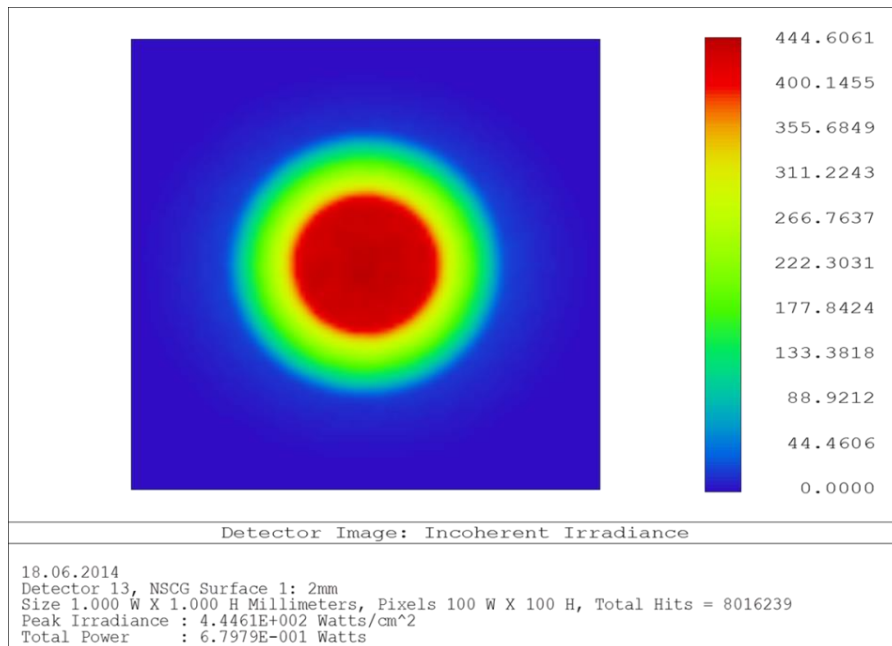


Figure 2.5 The Pump Illumination Profile on the Laser Crystal Slab at  $z = 2$  mm and 10 mm

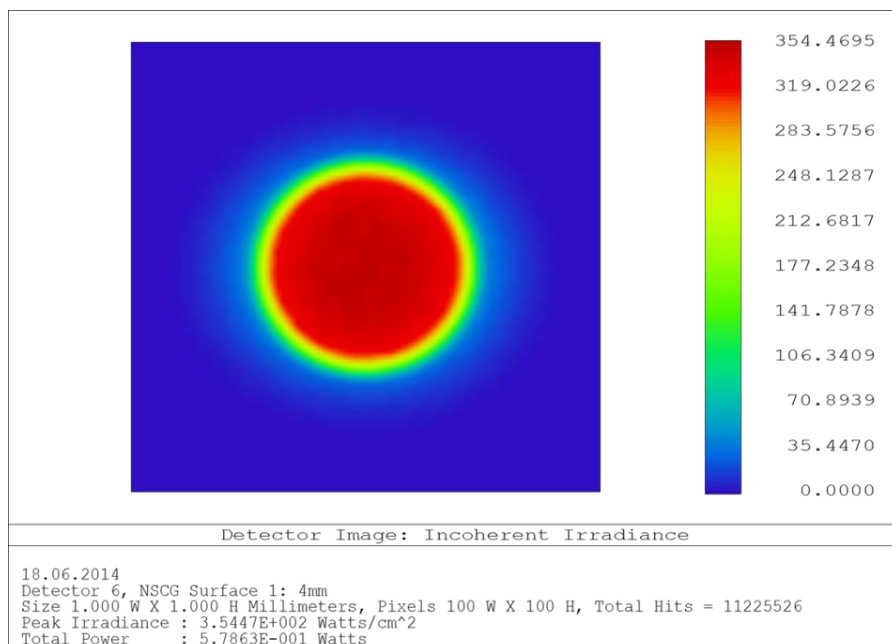


Figure 2.6 The Pump Illumination Profile on the Laser Crystal Slab at  $z = 4$  mm and 8 mm

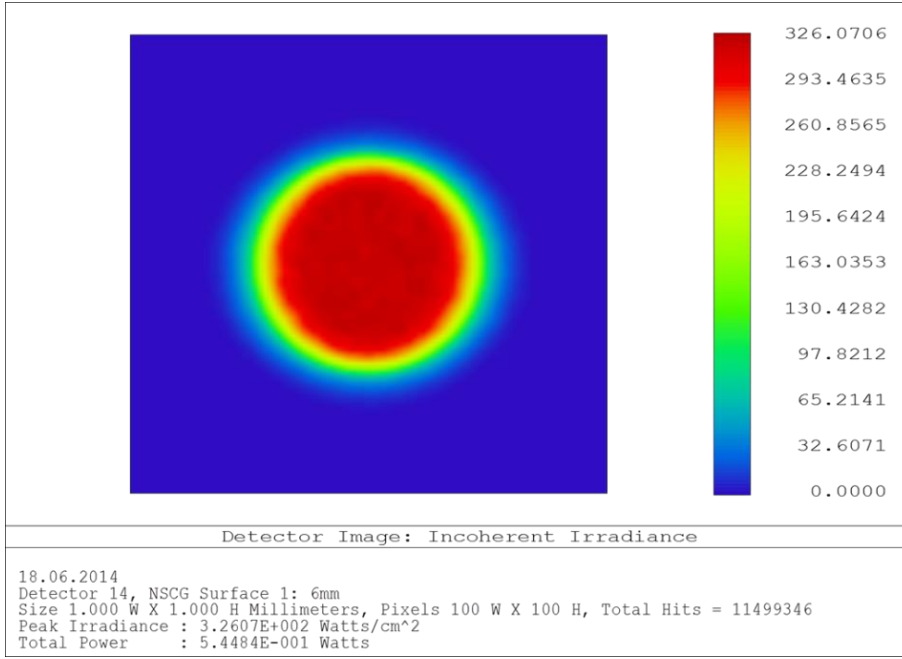


Figure 2.7 The Pump Illumination Profile on the Laser Crystal Slab at the Middle Surface,  $z = 6$  mm

The spatial distribution functions to be substituted into equation 2.1 for Gaussian and top-hat (uniform) heat generation profiles are given in equations 2.2 and 2.3.

$$f_{0_{Gaussian}}(x, y) = \begin{cases} \exp\left\{-2\left[\left(\frac{x}{r_p}\right)^2 + \left(\frac{y}{r_p}\right)^2\right]\right\} \cdot \left\{\sqrt{\frac{\pi}{2}} \operatorname{erf}(\sqrt{2})r_p\right\}^{-1} & ; \sqrt{x^2 + y^2} \leq r_p \\ 0 & ; \sqrt{x^2 + y^2} > r_p \end{cases} \quad (2.2)$$

$$f_{0_{Top-Hat}}(x, y) = \begin{cases} 1 & ; \sqrt{x^2 + y^2} \leq r_p \\ 0 & ; \sqrt{x^2 + y^2} > r_p \end{cases} \quad (2.3)$$

### **2.3. Conceptual Design of Laser Crystal Slab Holders**

The laser crystal holders should be designed according to the selected cooling method. In this study, conceptual laser crystal holders have been considered and debated for a symmetric end-pumped laser crystal slab. For the necessity of active cooling on efficient operation thermoelectric cooling (TEC) and liquid cooling have been investigated.

Liquid cooling is frequently used for laser crystal rod cooling due to the ease of construction compared to other alternatives. The sealing of the cooling liquid from the laser cavity becomes effective with the usage of o-rings. An example liquid cooling application may be given as the cooling of flash-lamp-pumped Neodymium (Nd):YAG rods. Both the flash and Nd:YAG rods are sealed in the pumping cavity with cooling liquids and the usage of o-rings at their contact.

For the end-pumped slab laser crystals, different alternatives of direct liquid cooling have been introduced in the literature [51]. One is immersing the laser crystal into the cooling liquid. The absorption coefficient of the cooling liquid for the pump and the laser wavelength, and the flow parameters play important roles in this cooling method. The vorticity of the flow, bubble generation throughout the flow and other effects that cause non-homogeneity of the refractive index along the optical path can affect the laser parameters.

Another direct liquid cooling method for end-pumped slabs is to seal the cavity from the cooling fluid. Since the cross-section is rectangular, standard o-rings as used in laser rod sealing cannot be applied. Liquid o-rings can be used to overcome this problem efficiently but the outgassing properties of these liquid o-rings pose a danger to the long-lasting operation of a completely sealed laser device. Some different cooling configurations are given in Figure 2.8. Direct contact crystal cooling is presented in Figure 2.8(a), and the immersion of laser crystal into the cooling liquid without applying direct sealing on the pumped surface crystal is shown in Figure 2.8(b). The laser crystal is fully immersed in the cooling liquid and the pumped end-surface is also cooled. Figure 2.8(c)

indicates a liquid cooling method where the pumped end-surface is cooled by a sapphire plate, and Figure 2.8(d) is again for liquid cooling where the undoped crystal host material is brazed to the pumped end-surface to relieve the thermal load.

Rather than direct liquid cooling, indirect liquid cooling (not cooling the crystal directly but by cooling the mechanics that hold the crystal) can prove to be less problematic. It can be achieved by immersing a part of the holder into cooling liquid flow or by using the cooling channels that are embedded in the holder. For the indirect case, it is easier and more effective to seal the cavity from the cooling liquid since the sealing is to be designed between two mechanical parts, not between a precise optical and a mechanical part. In addition, the sealing geometry is not limited by the laser slab. As mentioned in the Introduction chapter of this study, indirect cooling is the most common commercial application.

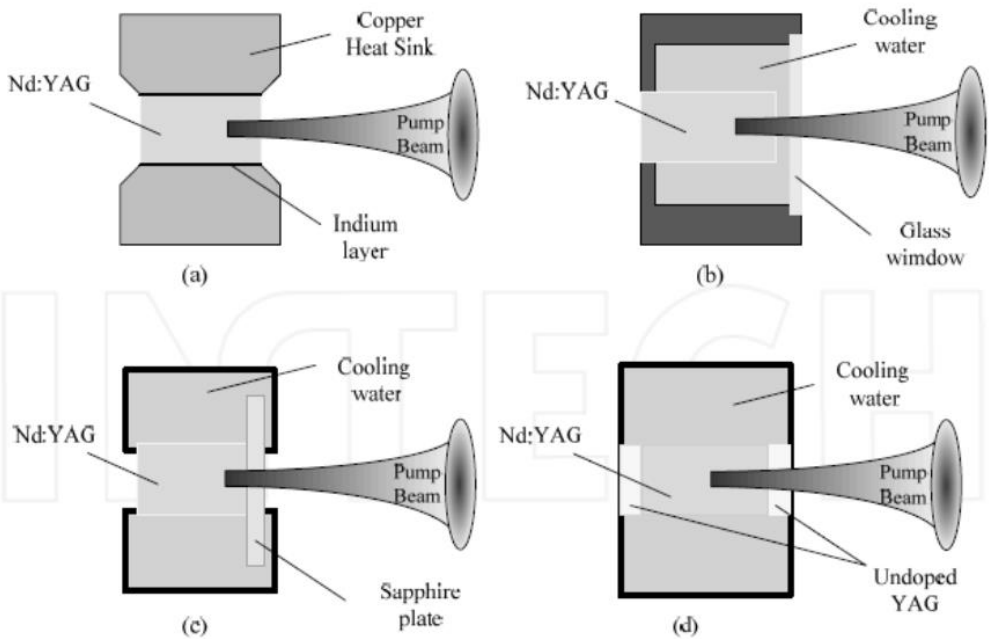


Figure 2.8 Different Cooling Configurations in End-Pumped System of Nd:YAG

[51]

For an active cooling requirement, which is the case for the Tm:YLF application, a refrigeration cycle is required for the liquid cooling. The general practice for laboratory setups is to use a chiller unit for this purpose. On the other hand, for a field application device, a compact refrigeration system is required for liquid cooling.

The need for a relatively bulky refrigeration unit can be averted by using thermoelectric coolers (TEC). They provide very good temperature accuracy and are compact in design when compared to refrigeration units [52]. Also a single component can achieve the same cycle of a refrigeration unit and since there is no cooling liquid, there is no need for sealing either. It can directly be mounted on the crystal holder.

When cooling applications are taken into account, the other issue to consider is the available geometry of the laser slab. The four side-surfaces are available for heat discharge. Generally high aspect ratio laser slabs are used to increase the heat transfer area [4, 5, 43]. For our case a unity aspect ratio slab is used. Conceptual design alternatives for the holders are given in Figure 2.9.

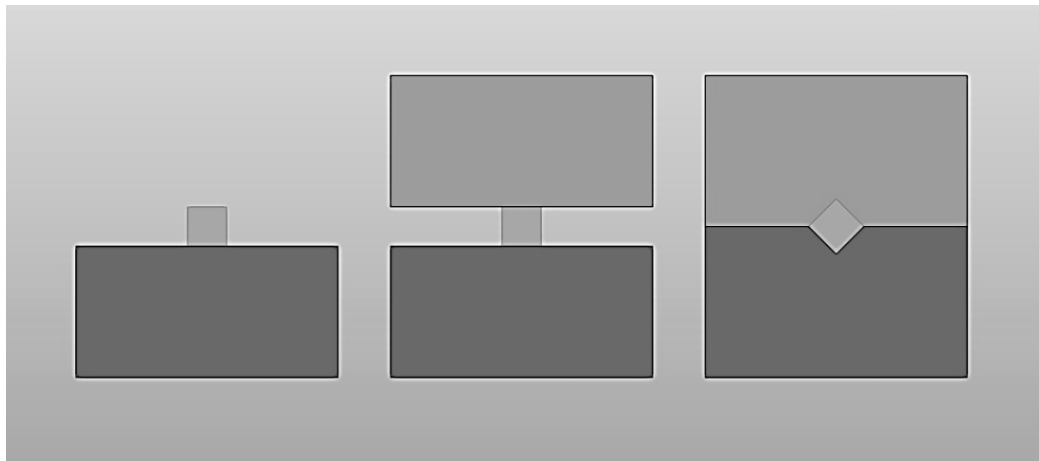


Figure 2.9 The Conceptual Holders for the Laser Slab Side-Contact Cooling

The four heat transfer surfaces of the crystal can be used as shown in Figure 2.9. The first one is the case when only one of the surfaces is used to cool the crystal. This is the most primitive case since the construction is simple but three of the four side-surfaces cannot be used to discharge heat. The second case is the most common application, using two parallel surfaces to cool the crystal. It doubles the heat transfer area while still retaining the construction simplicity. Basically, the crystal is sandwiched between two flat crystal holders. For this case, the selected slab is designed to have larger heat transfer surfaces compared to the ones that are not used for heat transfer. This significantly increases the heat transfer area, however, due to the low thermal conductivity and the temperature gradients that occur in the crystal, this design can yield adverse thermal effects if the aspect ratio is not optimized. The last option is to use all four side-surfaces for the heat transfer. This case provides the maximum heat transfer area from the laser crystal. However, the construction geometry is not as simple as the previous ones.

The conceptual designs are to be judged mainly according to their predicted thermal performance. The thermal performance, the major concern, is followed by the machinability of the holders, the precision of the system, the ease of assembly of the system and the cost.

A thermal interface material (TIM) is used for the contact surfaces to improve the heat transfer and it turns out that the usage of TIMs is crucial for the thermal performance. The TIMs can be mounted between the laser crystal and the holder and the required pressure on TIMs can be applied in the assembly process.

Considering these parameters, four holder design alternatives are introduced for 4-side cooling of the crystal. The first 4-side contact holder design has two different holders. The main holder is L-shaped and it gives the assembly the accuracy of the laser crystal as shown in Figure 2.10(a). It contacts two adjacent side-surfaces. The thermal contacts for the remaining surfaces are achieved with the block holder on the top left corner. The pressure on the TIMs is adjusted by

mounting the block holder on the L-shaped holder in both horizontal and vertical directions. The downside of this design is the difficulty in adjusting the pressure distribution on the TIMs and the fact that one of the cooling surfaces is shared by two holders which can lead to assembly difficulties.

The second conceptual design shown in Figure 2.10(b) is similar to the first one. The mounting difficulties due to unequal pressure distribution on TIMs cannot be eliminated completely by using two identical holders, but the problem of the second cooling surface can be overcome since the cooling surfaces are not shared with the two holders.

The third conceptual design in Figure 2.10(c) uses three different holders. The L-shaped holder is used for the accurate positioning of the crystal slab and the other two holders are used to adjust the pressure on the TIMs. However, the assembly is relatively complex.

The last design for 4-side cooling consists of two identical holders as given in Figure 2.10(d). The design is just like the second design alternative, but the holders have V-shaped grooves for the crystal mounting. The crystal is mounted on those V-shaped grooves with a foil used as a TIM wrapped around it. The pressure is adjusted by the assembly bolts. The pressure distribution of the TIM is better than that of the second case and the assembly does not require bolts in both horizontal and vertical directions to adjust the pressure on the TIM on the horizontal and vertical surfaces separately. The only downside is that the laser crystal slab is required to be tilted by 45°.

The first three conceptual designs are relatively easier to machine and cost-friendly but the last one is more suitable since it has less mechanical contact between the holders and is easier to assemble. Less mechanical contact yields less contact resistance which may cause inhomogeneous temperature profiles. It should be noted that for the last conceptual design shown in Figure 2.10(d), the mechanical contact zone is in symmetry line for 2-surface cooling method.

Hence, there expected to be no heat transfer through that mechanical contact zone bypassing the effect of contact resistance between holders.



Figure 2.10 The Conceptual Holders for the Laser Slab with 4-Side-Contact Cooling

## CHAPTER 3

### VALIDATION OF THE FINITE ELEMENT MODEL AND THE THERMAL SIMULATIONS OF THE LASER CRYSTAL SLAB

In this chapter, the analytical thermal solution of an end-pumped laser slab system was used to validate the finite element model that is used in the present study.. An analytical model has been selected from the literature that involves the thermal conductivity of the slab as an inverse linear function of temperature and four Dirichlet type boundary conditions are applied on the four side-surfaces of the slab. The pumping profile is assumed to be Gaussian and it is continuous throughout the problem domain. The validated finite element model involves constant thermal conductivity and discretized heat generation zones.

The reason for using a finite element model for the present analyses is that the analytical models presented in the literature are for specific laser properties that are similar to the case in this study, but are not fully covering all the aspects of the system, such as symmetric double-end pumping. Also, analytical models are presented for Gaussian heat generation profiles, since it yields a continuous heat generation profile in the domain of the problem. In this study, uniform heat generation profile, which yields a discontinuous heat generation profile in the problem domain causing a very complex thermal problem, is also investigated. Hence, finite element solutions are preferred to handle both Gaussian and uniform heat generation profiles. In Chapter 4, a composite system with both laser crystal and the laser crystal holder are investigated by FEM, since analytical simulations for these systems are extremely hard and require simplifications.

In Section 2.1 the pump profile of the present system was stated to be between Gaussian and top-hat (uniform), being closer to the top-hat profile. Gaussian heat generation profile has been selected for the analytical solution, since it is easier to solve than discontinuous uniform heat generation profile, and there are numerous studies employing the analytical thermal model for laser crystals with Gaussian pumping profile [3, 18]. The other reason for the selection of the Gaussian profile was that it is a more complex heat generation case than that of uniform heat generation and the discretization plays a more significant role.

### 3.1. Analytical Thermal Model to Validate the Finite Element Model

The temperature distribution of the end-pumped laser crystal by a Gaussian pumping profile proposed by Tilleman [18] and its derivation is going to be studied in this chapter. The proposed analytical solution is for a single end-pumped laser slab, but can also be applied to a symmetric double-end-pumped laser slab by using superposition. The solution is valid for less than 5% lasant doping levels and the linear approximation for the thermal conductivity is valid for the temperature range of 77-770 K for laser crystal materials [3]. The thermal conductivity may be expressed using an inverse linear approximation as

$$k(T) = k_0 \frac{T_0}{T} \quad (3.1)$$

where  $k_0$  is the thermal conductivity coefficient at the temperature  $T_0$ .

The governing equation is the steady-state heat equation for Cartesian coordinates in the form

$$\nabla_{x,y,z} \cdot k(\nabla_{x,y,z} T) + Q(x, y, z) = 0. \quad (3.2)$$

Substitution of the expression for  $k$  in (3.1) into the heat equation (3.2) yields

$$\nabla_{x,y,z} \cdot k_0 \frac{T_0}{T} (\nabla_{x,y,z} T) + Q(x, y, z) = 0. \quad (3.3)$$

As it can be seen from (3.3) the heat equation becomes non-linear. The linearization of the (3.3) can be achieved by applying Kirchoff's transformation and introducing a new temperature variable  $\theta$  as

$$\theta(x, y, z) = \ln \frac{T(x, y, z)}{T_0}. \quad (3.4)$$

Kirchoff's transformation of (3.3) can be rewritten as

$$k_0 T_0 \nabla_{x,y,z} \cdot \frac{1}{T} (\nabla_{x,y,z} T) + Q(x, y, z) = k_0 T_0 \nabla_{x,y,z}^2 \ln \frac{T}{T_0} + Q(x, y, z). \quad (3.5)$$

Variable transformation and rearranging of (3.5) yields

$$K \nabla_{x,y,z}^2 \theta(x, y, z) + Q(x, y, z) = 0 \quad (3.6)$$

where  $K = k_0 T_0$  is a constant. It should be noted that (3.6) is similar to (3.2) for a temperature independent thermal conductivity.

The heat load in the laser medium for an optically pumped laser is generated by a fraction of the absorbed optical pump radiation. With luminescence and vibronic relaxation effects, the pumping power which is not converted to laser output generates the heat load [3]. The heat load for this problem can be expressed as [18]:

$$Q(x, y, z) = \frac{\eta P_{abs}}{\pi r_p^2 L_{eff}} f_0(x, y, z) \quad (3.7)$$

where  $P_{abs}$ ,  $\eta$ ,  $r_p$ ,  $L_{eff}$  are the pumping power absorbed in the laser medium, the fraction of the absorbed power not converted into laser (quantum yield), the radius of the optical pump beam in the laser medium, and the effective length of the laser medium, respectively.

$f_0$  is the spatial distribution function of the absorbed power which is dependent on the laser medium geometry and the beam profile of the optical pump inside the crystal. Also, some symmetry considerations may alter the geometry of the

problem. Hence, the spatial distribution function is to be considered after determining the boundary conditions.

The cooling geometry selection and the laser medium geometry define the boundary conditions of the problem. Previously the governing definition of the problem has been defined. For the slab geometry, six surface boundary conditions shall be designated for the 3D solution of the temperature profile.

As previously mentioned, this analytical solution is for 4-sided cooling of the laser crystal. Therefore all four side surfaces has Dirichlet type boundary conditions as

$$T(0, y, z) = T(a, y, z) = T(x, 0, z) = T(x, b, z) = T_w. \quad (3.8)$$

The converted boundary conditions in terms of the  $\theta$  variable may be expressed as

$$\theta(0, y, z) = \theta(a, y, z) = \theta(x, 0, z) = \theta(x, b, z) = \theta_w \quad (3.9)$$

The other two end-surfaces of the crystal are to be held either exposed to vacuum or idle gas. These two end-surfaces can be assumed to be isolated since the heat transfer is negligible compared to the heat transfer rate from the side-surfaces. The Neumann type boundary conditions are

$$\left. \frac{\partial T(x, y, z)}{\partial z} \right|_{z=0} = \left. \frac{\partial T(x, y, z)}{\partial z} \right|_{z=L} = 0, \quad (3.10)$$

and the converted boundary conditions in terms of the  $\theta$  variable are

$$\left. \frac{\partial \theta(x, y, z)}{\partial z} \right|_{z=0} = \left. \frac{\partial \theta(x, y, z)}{\partial z} \right|_{z=L} = 0. \quad (3.11)$$

For end-pumping, the maximum power absorption therefore the maximum heat generation occurs at the end-surface facet. Due to the intense heat generation at the facet and the end-surface being exposed to vacuum or idle gas, the heat transfer from the end-surface is nearly zero. For these reasons, Tilleman [18]

suggests brazing of undoped caps to the facet of the slab crystal to relieve the end-surfaces from the excess heat load since the pump beam passes these caps unabsorbed, therefore generating no heat and the heat conducted through these caps to the surfaces reduces the maximum temperature. The heat load formulations are given considering the undoped cap for the case of Tilleman's study, which is not used in the present study; therefore the heat load is modified as:

$$Q(x, y, z) = \frac{\eta P_{abs}}{\pi r_p^2} \cdot \frac{\alpha_\lambda \exp(-\alpha_\lambda z)}{1 - \exp(-\alpha_\lambda L)} f_0(x, y) \quad (3.12)$$

where  $\alpha_\lambda$  is the absorption coefficient, and the spatial distribution  $f_0$  for single end-pumping of a slab laser crystal with Gaussian profile considering the whole geometry is given by:

$$f_0(x, y) = \exp \left\{ -2 \left[ \left( \frac{x-a/2}{r_p} \right)^2 + \left( \frac{y-b/2}{r_p} \right)^2 \right] \right\} \quad (3.13)$$

It should be noted that both (3.12) and (3.13) of this analytical solution differ from (2.1) and (2.2), which simulate the uniform heat generation profile of the real case.

At this point, before the solution one may simplify the problem using symmetry considerations in  $x$  and  $y$  coordinates. Rather than using the domain  $x: 0 \rightarrow a$  and  $y: 0 \rightarrow b$ , the domain  $x: 0 \rightarrow a/2$  and  $y: 0 \rightarrow b/2$  can be used. Both full and quarter domains are shown in Figure 3.1.

For the quarter domain shown in Figure 3.1(b), the boundary conditions are altered and the spatial distribution function  $f_0$  is slightly modified. There are two Dirichlet type boundary conditions and four Neumann type boundary conditions as

$$\frac{\partial \theta(x', y', z)}{\partial z} \Big|_{z=0} = \frac{\partial \theta(x', y', z)}{\partial z} \Big|_{z=L} = \frac{\partial \theta(x', y', z)}{\partial x'} \Big|_{x'=0} = \frac{\partial \theta(x', y', z)}{\partial y'} \Big|_{y'=0} = 0$$

and

$$\theta(x', b/2, z) = \theta(a/2, y', z) = \theta_w \quad (3.14)$$

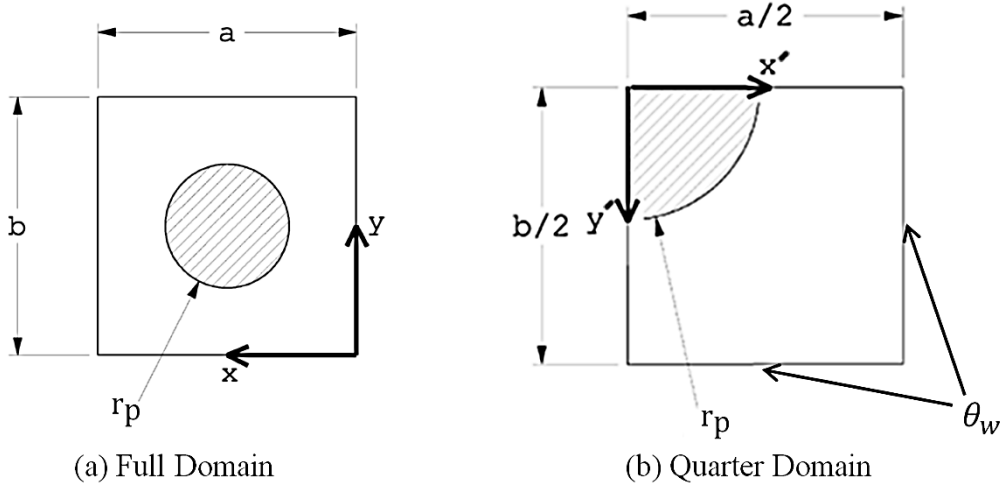


Figure 3.1 The Illustration of the Analytical Solution Domain for the (a) Full domain and (b) Quarter Domain.

To adapt the heat load considering the symmetry, the function  $f_0$  is modified as

$$f_0(x, y) = \exp \left\{ -2 \left[ \left( \frac{x}{r_p} \right)^2 + \left( \frac{y}{r_p} \right)^2 \right] \right\} \quad (3.15)$$

By solving the homogeneous equation (3.6) or the Laplace equation and satisfying the boundary conditions, Green's function can be constructed. For the defined problem, Green's function may be constructed as

$$G(\xi, \eta, \zeta, x, y, z) = \frac{1}{ab} \sum_{n=0}^{\infty} \sum_{m=0}^{\infty} \frac{\cos(p_n x) \cos(p_n \xi) \cos(q_m y) \cos(q_m \eta)}{\beta_{nm} \cosh(\beta_{nm} L)} H_{nm}(z, \zeta) \quad (3.16)$$

where  $\xi, \eta, \zeta$  are Green's function variables and the function  $H_{nm}(z, \zeta)$  is defined as

$$H_{nm}(z, \zeta) = \begin{cases} \cosh(\beta_{nm}\zeta) \cosh[\beta_{nm}(L - z)]; & L \geq z \geq \zeta \geq 0 \\ \cosh(\beta_{nm}z) \cosh[\beta_{nm}(L - \zeta)]; & L \geq \zeta \geq z \geq 0 \end{cases} \quad (3.17)$$

with

$$p_n = \left(n + \frac{1}{2}\right) \frac{\pi}{a}; \quad q_m = \left(m + \frac{1}{2}\right) \frac{\pi}{b}; \quad \beta_{nm} = \sqrt{p_n^2 + q_m^2} \quad (3.18)$$

The formal solution of the equation set of (3.6) and (3.14) is

$$\theta(x, y, z) = \theta_w + \int_0^a \int_0^b \int_0^L Q(\xi, \eta, \zeta) G(\xi, \eta, \zeta, x, y, z) d\xi d\eta d\zeta \quad (3.19)$$

Substituting (3.16) and (3.12) into (3.19) and carrying out the integrations, the solution is obtained as

$$\begin{aligned} & \theta(x, y, z) \\ &= \theta_w + \frac{1}{4} \frac{\eta P_{abs} \alpha^2}{abK[1 - \exp(-\alpha z)]} \sum_{n=0}^{\infty} \sum_{m=0}^{\infty} F_n(p_n, a) F_m(q_m, b) \frac{\cos(p_n x) \cos(q_m y)}{\beta_{nm} \cosh(\beta_{nm} L)} \\ & \cdot \frac{1}{\alpha^2 - \beta_{nm}^2} \left[ \cosh\{\beta_{nm}(L - z)\} - e^{-\alpha L} \cosh(\beta_{nm} z) - \frac{\beta_{nm}}{\alpha} e^{-\alpha z} \sinh(\beta_{nm} L) \right] \end{aligned} \quad (3.20)$$

where

$$F_n(p_n, a) = \exp\left[-\frac{(p_n r_p)^2}{8}\right] \left\{ \begin{aligned} & \operatorname{erf}\left(\frac{a}{\sqrt{2} r_p}\right) + \frac{2\sqrt{2} a}{\pi r_p} e^{-\left(\frac{a}{2r_p}\right)^2} \\ & \times \sum_{k=0}^{\infty} \frac{e^{-\frac{k^2}{4}}}{k^2 + 2\left(\frac{a}{r_p}\right)^2} \left[ 1 - \cos(p_n a) \cosh\left(\frac{k p_n r_p}{2\sqrt{2}}\right) \right] \end{aligned} \right\} \quad (3.21)$$

The analytical solution for the problem with single end-pumping is given in (3.20) where the coefficients  $p_n$ ,  $q_m$  and  $\beta_{nm}$  are expressed by (3.18).

The heat load for the symmetric end-pumping case can be obtained by superposition using (3.12) as

$$Q(x, y, z) = Q_1(x, y, z) + Q_2(x, y, z) = \frac{\eta P_{abs}}{\pi r_p^2} \cdot \frac{\alpha(\lambda) \{ \exp(-\alpha(\lambda) z) + \exp(-\alpha(\lambda) (L-z)) \}}{1 - \exp(-\alpha(\lambda) L)} f_0(x, y) \quad (3.22)$$

Since temperature differences are considered,  $\theta(x, y, z) - \theta_w$  has been calculated. The MATLAB code to execute the analytical solution is given in Appendix C, and the results are presented in Section 3.4.

### 3.2. ANSYS Workbench Finite Element Model of Laser Crystal Slab

A finite element model of the same thermal problem described in the Section 2.1 is created using ANSYS R14.5 Workbench Software Steady-State Thermal Module.

For the Gaussian heat generation profile, the same profile as in the analytical solution, the heat generation is discretized. The reason for discretization is that ANSYS Workbench v14 Steady-State Thermal Module does not compute internal heat generation as a function of coordinates, but only computes it as a function of time. In the fast-axis direction (z-axis), the heat generation zone is divided into twenty four equal elements each having a thickness of 0.5 mm. There is a perfect match between the continuous and the discretized heat generations through the fast-axis as given in Figure 3.2. The twenty four element discretization in z-axis is illustrated in Figure 3.3 where the discretization elements are shown from z1 to z24 where z1 is the element between  $z = 0$  and  $z = 0.5$  mm, z2 is the element between  $z = 0.5$  mm and  $z = 1.0$  mm, etc.

Since the heat generation is Gaussian, the elements are also discretized in the  $xy$ -plane. Four elements are used as cylinders and hollow cylinders with diameters of 0.72 mm, 0.48 mm, 0.24 mm and 0.12 mm. A total of ninety six heat generation elements are constructed.

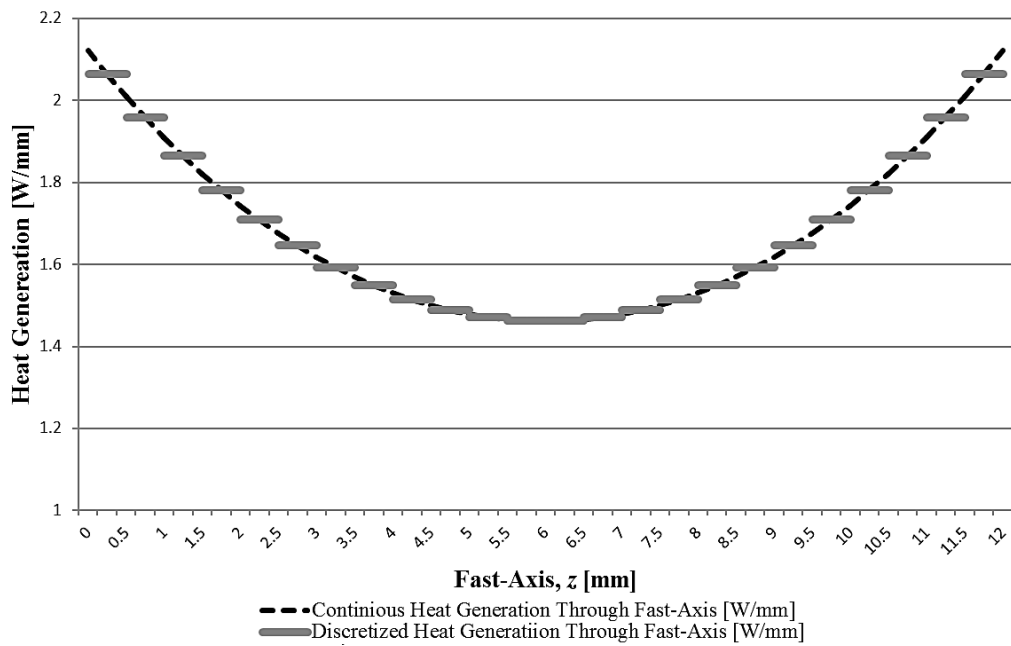


Figure 3.2 Continuous and Discretized Heat Generation Through Fast-Axis ( $Z$ -Axis)

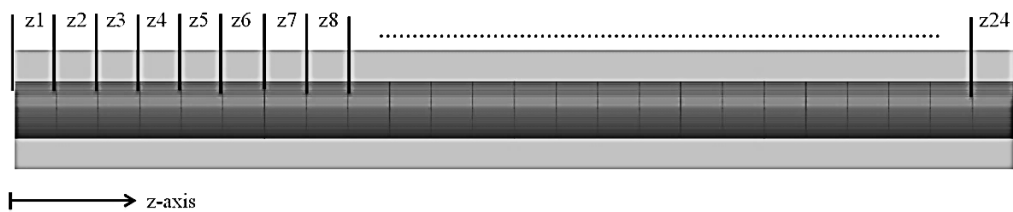


Figure 3.3 Discretized Elements in  $z$ -Direction.

The discretization elements in  $xy$ -plane and the radially outward axis “ $r$ ” originating from the center axis of the laser crystal slab are given in Figure 3.4. The first element in  $xy$ -plane is a cylinder between  $r = 0$  and  $r = 0.06$  mm. The second to the fourth elements are hollow cylinders from  $r = 0.06$  to  $r = 0.12$ ,  $r = 0.12$  to  $r = 0.24$ , and  $r = 0.24$  to  $r = 0.36$  respectively.

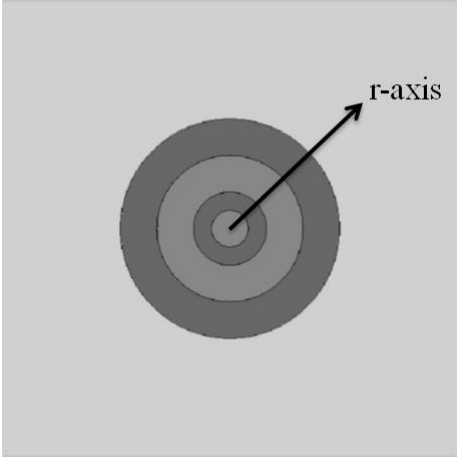


Figure 3.4 Discretized Elements in  $xy$ -Plane,  $r$ -Direction.

The discretization of the heat generation profile in this case is the discretization of Gaussian heat profile for the obtained heat generation through the crystal length as given in Figure 2.3. The discretization of the heat generation profile for the end surface elements  $z_1$  and  $z_{24}$  are provided in Figure 3.5. The discrete profile and the Gaussian profile are again in very good agreement.

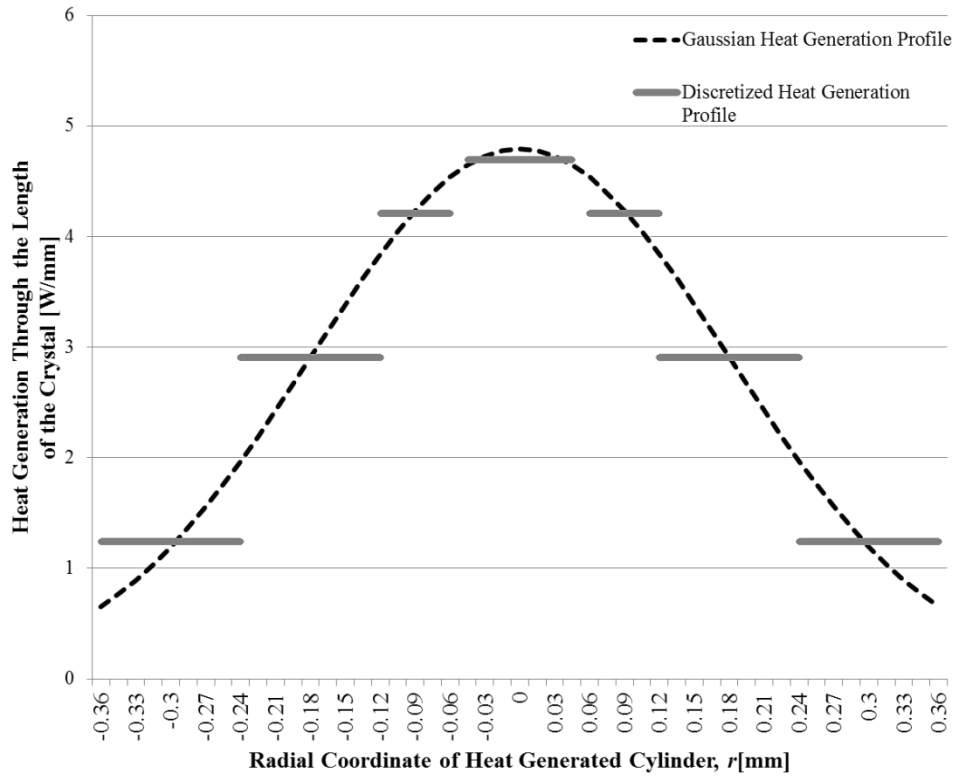


Figure 3.5 Continuous and Discretized Heat Generation in  $xy$ -Plane

The heat generation per unit volume has been calculated using the information provided in Section 2.2. Gaussian distribution function given in (2.1) and (2.2) have been utilized. Results are presented in Table 3.1.

The same procedure has been applied to the top-hat (uniform) heat generation profile, where only  $z$ -axis discretization is required.

Table 3.1 Volumetric Heat Generation Values Used in the Finite Element Model with Gaussian Distribution.

<b>Heat Generation [W/mm<sup>3</sup>]</b>	<b>z=0.0-0.5mm</b>	<b>z=0.5-1.0mm</b>	<b>z=1.0-1.5mm</b>	<b>z=1.5-2.0mm</b>	<b>z=2.0-2.5mm</b>	<b>z=2.5-3.0mm</b>	<b>z=3.0-3.5mm</b>	<b>z=3.5-4.0mm</b>
<b>r=0-0.06mm</b>	50.08	47.52	45.23	43.22	41.45	39.93	38.64	37.57
<b>r=0.06-0.12mm</b>	15.13	14.36	13.67	13.06	12.52	12.06	11.67	11.35
<b>r=0.12-0.24mm</b>	5.12	4.86	4.62	4.42	4.24	4.08	3.95	3.84
<b>r=0.24-0.36mm</b>	1.32	1.25	1.19	1.14	1.09	1.05	1.02	0.99
<b>Heat Generation [W/mm<sup>3</sup>]</b>	<b>z=4.0-4.5mm</b>	<b>z=4.5-5.0mm</b>	<b>z=5.0-5.5mm</b>	<b>z=5.5-6.0mm</b>	<b>z=6.0-6.5mm</b>	<b>z=6.5-7.0mm</b>	<b>z=7.0-7.5mm</b>	<b>z=7.5-8.0mm</b>
<b>r=0-0.06mm</b>	36.73	36.10	35.69	35.48	35.48	35.69	36.10	36.73
<b>r=0.06-0.12mm</b>	11.10	10.91	10.78	10.72	10.72	10.78	10.91	11.10
<b>r=0.12-0.24mm</b>	3.76	3.69	3.65	3.63	3.63	3.65	3.69	3.76
<b>r=0.24-0.36mm</b>	0.97	0.95	0.94	0.93	0.93	0.94	0.95	0.97
<b>Heat Generation [W/mm<sup>3</sup>]</b>	<b>z=8.0-8.5mm</b>	<b>z=8.5-9.0mm</b>	<b>z=9.0-9.5mm</b>	<b>z=9.5-10.0m</b>	<b>z=10.0-10.5m</b>	<b>z=10.5-11.0m</b>	<b>z=11.0-11.5m</b>	<b>z=11.5-12.0mm</b>
<b>r=0-0.06mm</b>	37.57	38.64	39.93	41.45	43.22	45.23	47.52	50.08
<b>r=0.06-0.12mm</b>	11.35	11.67	12.06	12.52	13.06	13.67	14.36	15.13
<b>r=0.12-0.24mm</b>	3.84	3.95	4.08	4.24	4.42	4.62	4.86	5.12
<b>r=0.24-0.36mm</b>	0.99	1.02	1.05	1.09	1.14	1.19	1.25	1.32

150318 quadrilateral elements with 744203 nodes are used in meshing of the laser crystal. The mesh structure can be seen in Figure 3.6. This crystal mesh system is used for all ANSYS analyses both with and without holders and for both Gaussian and uniform heat generation profiles to eliminate mesh related differences in the solution. This master mesh system is constructed using 0.08 mm maximum element size. Results are compared with a finer mesh system with 0.05 mm maximum element size and found that finer mesh does not change the temperature profile result by more than 1%.

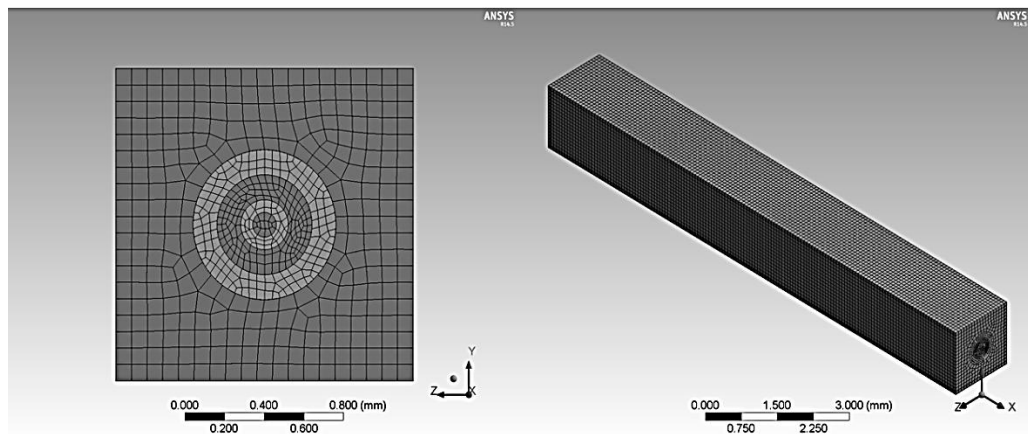


Figure 3.6 The Mesh Structure Used in Laser Crystal Slab for Gaussian Heat Generation.

Constant temperature boundary conditions are applied on the side surfaces and  $T_w$  is set to  $0^\circ\text{C}$  directly determine the temperature difference in the analysis. The other assumption used in the ANSYS model is that the thermal conductivity of Tm:YLF is assumed to be independent of the temperature and is  $0.6 \text{ W/m} \cdot \text{K}$ , for simplicity. In addition, a model with uniform heat generation in 1-plane with the same heat generation volume is constructed. As it is debated in Section 1.2, the pumping profile of the system is between uniform heat generation and a Gaussian one. Hence, both cases have been investigated and the real laser system behavior is expected to be in between these two cases.

Using the thermal data obtained from the Steady-State Thermal Module and Static Structural Module of ANSYS, thermal stress analyses have been conducted. The initial temperature of the system is taken to be  $0^\circ\text{C}$  and the steady-state temperature of the system taken from the Steady-State Thermal Module is considered as the thermal load and no other constraints or loadings are defined on the crystal. The aim of this analysis is to compare the stress effects of the cooling geometries on the crystal without considering the crystal holders. For

this reason, only the thermal stress due to thermal gradient has been taken into account.

Three principal stresses and a safety factor computation applying Mohr-Coulomb theory with constant tensile and compression limits, 40 MPa and 100 MPa respectively, have been performed. The 40 MPa tensile limit information is provided by the manufacturer of the crystal and can also be found in literature [40, 49]. However, the compression limit is unavailable. Due to the fact that YLF is a crystal, it is brittle and as a lasing medium application, the failure is expected to be from tensile stress in the crystal. For this reason, a high compression limit of 100 MPa has been assumed to investigate the safety factor due to tension only.

### **3.3. Temperature Dependent Optical Path Difference (OPD) and Calculation of the Thermal Lens Radius**

Since the refractive index ( $n$ ) is a temperature dependent property, non-uniform temperature distributions with temperature gradients cause gradients in the refractive index. As mentioned in the Introduction chapter, the refractive index gradients ( $\Delta n$ ) along the fast-axis of the gain medium can cause thermal lensing due to the non-uniform optical path difference (OPD) generation. Another source of the OPD is the non-uniformity of the thermal expansion along the traverse-plane.

OPD is the phase shift that appears between previously coherent sources when they passed through media with different refractive indices and/or different path lengths. Considering two coherent light waves, one passing through glass and the other passing through air for the same path length, the former light travels a greater distance than the latter due to the lower speed and greater number of wavelengths covered in glass media due to higher refractive index.

The OPD in laser gain medium may be calculated as

$$\begin{aligned}
OPD &= \left\{ \underbrace{\Delta T \cdot \frac{dn}{dT} \cdot L}_{\text{due to refractive index gradients } (\Delta n)} \right\} + \left\{ \underbrace{\Delta T \cdot \alpha \cdot L}_{\text{due to thermal expansion}} \right\} \\
&= (\Delta T \cdot L) \cdot \left[ \frac{dn}{dT} + \alpha(T) \right] \tag{3.22}
\end{aligned}$$

where  $\Delta T$  is the temperature difference between two points on the optical path in the laser gain medium, and the  $L$  is the distance between those two points.  $dn/dT$  is the temperature coefficient of refractive index which is a material property dependent on the temperature and the wavelength, and  $\alpha$  is the coefficient of thermal expansion.

By calculating the OPD values for discrete optical paths through laser gain medium, radius of curvature of thermal lensing can be estimated by a paraboloid as [53]

$$OPD(x, y) = \frac{2\pi}{\lambda} (P + T_x x + T_y y + \alpha x^2 + \beta y^2 + \gamma xy) \tag{3.23}$$

where  $P$  is the constant ‘‘piston’’ term,  $T_x$  and  $T_y$  are ‘‘tilt’’ terms in  $x$  and  $y$ -axes,  $\alpha$  and  $\beta$  are ‘‘defocus’’ terms and  $\gamma$  is the ‘‘astigmatism’’ term. The  $2\pi/\lambda$  term is the propagation constant of the medium. The thermal lensing effects are governed by the second order terms ( $\alpha$  and  $\beta$ ) only, piston, tilt and astigmatism terms do not contribute to the beam divergence [53]. Astigmatism distorts the beam divergence but has been ignored in this study. Hence, the OPD takes the form

$$OPD(x, y) = \frac{2\pi}{\lambda} \left[ \frac{x^2}{2R_x} + \frac{y^2}{2R_y} \right] \tag{3.24}$$

Equation 3.24 exhibits the relation between the radius of curvature and the OPD. Using (3.23) and (3.24), the thermal lens radius in  $x$ - and  $y$ -axes are found as

$$R_x = \frac{1}{2\alpha} \text{ and } R_y = \frac{1}{2\beta}. \tag{3.25}$$

The calculation of the thermal lens radii for the cases described in the following sections will be performed using (3.23) and equation (3.25).

For the ODP calculations, the temperature along the optical path has been taken from the analytical thermal solution or the finite element solution. The other required parameters are  $\alpha$  (the coefficient of thermal expansion, CTE) and  $dn/dT$  of the Tm:YLF crystal for  $\lambda = 1908$  nm, which is the wavelength of the laser beam. The CTE of the Tm:YLF crystal within a temperature range of 0-100°C is given as [54]

$$\text{CTE of Tm:YLF (0 – 100°C): } \begin{cases} \text{for } a\text{-axis: } 13.8 \cdot 10^{-6} \text{°C}^{-1} \\ \text{for } c\text{-axis: } 9.0 \cdot 10^{-6} \text{°C}^{-1} \end{cases}$$

where  $a$ - and  $c$ -axes are crystallographic axes of the tetragonal YLF crystal system. The lensing effect caused by thermal expansion is in the fast-axis direction, which generates OPD. The fast-axis of the crystal is the  $a$ -axis, so the CTE term used in the calculations is  $\alpha = 13.8 \cdot 10^{-6} \text{°C}^{-1}$  and is independent from the temperature in the thermal range of the problem.

The temperature coefficient of the refractive index of the Tm:YLF crystal for different wavelengths are given as [54, 55]

$$\frac{dn_{\sigma}}{dT} = \begin{cases} -0.54 \cdot 10^{-6} \text{°C}^{-1} @ 435.8 \text{ nm} \\ -0.67 \cdot 10^{-6} \text{°C}^{-1} @ 546.1 \text{ nm} \\ -0.91 \cdot 10^{-6} \text{°C}^{-1} @ 578.0 \text{ nm} \\ -2.00 \cdot 10^{-6} \text{°C}^{-1} @ 1060 \text{ nm} \end{cases}$$

The subscript  $\sigma$  refers to the extra-ordinary axis, which corresponds to the fast-axis.  $dn_{\sigma}/dT$  for 1908 nm has been found by the extrapolation of the above data as  $-3.50 \cdot 10^{-6} \text{°C}^{-1}$ . This estimation can be improved by using an experimental value, but since the thermal lens radius determination is to be used for the comparison of the cooling geometries, using the exact value is not crucial.

### **3.4. Comparison of the Analytical and Finite Element Solutions for the 4-Face Cooling Case and Validation of the Finite Element Model**

The analytical steady-state thermal solution of the end-pumped laser slab problem has been constructed using the method proposed by Tilleman [18]. The MATLAB code for the solution is given in Appendix C. The finite element model of the same problem with single end-pumping with some simplifications and discretization of heat generation has been constructed in the ANSYS Workbench Environment.

To compare the FEM and the analytical solution, line segments along the optical path of the laser beam have been constructed and mapped. In addition, vertical and horizontal paths along the cross-section of the laser slab for the end-surface and middle-surface have been created. Since the simulated laser beam diameter throughout the crystal was about 590  $\mu\text{m}$ , considering only the temperature profiles in the cylindrical volume with diameter 590  $\mu\text{m}$  from the center axis of the slab has been sufficient to determine the thermal effects on the laser beam. However, in this thesis, an extended cylindrical volume of diameter 720  $\mu\text{m}$  instead of 590  $\mu\text{m}$  has been considered since the extensive effect of heat generation can be investigated if the temperature profile is observed at the heat generated volume boundaries. Figure 3.7 shows the paths and mapping used for the solution. Numbers indicate the path number and paths are linear with starting point A and ending point B.

The temperature profiles through paths parallel to the fast-axis ( $z$ -axis) for  $r = 0$  mm (center-axis) and  $r = 0.32$  mm (radius of the pump beam) have been plotted in Figure 3.8. The temperature profile for  $r \geq 0.32$  mm is the same for both analytical and FEM solutions, for  $r < 0.32$  mm there is a slight difference between the two solutions and the deviation maximizes at  $r = 0$ . The reason for this error in the finite element model is the discretization of the Gaussian energy distribution in the  $xy$ -plane perpendicular to the beam path. As it can be seen from Figure 3.8 the difference is very small even at  $r = 0$ . Increasing the number

of discrete elements in the  $xy$ -plane reduces this error. For the current case (4 element discretization on the  $xy$ -plane), the maximum error is  $\sim 3\%$ . The other finite element discretization has been performed along the fast-axis ( $z$ -direction). It can be observed from both  $r = 0$  and  $r = 0.32$  mm solutions that this discretization gives very accurate results, there is no need to increase the discretization step in the  $z$ -direction or in  $xy$ -plane.

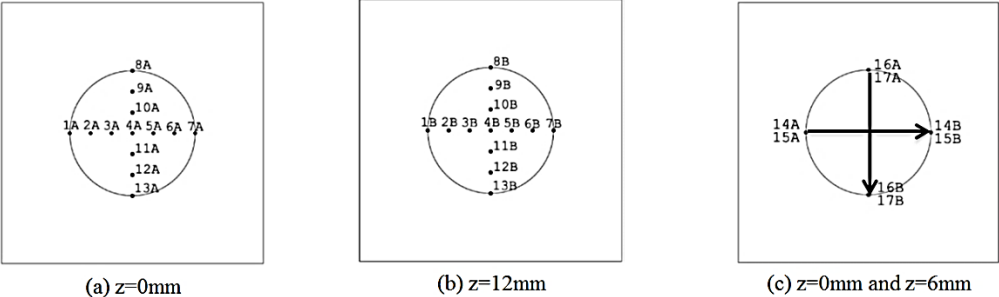


Figure 3.7 Paths and Mapping Used to Determine the Temperature Profiles in the Laser Crystal Slab.

As expected, a very large temperature difference of  $\sim 60^\circ\text{C}$  occurs over a distance of only 0.36 mm, which can be observed at  $z = 0$  of the center-axis in Figure 3.8.

The analytical and finite element solutions for the OPD have been conducted following the steps provided in Section 3.3. The OPD results for the analytical and finite element solutions are presented in Figure 3.9Figure 3.12. A smaller thermal lens radius,  $R$  means a stronger lens effect, therefore poorer laser beam quality.

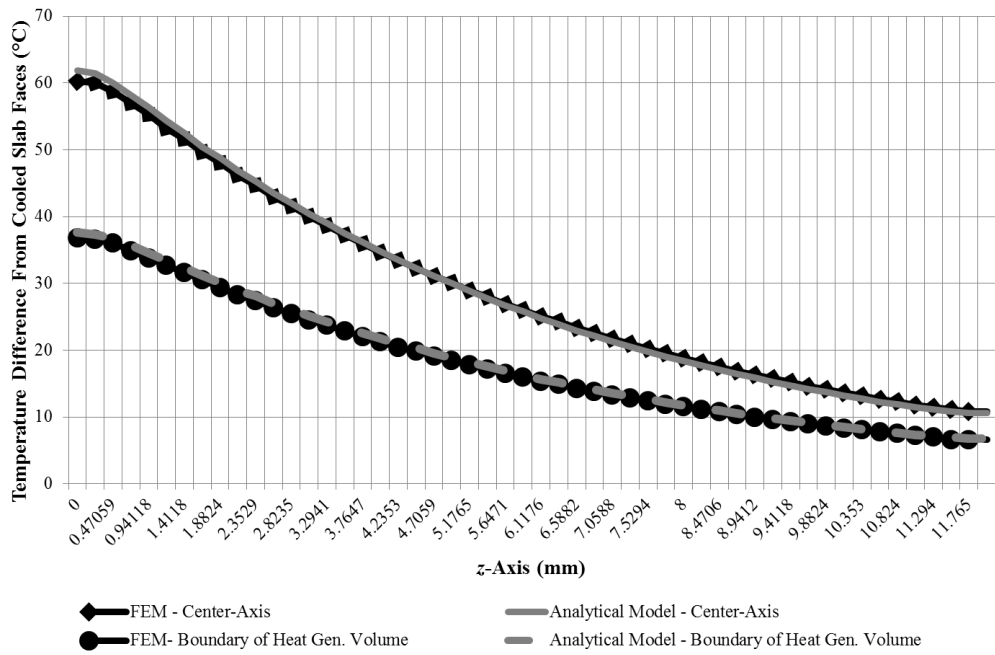


Figure 3.8 Comparison of Temperature Profiles Obtained from Analytical and Finite Element Solutions

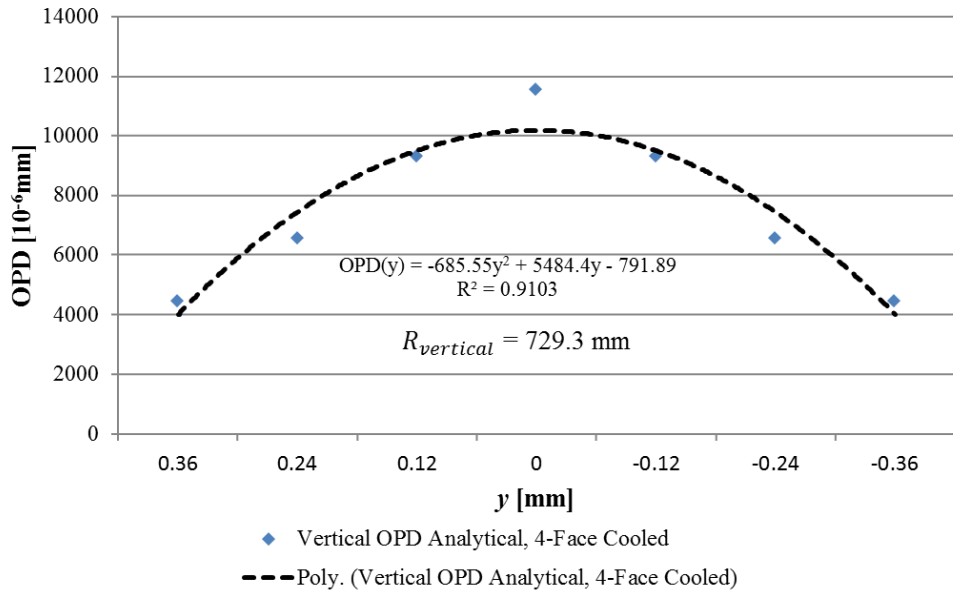


Figure 3.9 Analytically Obtained Vertical OPD Profile for the 4-Face Laser Crystal Slab Cooling.

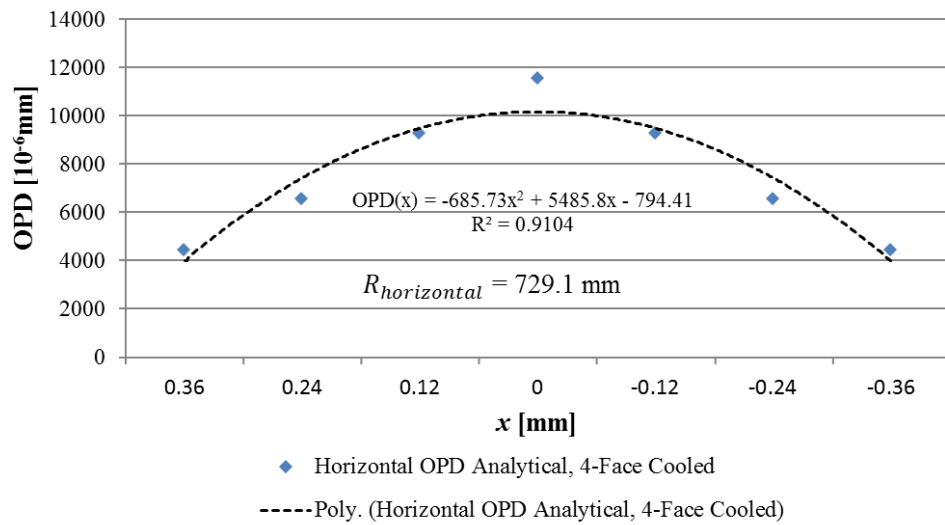


Figure 3.10 Analytically Obtained Horizontal OPD Profile for the 4-Face Laser Crystal Slab Cooling.

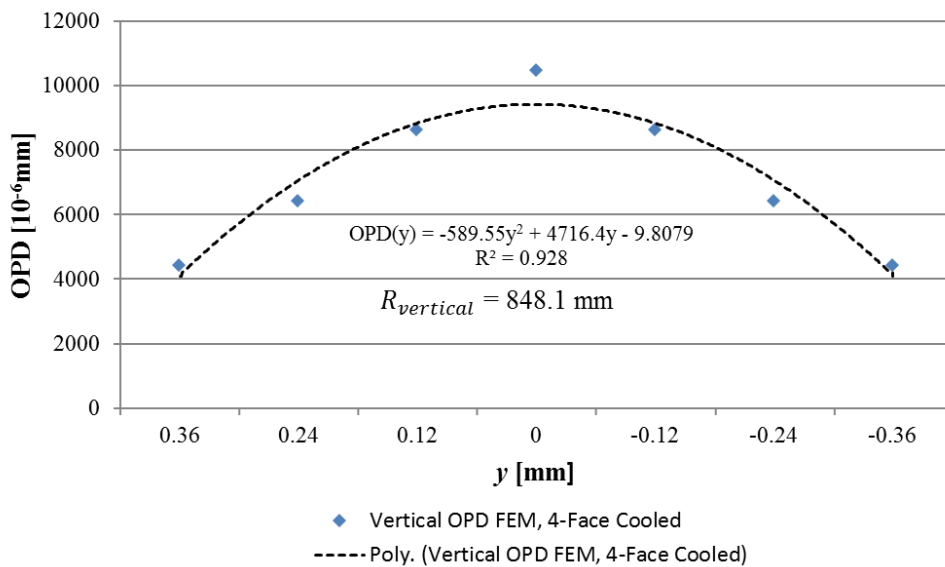


Figure 3.11 Vertical OPD Profile Obtained by FEM for the 4-Face Laser Crystal Slab Cooling.

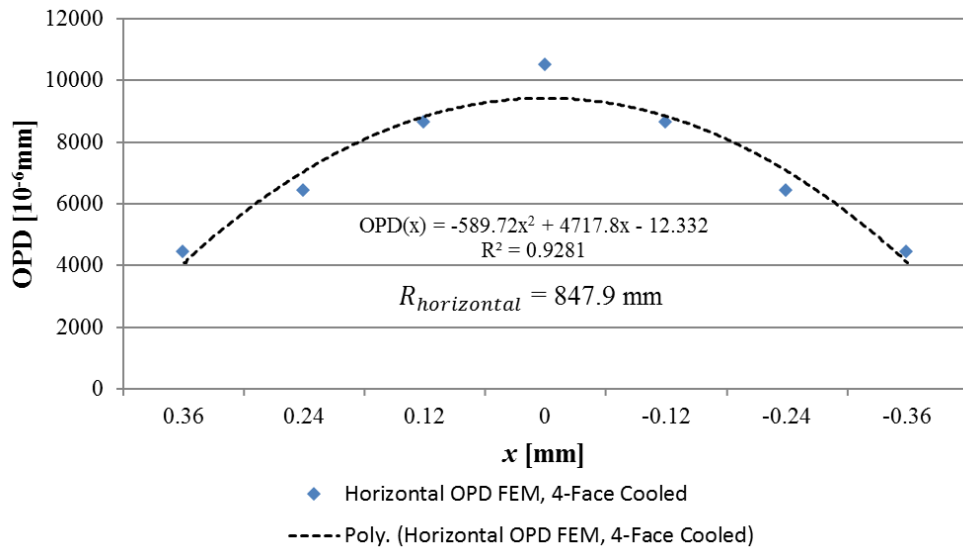


Figure 3.12 Horizontal OPD Profile Obtained by FEM for the 4-Face Laser Crystal Slab Cooling.

There is ~9% error in the thermal lens radius between the analytical and numerical solutions. This is an expected result since due to the discretization, the temperature gradients are less steep in the finite element solution. Furthermore, since the governing equation of the problem has only a diffusion term (no advection or convection terms), a finite element model with fine meshing and good discretization is bound to provide accurate results.

As expected, due to the symmetry in the cooling geometry and a cylindrical heat load zone, the vertical and horizontal temperature profiles, hence, the vertical and horizontal OPD profiles are very similar. In fact, the two are expected to be equal, but the very small difference is believed to be due to a round off error both in the FEM and analytical solutions.

Overall, the finite element model generated in ANSYS Workbench environment using the simplifications stated in Section 3.2 is a valid tool to compare the thermal effects of cooling and holder geometries. This is a predictable result

since the problem is steady-state and purely diffusional with no advection term (convection) being present. For a fine enough mesh structure, the only considerable error may be due to the discretization of the heat generation.

In Section 2.2, the heat generation profile in the  $xy$ -plane is mentioned to be between Gaussian and uniform. For this study, validation of the finite element model has been performed considering Gaussian heat generation for the case in which four side-surfaces are cooled since the Gaussian profile is easier to handle in Cartesian coordinates compared to uniform heat generation. For the compared cases with crystal holders, the finite element analysis with uniform heat generation in the  $xy$ -plane and the discretized generation in the  $z$ -direction are used, due to the fact that the temperature distribution in the no-heat-generation zone of the system is independent of the heat generation profile in the pumped zone. A more detailed information in this topic is provided in Section 5.4.

### **3.5. Comparison of the Temperature Distribution for Different Cooling Geometries of the Laser Crystal Slab**

ANSYS models have been prepared using the principles presented in Section 3.2 to determine the temperature profiles in the Tm:YLF laser crystal for both Gaussian and uniform heat generation profiles with equal heat generated volumes. The considered cooling geometries are given in Figure 3.13 as 1-face, 2-face (parallel) and 4-face cooling. Only the laser crystal is considered in these analyses as the boundary conditions are directly applied onto the side surface(s) of the laser crystal.

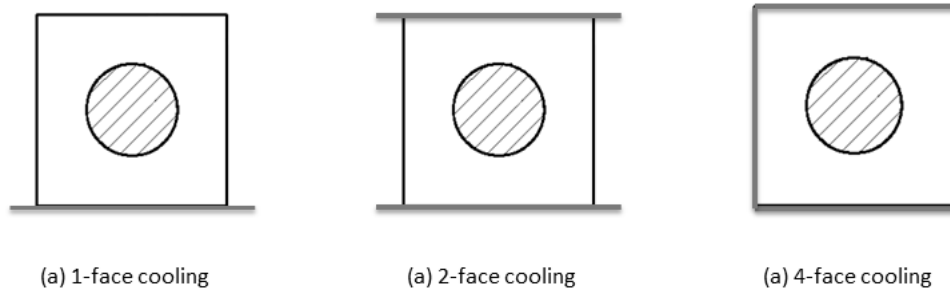


Figure 3.13 Illustration of (a) 1-Face, (b) 2-Face, and (c) 4-Face Cooling Geometries

The temperature profiles at the end surfaces for both Gaussian and uniform pumping and for different face cooling cases are illustrated in Figure 3.14 to Figure 3.16.

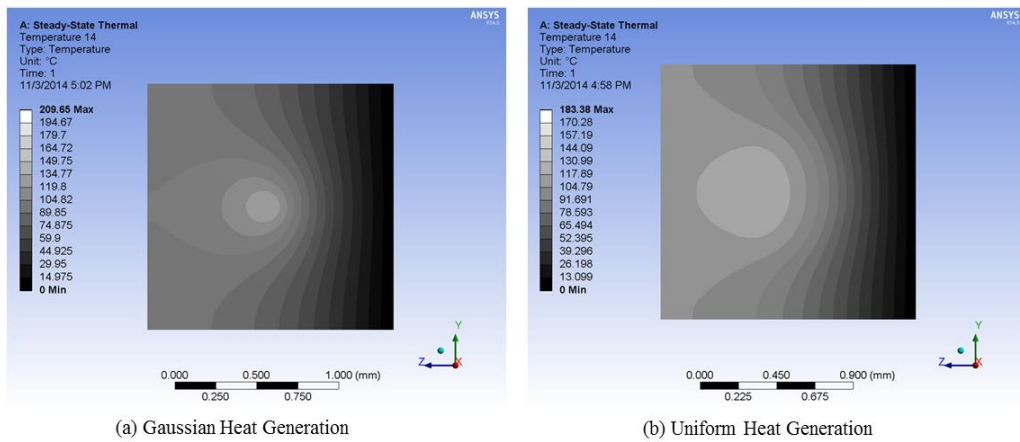
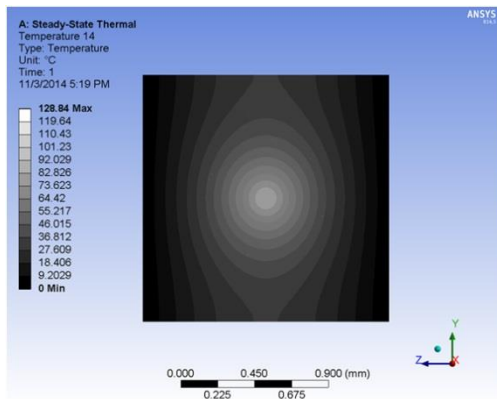
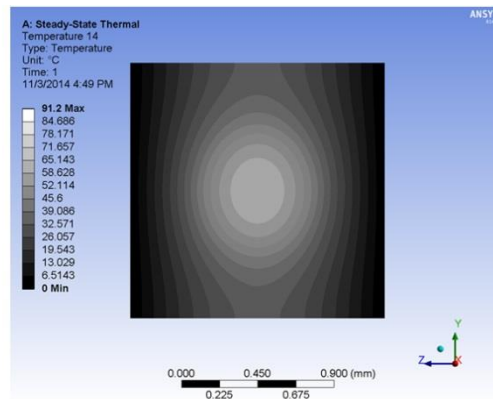


Figure 3.14 End Surface Temperature Profiles for the 1-Face Cooling Case with (a) Gaussian and (b) Uniform Heat Generation Profile

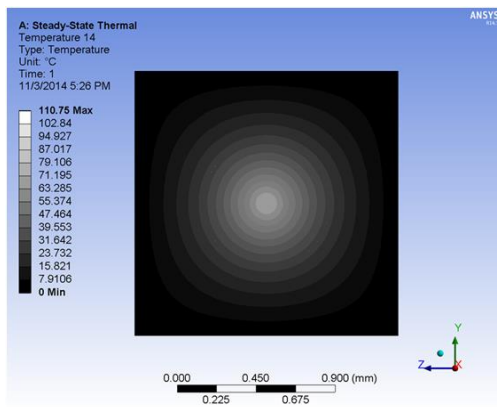


(a) Gaussian Heat Generation

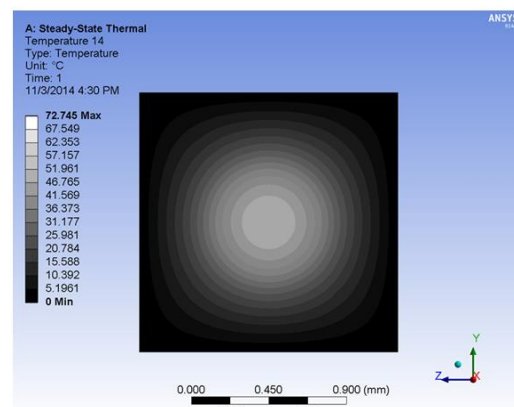


(b) Uniform Heat Generation

Figure 3.15 End Surface Temperature Profiles for the 2-Face Cooling Case with  
(a) Gaussian and (b) Uniform Heat Generation Profile



(a) Gaussian Heat Generation



(b) Uniform Heat Generation

Figure 3.16 End Surface Temperature Profiles for the 4-Face Cooling Case with  
(a) Gaussian and (b) Uniform Heat Generation Profile

Considering Gaussian and uniform heating cases, unlike 1-face cooling, the 2-face and 4-face cooling geometries provide axi-symmetric temperature profiles. 1-face cooling yields a flame-like a symmetric hotspot, 2-face cooling an elliptic hotspot and 4-face cooling a more circular hotspot.

The results are compared in Table 3.2. For the lensing effects, only the pumped area has been considered since the output laser dimensions cannot exceed the pumping cross-section for an end-pumped solid-state laser.

Table 3.2 Comparison of the Single Crystal Cooling Cases

Cooling Method		Average Temperature (°C)	Maximum Temperature (°C)	Thermal Lens Radius Vertical (mm)	Thermal Lens Radius Horizontal (mm)	Principle Stresses (MPa)	Safety Factor
1-Face Cooled	Uniform	133.73	183.34	1370	2011	67.1 and -36.05	0.5955
	Gaussian	143.04	208.38	707	847	69.7 and -61.68	0.5738
2-Face Cooled	Uniform	63.43	91.21	1358	2028	67.5 and -36	0.5922
	Gaussian	72.68	129.14	704	850	69.9 and -61.65	0.5712
4-Face Cooled	Uniform	47.88	72.75	1611	1610	51.88 and -37.1	0.7691
	Gaussian	57.13	111.06	766	767	54.65 and -62.56	0.7304

For all cooling geometries, the uniform heat generation provides lower average and maximum temperatures, and decreases the thermal lensing effect by increasing the thermal lensing radius. The same can be said for the thermal stresses. Comparing the cooling cases, it can be seen that, 4-face cooling is superior to 1-face and 2-face cooling in all aspects but the horizontal thermal lens radius. However, as the horizontal and vertical lens radii are equalized, 4-face cooling is a more preferable option even though it has a greater horizontal thermal lensing effect. In fact, equal lensing can be compensated by a single lens or by using a curved output coupler.

For all cooling cases, the uniform pumping profile yields 7-16% lower maximum and average temperature, about twice the thermal lens radius (nearly half the

thermal lens effect), and about 3.8% increase in the mechanical safety factor due to thermal stresses. 4-face cooling yields superior thermal and thermo-optical results than 1-face and 2-face cooling for both heat generation profiles. Average and maximum temperatures are about 25% less than 2-face cooling and 65% less than 1-face cooling. Also, the safety factor of 4-face cooling is 30% higher than 1-face and 2-face cooling. Considering the thermal lens radius, 4-face cooling underperforms in horizontal axis, but it is still favorable as it yields equal thermal lens radii in both horizontal and vertical directions which is easier to compensate in resonator structure with standard optical components.

The safety factor solutions point out fracture for all cases, but the results yield enough mechanical information to compare the cooling alternatives. For both 1-face and 2-face cooling cases, uniform heat generation provides  $\sim 3.8\%$  higher safety factor than Gaussian pumping. The increase in safety factor scales up to  $\sim 5.3\%$  for the 4-face cooling. Considering average safety factor values of the uniform and Gaussian pumping, the 2-face cooling yields  $\sim 0.5\%$  lower mechanical safety factor than 1-face cooling, whereas the 4-face cooling provides  $\sim 30\%$  higher mechanical safety factor than both 1-face and 2-face cooling geometries.

Even though the thermal lens radii of 1-face cooling are close to the ones of 2-face cooling, there exists a great tilt in the OPD analysis. This tilt may disrupt the resonator, causing lasing to not initiate.

The greatest thermal and thermo-optical differences between 2-face and 4-face cooling occur due to the increase in the symmetric cooling surfaces. For a slab of near-unity aspect ratio, such as the system used in this thesis, the symmetric cooling surfaces have been increased two folds. It can be predicted that as the aspect ratio increases, and the difference between the symmetric cooling surfaces of the laser slab for 2- and 4-face cooling decreases, the thermal and thermo-optical differences between the two also decrease. In other words, the maximum

benefit of the 4- over 2-face cooling is expected for laser slabs of near-unity aspect ratio.

For OPD calculations, it has been observed that, in Tm:YLF, OPD generation due to thermal expansion coefficient is more dominant than that due to refractive index gradient.



## CHAPTER 4

### LASER CRYSTAL HOLDER GEOMETRIES AND FINITE ELEMENT ANALYSIS OF THE COMPOSITE SYSTEM

In Chapter 3, thermal analyses considering only the laser crystal slab have been conducted. This is the common approach used in the literature, except for the direct fluid flow cooling of the laser crystal. A more realistic analysis may be conducted on a composite laser crystal and crystal holder system, where the boundary conditions are applied on the holder.

In the previous chapter, where only the laser crystal slab was considered and the boundary conditions were applied on the side-surface(s) of the laser crystal slab, the cooling type was referred as face-cooling. Now, the cooling type when the composite system is considered and the laser crystal slab is indirectly cooled by the contact between the crystal and the cooling applied holder will be referred as side-contact cooling. In side-cooling cases, constant temperature boundary condition is applied to the holders.

Both Gaussian and uniform pumping have been considered in the previous chapter for the face-cooling cases. It was concluded that the temperature profile within the boundaries of the heat generated zone, as well as the applied area of the boundary conditions were the same for both pumping profiles. as the total heat load was taken constant for both cases. For this reason, only the uniform heat generation profile has been investigated in this chapter. The difference between the Gaussian and uniform heat generation profiles for the side-contact-cooling cases are expected to be equivalent of those for the face-cooling cases.

Just like in the previous chapter, only a steady-state thermal analysis has been conducted since the thermal effects are the most critical in thermal equilibrium [35, 36]. Since the only material property that affects the steady-state thermal outcome of the system is the thermal conductivity, holders made out of copper and aluminum have been analyzed with the same holder geometries.

The dimensions of the holders are selected so that the cooling surfaces match with commercial TEC modules that can discharge the heat load of the laser crystal to a commercial heat sink for a broad ambient temperature range, as discussed in the introduction chapter. The distance between the center axis of the laser crystal slab and the applied area of the boundary conditions has been considered constant at 6.75 mm for all cases. This yields enough space for heat dissipation in the holders.

### 4.1.1-Side Contact Laser Crystal Slab Holder System

In this section, a more realistic cooling case of the 1-face cooled crystal has been analyzed. For the same laser crystal slab, a conceptual laser crystal holder has been constructed and analyzed. The 1-side contact laser crystal holder dimensions and the corresponding 1-face cooled crystal previously analyzed are shown in Figure 4.1.



Figure 4.1 Geometry of the 1-Face Cooling Case and the Corresponding 1-Side Contact Cooling Case.

The same mapping system shown previously in Section 3.4 has been used and the temperature profiles through these linear paths have been obtained. The maximum and minimum temperature gradients along the  $r$ -axis occur at the end surfaces and the middle surface, respectively. The vertical and horizontal temperature profiles for 1-side contact crystal cooling with aluminum alloy and copper alloy crystal holders, as well as those for 1-face cooling are plotted in Figure 4.2 and Figure 4.3.

An important factor that cannot be overlooked is the huge tilt of the temperature profile in 1-side and 1-face cooling cases. As mentioned before, this tilt may not affect the laser beam quality, but disrupts the coupling between the reflector and the output coupler of the resonator (coupling between HR and PR mirrors) which may yield disruption in the lasing process.

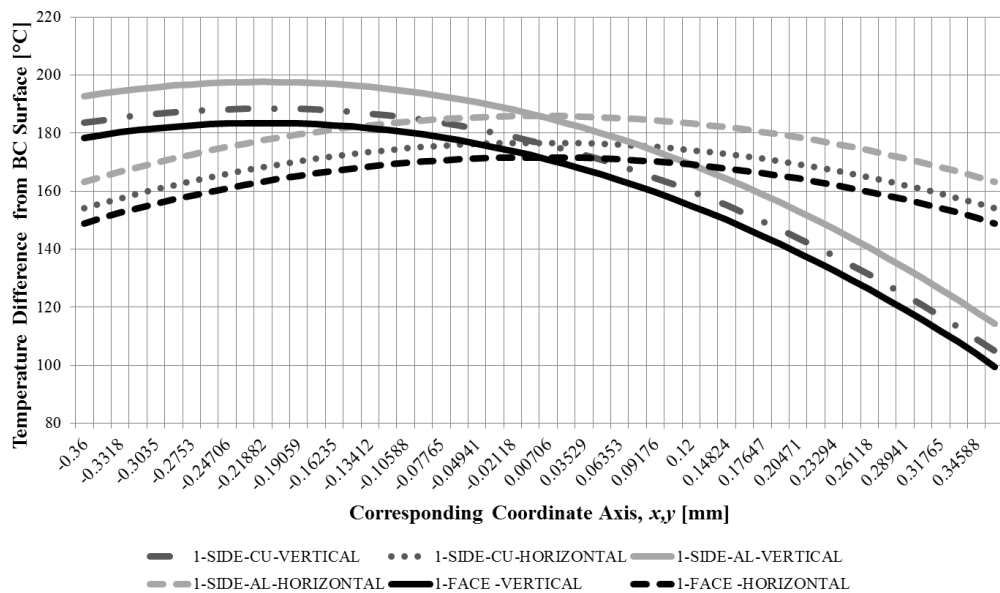


Figure 4.2 Comparison of the End Surface Temperature Profiles for 1-Side Cooled Crystal with Al and Cu Holders, and 1-Face Cooled Crystal

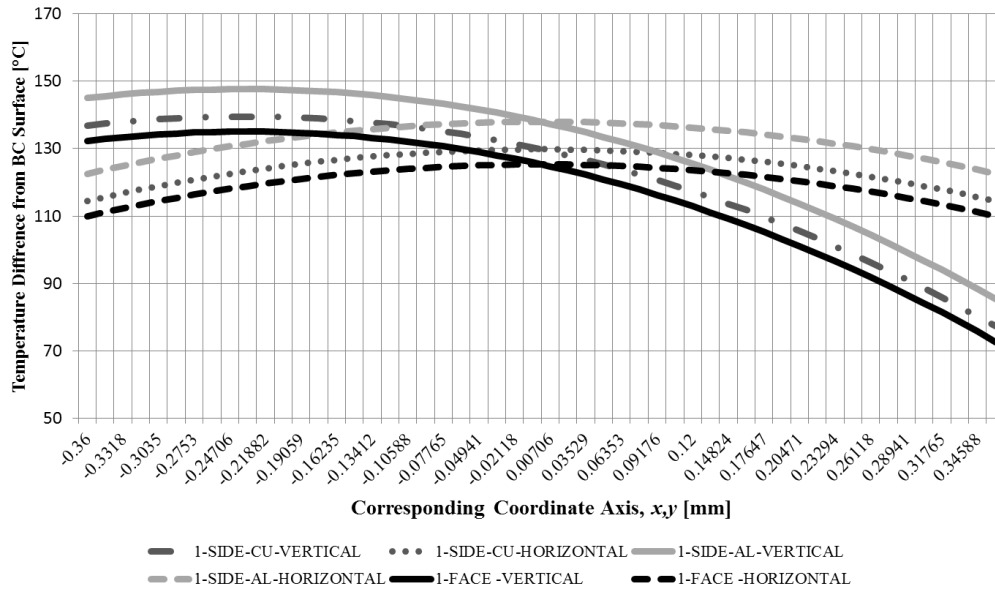


Figure 4.3 Comparison of the Middle Surface Temperature Profiles for 1-Side Cooled Crystal with Al and Cu Holders, and 1-Face Cooled Crystal

The copper crystal holder apparently yields closer results to face-cooling case due to its higher thermal conductivity than that of aluminum. When closely investigated, both aluminum and copper crystal holders only affect the temperature profiles by introducing a certain close-to-constant value temperature offset. To clearly illustrate this, the mean values of the temperature profile differences between the composite and crystal only cases, and their average deviations have been calculated. The results are tabulated in Table 4.1.

The mean values of the temperature profile differences have been obtained by calculating the mean value of the temperature difference between 1-face cooling and 1-side-contact-cooling at all discrete points along the end and middle surface paths. Also the averages of absolute deviations from the mean value of the

temperature difference between 1-face cooling and 1-side-contact-cooling at all discrete points along the end and middle surface paths have been calculated and tabulated.

This temperature difference should not be mistaken with the temperature difference occurring inside the laser crystal slab, which is independent of holder material. The tabulated temperature difference is the mean difference induced in the crystal slab due to the introduction of conduction thermal resistance of the holder.

Table 4.1 The Mean Values of the Temperature Profile Differences Between 1-Side Contact Crystal Holder and Single Crystal with the Average Deviations

Laser Slab Surface	Temperature Profile	Holder Material	Mean Value of the Temperature Difference (°C)	Average of Absolute Deviations (°C)	Ratio of Mean Values (Cu/Al)
End Surface Profile	Vertical	Cu	5.03	0.0190	0.3529
		Al	14.25	0.0728	
	Horizontal	Cu	5.02	0.0108	0.3532
		Al	14.21	0.0122	
Middle Surface Profile	Vertical	Cu	4.48	0.0192	0.3541
		Al	12.64	0.0154	
	Horizontal	Cu	4.47	0.0068	0.3544
		Al	12.62	0.0097	

The low average deviations indeed indicate that the crystal holder introduces only a constant temperature offset to the temperature distribution as mentioned above. The ratio of the mean temperature difference values for copper and aluminum holders are almost equal (0.35), for all cases. As the ratio 0.35 is very close to the ratio of the thermal conductivities of the materials, the constant offset has been proved to be due to the conductive thermal resistance introduced by the holders. This thermal resistance can be calculated using the thermal

conductivity of the holder material, the geometry of the holder and the applied area of the constant temperature boundary condition as

$$R_{cond} = \frac{L_{ht}}{k \cdot A_{ht}} = \frac{\Delta T}{\dot{Q}} \quad (4.1)$$

where  $L_{ht}$  is the effective heat transfer length,  $k$  is the thermal conductivity and  $A_{ht}$  is the effective heat transfer area along  $L_{ht}$ .  $\Delta T$  is the temperature difference between the two end points of  $L_{ht}$  and  $\dot{Q}$  is the heat transfer rate through  $L_{ht}$ .

The copper holder of the 1-side contact cooling case has  $L_{ht} = 6 \text{ mm}$ ,  $k = 400 \text{ W}/(\text{m} \cdot \text{K})$ . Even though the holder has dimensions of  $30 \times 6 \times 12 \text{ mm}^3$ , as the heat enters the holder from the  $1.5 \times 12 \text{ mm}^2$  area, is discharged to an area of  $30 \times 12 \text{ mm}^2$ , the effective heat transfer area cannot be taken as  $30 \times 12 \text{ mm}$ . Assuming that the heat transfer region in the holder is as shown in Figure 4.4, an equivalent estimate of conduction resistance can be calculated as

$$R_{cond\_estimation} = \int_0^{6\text{mm}} \frac{dx}{k \cdot A(x)} = 0.251 \text{ K/W} \quad (4.2)$$

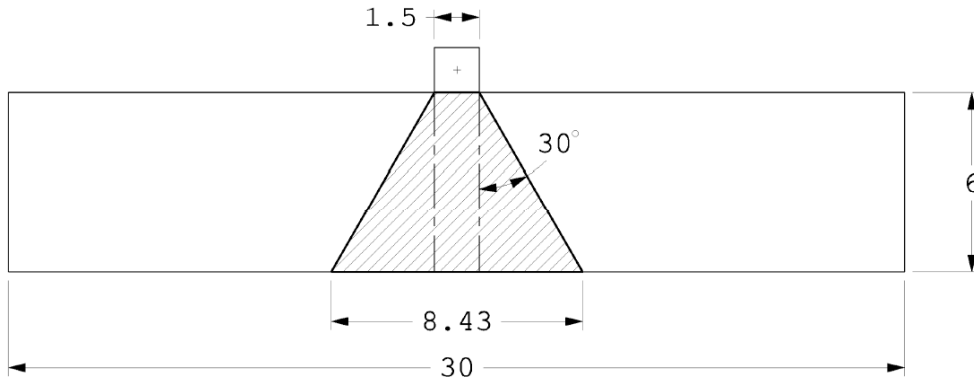


Figure 4.4 Heat Transfer Region in the 1-Side Contact Crystal Holder

It should be noted that the average  $\Delta T$  through the fast axis is  $4.81^\circ\text{C}$  and all  $20.1 \text{ W}$  heat load is discharged from a single holder. Then the resistance analysis

using the simulation data suggests that  $R_{\text{cond\_simulation}} = 0.24 \text{ K/W}$ . Both resistance values are similar. This indicates that, a thermal resistance estimation using (4.2) and the geometry shown in Figure 4.4 gives a close approximation of the real case. Using this procedure, the analyses performed in the literature for only face cooling or analytical solutions considering only the laser crystal slab can be adjusted to reflect the effects of the crystal holder.

This method is error-prone, since the heat generation along the fast-axis is not constant so the crystal surface, which is considered to be at a constant temperature for the face cooling case, is not exactly a constant temperature surface for the composite case with the crystal holder. From Table 4.1 it can be observed that for a cross-section along the fast-axis the deviation of the temperature difference is negligible. The deviation through the fast-axis should also be considered to check if the face-cooling approach with constant temperature boundary condition is an applicable assumption for 1-side contact cooling case with the holder. The average deviations of the temperature profile differences between 1-face cooling and 1-side cooling, for copper and aluminum holders, calculated along the paths mentioned in Chapter 2, have been calculated as  $0.179^\circ\text{C}$  and  $0.492^\circ\text{C}$ , respectively. These slight deviations suggest that the non-uniformity of the heat generation along the fast-axis has no effect on the temperature increase along the length of the slab introduced due to the crystal holder. Then, by simply adding the temperature increase caused by the thermal resistance of the holder, the constant temperature boundary condition applied on the holder can be estimated from the knowledge of the boundary condition for the face-cooling case. When compared to the simulation results, the error of this estimation, which is introducing the thermal effect of the holder as a constant conductive thermal resistance for 1-side cooling have been calculated as 0.11% and 0.30% for copper, and aluminum holders, respectively. As was expected, copper has a lower error than aluminum due to its superior thermal conductivity. In any case, the errors are negligible. It should be noted that the temperature profiles near the crystal side-surfaces are bound to have greater errors. However,

since the temperature profiles in the close proximity of the center axis of the slab are crucial to determine the thermal effects on the laser beam and as the errors are negligibly small, the assumption of face cooling is a valid assumption. It can further be improved by just adding the temperature increase caused by the holder to the boundary condition.

The OPD analysis on cooling with 1-side contact holder showed a similar trend. As was given in Table 3.2 the vertical and horizontal thermal lens radii for the 1-face cooling case were 1370 mm and 2011 mm, respectively. For the 1-side contact cooling case with copper holder the vertical and horizontal thermal lens radii have been calculated as 1380 mm and 2025 mm, respectively. The corresponding values for the aluminum holder are 1382 mm and 2021 mm. Since the addition of the holder only increases the piston term in the OPD, and the thermal lens radius is independent of this term, the thermal lensing effect does not change with the addition of the holder.

#### **4.2.2-Side Contact Laser Crystal Slab Holder System**

In this part, a more realistic case, namely, the 2-face symmetrically cooled crystal has been investigated. For the same laser crystal slab, a conceptual laser crystal holder has been constructed and analyzed. The dimensions of the 2-side contact holder dimensions and the corresponding 2-face cooled crystal case are shown in Figure 4.5. Both 2-face cooling and the corresponding 2-side contact cooling are symmetrical cooling options.

The same mapping and the same procedure described for the 1-side contact cooling have been employed for this case as well. Comparative plots of the vertical and horizontal temperature profiles for 2-side contact crystal cooling with aluminum alloy and copper alloy holders, as well as for 2-face cooling are plotted in Figure 4.6 and Figure 4.7.

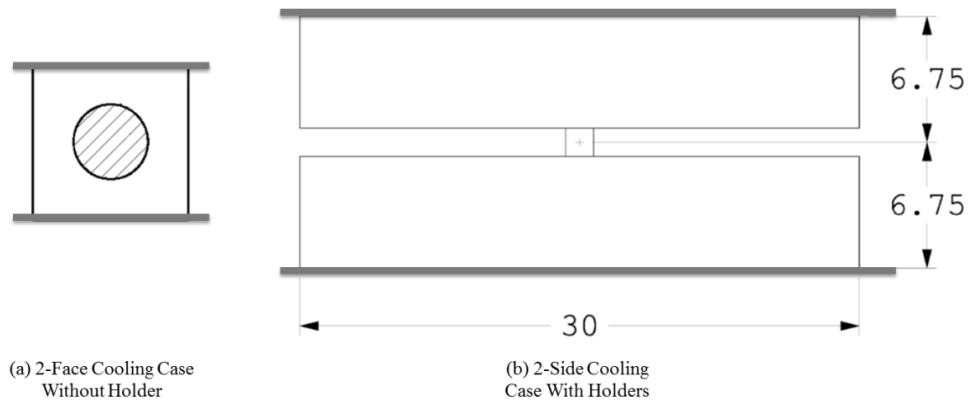


Figure 4.5 2-Face Cooling Geometry and the Corresponding 2-Side Cooling Geometry

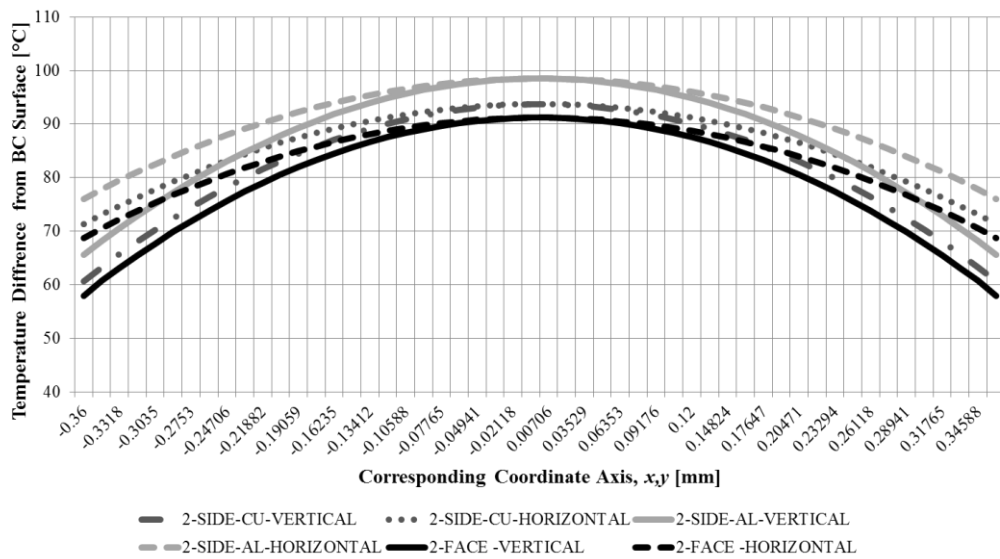


Figure 4.6 Comparison of the End Surface Temperature Profiles for 2-Side Cooled Crystal with Al and Cu Holders, and 2-Face Cooled Crystal

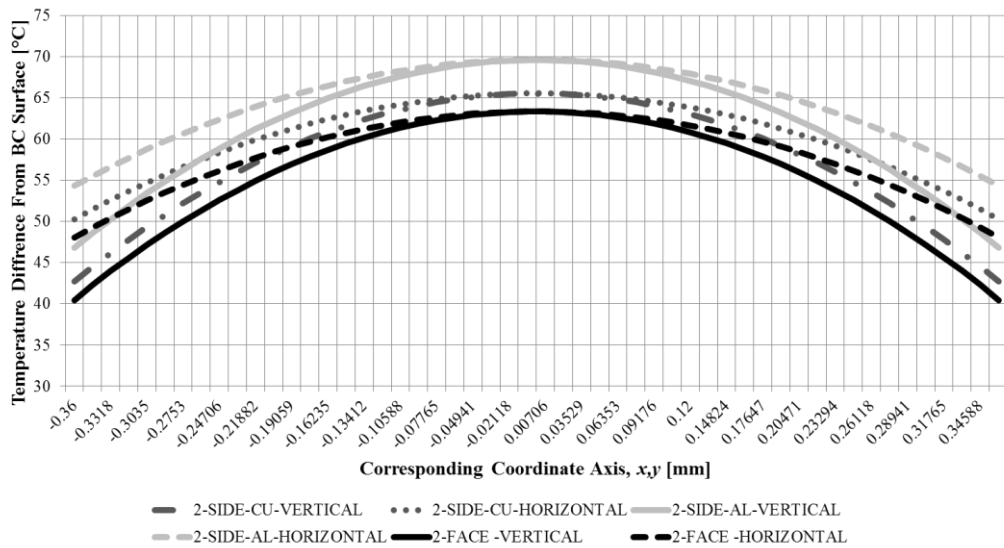


Figure 4.7 Comparison of the Middle Surface Temperature Profiles for 2-Side Cooled Crystal with Al and Cu Holders, and 2-Face Cooled Crystal

As expected, the copper crystal holder yields closer results to the face-cooling case due to its higher thermal conductivity than that of aluminum. When closely investigated, both aluminum and copper crystal holders only affect the temperature profiles by introducing a certain close-to-constant value temperature offset just as in the case with 1-side cooling. the mean values of the temperature profile differences between the crystal holder and crystal only cases, and the average deviations are tabulated in Table 4.2.

Table 4.2 The Mean Values of the Temperature Profile Differences Between 2-Side Contact Crystal Holder and Single Crystal with Average Deviations

Laser Slab Surface	Temperature Profile	Holder Material	Mean Value of the Temperature Difference (°C)	Average of Absolute Deviations (°C)	Ratio of Mean Values (Cu/Al)
End Surface Profile	Vertical	Cu	2.54	0.01777	0.34533
		Al	7.35	0.03090	
	Horizontal	Cu	2.53	0.00969	0.34599
		Al	7.30	0.01331	
Middle Surface Profile	Vertical	Cu	2.18	0.01128	0.34785
		Al	6.26	0.01741	
	Horizontal	Cu	2.17	0.00657	0.34843
		Al	6.24	0.00960	

While the average deviations can be considered as the same with those for the 1-side cooling, the mean values of the temperature differences for 2-side cooling are about half of the values for 1-side cooling given in Table 4.1. This is an expected result since the holders are geometrically identical to that in 1-side cooling, but for 2-side cooling the total heat discharged is split between the two holders. It can be concluded that since the thermal resistances due to holders are the same, two of the same resistances are in parallel, hence, the total resistance of the holder system decreases by half. Then, the temperature rise caused by introducing two holders is half of that for 1-side cooling.

The average deviation of the temperature profile differences between 2-face and 2-side cooling with copper and aluminum holders, calculated along the paths mentioned in Chapter 3, are 0.13°C and 0.36°C, respectively.. The method of modified constant temperature boundary condition to estimate the temperature profile of side-cooling by only simulating the face-cooling can also be applied in 2-side cooling case. The errors in this case have been calculated as 0.27%, and 0.68% for copper, and aluminum holders, respectively. Again, copper has lower

error compared to aluminum due to its superior thermal conductivity. For both cases, the errors are negligible just as the case with the 1-side cooling.

The OPD analysis on cooling with 2-side contact holder presented a similar trend as that of 1-side contact. As previously given in Table 3.2 the vertical and horizontal thermal lens radii for the 2-face cooling case were 1358 mm and 2028 mm, respectively. For the 2-side contact cooling case with copper holder the vertical and horizontal thermal lens radii have been calculated as 1369 mm and 2042 mm, respectively. The corresponding values for the aluminum holder are 1370 mm and 2037 mm. This is again due to the fact that the addition of the holder only increases the piston term in the OPD, and the thermal lens radius is independent of this term. Hence, the thermal lensing effect does not change with the addition of the holder.

#### **4.3.4-Side Contact Laser Crystal Holder Slab**

In this section, 4-face symmetrically and asymmetrically cooled crystals are investigated. For the same laser crystal slab, two conceptual holders have been constructed and analyzed. The 4-side contact laser crystal holder dimensions and the corresponding 4-face cooled crystal, previously analyzed are shown in Figure 4.8. For the asymmetrical 4-side cooling case, the boundary condition has been applied on one of the surfaces only.

The same mapping and same methods as in 1-side and 2-side contact cooling have been considered for this case. Only vertical temperature profiles for 4-side contact symmetric and asymmetric crystal cooling cases for aluminum alloy and copper alloy crystal holders as well as the 4-face cooling case are plotted in Figure 4.9 and Figure 4.10. Due to the symmetry of the case, vertical profiles are identical to the horizontal profiles for both symmetrical and asymmetrical cooling cases.

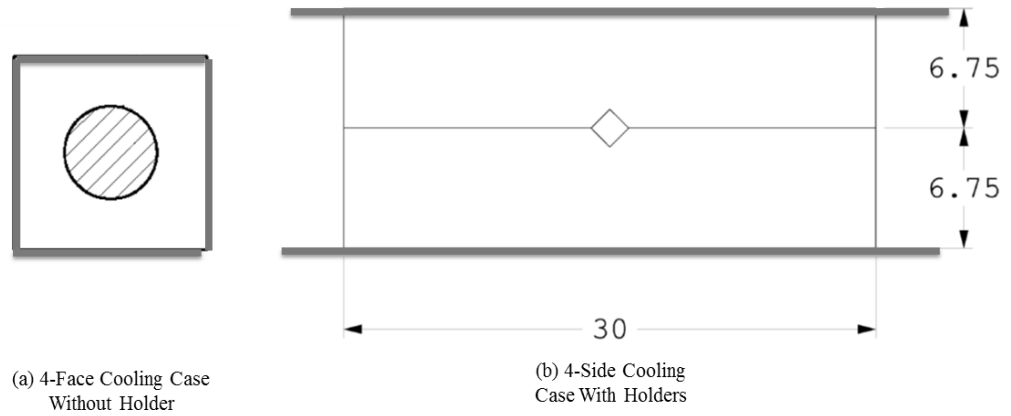


Figure 4.8 4-Face Cooling Geometry and the Corresponding 4-Side Symmetrical Cooling Geometry

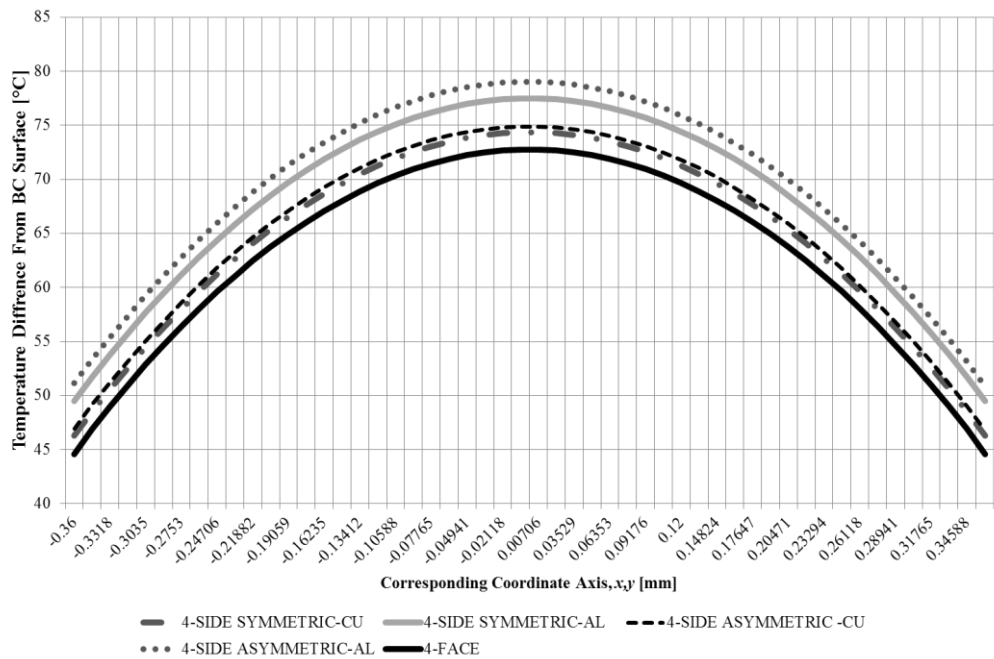


Figure 4.9 Comparison of the End Surface Temperature Profiles: 4-Side Cooled Crystal with Al and Cu Holders, 4-Face Cooled Crystal

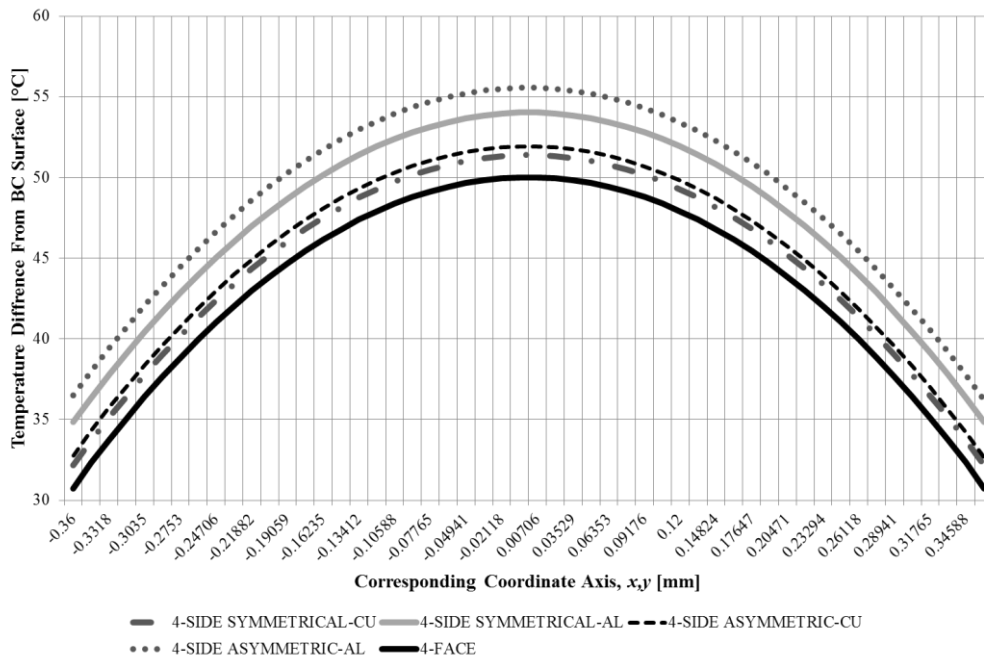


Figure 4.10 Comparison of the Middle Surface Temperature Profiles: 4-Side Cooled Crystal with Al and Cu Holders, 4-Face Cooled Crystal

Again, copper crystal holders yield closer results to the face-cooling case due to its higher thermal conductivity compared to aluminum. For the geometry of the conceptual 4-side contact crystal holders, the asymmetrically cooled copper holder outperformed the symmetrically cooled aluminum holder. When the results are closely investigated, both aluminum and copper crystal holders only affect the temperature profiles by introducing a close-to-constant temperature offset just as the case with 1-side and 2-side cooling for both symmetrical and asymmetrical cooling cases. The mean values of the temperature profile differences between the crystal holder and the single crystal case and the average deviations are tabulated in Table 4.3.

Table 4.3 The Mean Values of the Temperature Profile Differences Between 4-Side Contact Crystal Holder and Single Crystal with Average Deviations

Laser Slab Surface	Temperature Profile	Holder Material and Symmetry	Mean Value of Temperature Difference (°C)	Average of Absolute Deviations (°C)	Ratio of Mean Values (Cu/Al)
End Surface Profile	Vertical	Cu (S)	1.609	0.0135	0.3369
		Cu (A)	2.160	0.0295	
		Al(S)	4.774	0.0149	
		Al(A)	6.296	0.0664	
	Horizontal	Cu(S)	1.609	0.0134	0.3369
		Cu(A)	2.160	0.0294	
		Al(S)	4.774	0.0149	
		Al(A)	6.296	0.0663	
Middle Surface Profile	Vertical	Cu (S)	1.370	0.0089	0.3409
		Cu (A)	1.921	0.0269	
		Al(S)	4.018	0.0090	
		Al(A)	5.541	0.0647	
	Horizontal	Cu(S)	1.370	0.0089	0.3409
		Cu(A)	1.921	0.0268	
		Al(S)	4.018	0.0091	
		Al(A)	5.541	0.0647	

Considering the results for 1-side and 2-side cooling, the 4-side cooling yields the lowest maximum temperature, as well as the lowest temperature increase due to the introduction of the holder while average deviations remain the same. When the mean values of the temperature differences from Table 4.1 for 1-side cooling and Table 4.2 for 2-side cooling are investigated, it can be seen that the total conduction resistance caused by the 4-side cooling case holders is about 30% of that caused by 1-side cooling holder and about 65% of that caused by the 2-side cooling holder. Then it can be concluded that 4-side cooling is superior due to the lower resistances of its holder in addition to the superiorities of 4-face cooling presented in the previous section.

The other important factor not to be missed here is the symmetry consideration. Due to the introduction of both copper and aluminum holders, the asymmetric case only increased the temperature rise by 30% compared to the symmetric case. Since the increase is very low, the effect of the symmetry on the temperature increase in the crystal is also very low for the given geometry of the 4-side cooling crystal holders. The effects of the holder geometry on the temperature rise regarding the symmetry of the cooling are investigated in the following section.

The average deviation of the temperature profile differences between the 4-face cooling and 4-side cooling for copper and aluminum holders, calculated along the paths mentioned in Chapter 2, are  $0.09^{\circ}\text{C}$  and  $0.025^{\circ}\text{C}$ , respectively, independent of the symmetry. The method of modified constant temperature boundary condition to estimate the temperature profile of the side-cooling by only simulating the face-cooling can also be applied for 4-side cooling. The error in this case is calculated as 0.24% for copper holder and 0.63% for aluminum holder. The results are similar to those obtained for 1-side and 2-side cooling cases.

The OPD analysis on 4-side contact holder cooling yielded similar trends. In Table 3.2, the vertical and horizontal thermal lens radii for the 4-face cooling case were given as 1611 mm and 1610 mm. For the 4-side contact cooling case with copper holder, the vertical and horizontal thermal lens radii are both about 1622 mm for symmetric and asymmetric cooling. For aluminum holder, radii are also both 1622 mm for all symmetry cases considered. This is again due to the fact that the addition of the holder only increases the piston term in OPD and the thermal lens radius is independent of this term. Hence, the thermal lensing effect does not change with the addition of the holder.

The effects of the geometry and the material of the holder, the cooling orientation and conduction thermal resistance considerations for the 4-side contact cooling case are given in the following section.

#### 4.4. The Effects of the Holder Geometry and the Material on 4-Side Contact Cooling

From the analysis of crystal face cooling cases, it has been shown that the 4-face cooling is superior to 1-face and 2-face cooling both thermally and mechanically. The only downside of 4-face cooling compared to the 1-face and 2-face cooling cases is the increase in the horizontal thermal lensing effect. However, only this cooling form yielded equal thermal lensing radius in horizontal and vertical directions, which is beneficial in terms of the laser quality. In addition, the 4-side cooling, which is a more feasible cooling alternative of the 4-face cooling with the introduction of the crystal holder to the analysis, introduced the minimum thermal resistance into the system among all side cooling cases considered. In short, 4-side cooling yields the best thermal performance for crystal geometries with near-unity aspect ratio. This is not only because the crystal alone performs better when all 4 side surfaces are used to discharge heat, but also because the conceptual holder introduced for this case gives out the best thermal performance.

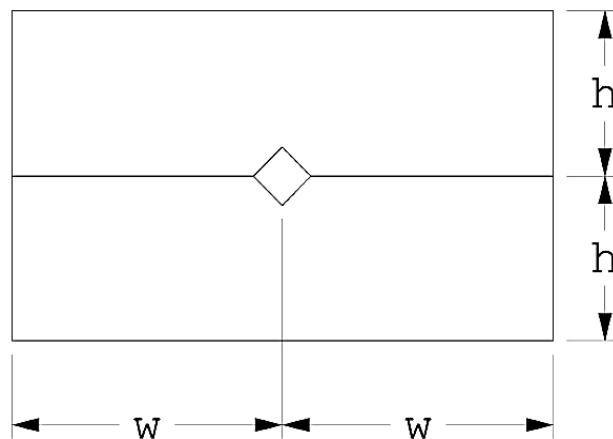


Figure 4.11 Dimensional Variables of 4-Side Contact Holder Used in the Analysis.

The geometrical effects of the holder have been considered for both symmetric and asymmetric cooling and for both aluminum and copper holders. Figure 4.11 describes the holder used in the analysis. Only the width of the crystal holder has been changed and the height,  $h$ , of the crystal has been taken as 10 mm. The analysis performed in the previous section used 4-side holders with the height of 7.25 mm. Here, the findings for holders of  $h = 10$  mm have been compared with those of  $h = 7.25$  mm holders. The thermal paths used for the present analysis are the same as those analyzed in the previous sections.

The average and the maximum temperatures of the thermal paths as a function of the half-width of the crystal are plotted in Figure 4.12 and Figure 4.13 for symmetric and asymmetric cooling orientation and for aluminum and copper holder materials.

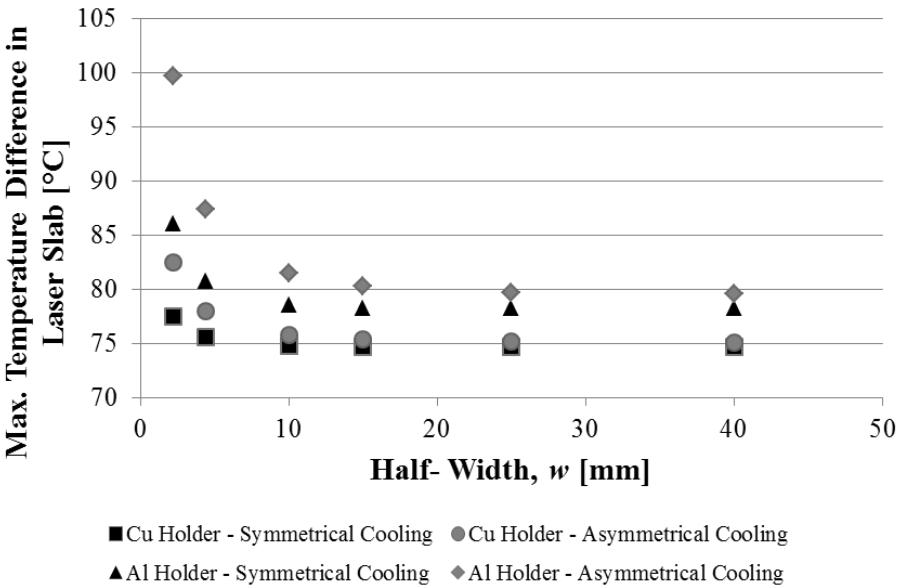


Figure 4.12 Variation of the Maximum Temperature Difference in the Laser Slab with the Half-Width for 4-Side Contact Holders

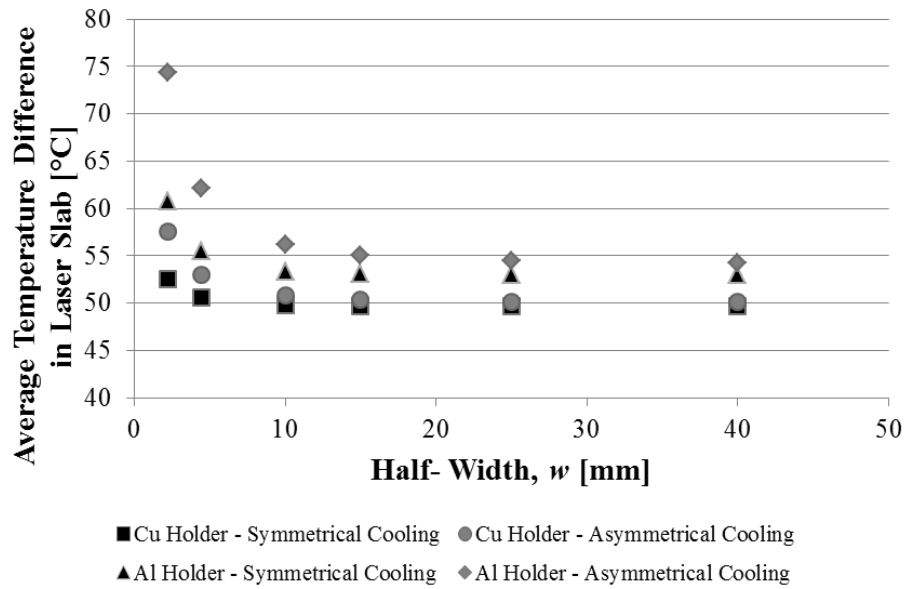


Figure 4.13 Variation of the Average Temperature Difference in the Laser Slab with the Half-Width for 4-Side Contact Holders

For  $w$  values greater than 10 mm, both maximum and average temperatures in laser crystal paths stabilize for the same holder and the cooling orientation. This means that the effect of  $w$  on conduction thermal resistance converges for both cooling cases. For the geometry of the laser crystal used in this analysis and for an  $h$  value enough to dissipate heat in the holder ( $h \geq 5 \times a$ ), the half width  $w$  selection should be a minimum of 10-15 mm.

The effect of cooling symmetry can be seen very clearly in  $w < 10$  mm region. The temperature rise with decreasing  $w$  is significantly higher for asymmetrical cooling. The temperature difference between the symmetrical and asymmetrical cooling at a given  $w$  is a constant and at its minimum in the region  $w > 10$  mm. The difference decreases as the thermal conductivity of the holder increases. For this case, it is  $0.5^\circ\text{C}$  for copper holder and  $1.3^\circ\text{C}$  for aluminum holder for  $w > 10$  mm, still a low value compared to the average temperature in the crystal. For  $w = 4.4$  mm the temperature difference between the symmetrical

and asymmetrical cooling is 2.4°C for copper holder and 6.7°C for aluminum holder. Asymmetric cooling yields close results to those for symmetric cooling for  $w > 10$  mm and can be favorable since it is easier to construct.

This critical half width value of  $w = 10$  mm can be also verified from conduction thermal resistance calculations. For symmetrical cooling with a single copper holder and using (4.1) with simulation result  $\Delta T = 1.89$  °C and half of the total heat load  $\dot{Q} = 10.5$  W, the conductive thermal resistance from the simulation data becomes;

$$R_{cond} = \frac{L_{ht}}{k \cdot A_{ht}} = \frac{\Delta T}{\dot{Q}} = \frac{1.89^\circ\text{C}}{10.5 \text{ W}} = 0.18^\circ\text{C/W} \quad (4.3)$$

Rather than the v-groove surface of the crystal holder, a flat surface of equal area to the two side surfaces of the crystal is assumed to be placed as shown in Figure 4.14, the modified distance between the heat discharging surface and the boundary condition applied surface becomes  $L_{ht} = 9.65$  mm. The thermal conductivity is  $k = 400$  W/(m · K) for copper holder. The effective heat transfer area then can be calculated from (4.1) as  $A_{ht} = 1.34 \cdot 10^4$  m<sup>2</sup>. Since the depth of the crystal holder is 12 mm the effective heat transfer width becomes 11.17 mm. When this effective heat transfer width is assumed to be the average of the laser crystal width and the effective width used for the boundary condition applied surface, the approximate width used by heat conduction on the boundary surface becomes 19.33 mm. The critical half-width was shown in Figure 4.12 and Figure 4.13 as  $w = 10$  mm, so the critical width becomes  $W = 2 \cdot w = 20$  mm  $\cong$  19.33 mm.

The same calculation can be performed for the previous analysis given in Section 4.3 while considering the fact that the critical half-width of the 4-side cooling crystal holder is independent of the holder material (thermal conductivity) and the cooling symmetry. The previous analysis used  $h = 6.75$  mm, applying the same procedure as above, the critical half width of this case has been found as  $w = 6.77$  mm. Since this effect is geometrical, a relation using the angle  $\alpha$

shown in Figure 4.14 can be used to approximate the critical holder width of the 4-side cooling case as

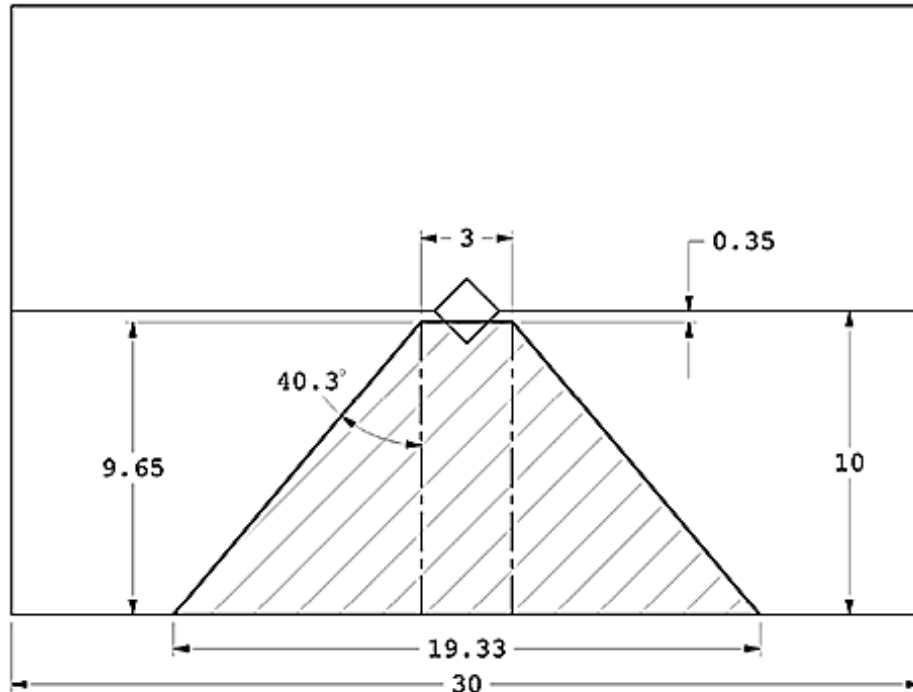


Figure 4.14 Heat Transfer Region in One of the 4-Side Contact Crystal Holder for the Symmetric Cooling Case

$$\cot \alpha = \frac{w - \frac{l}{\sqrt{2}}}{h - \frac{l}{3\sqrt{2}}} \quad (4.4)$$

and the angle  $\alpha$  has been found as  $40.3^\circ$ . It should be noted that this is just an approximation and may be subjected to certain dimensional constraints. It can only be used as a guidance to determine the minimum required width for the minimum conductive thermal resistance in the 4-side crystal holder design.



## CHAPTER 5

### DESIGN AND CONSTRUCTION OF THE EXPERIMENTAL SETUP AND THE MEASUREMENTS

The results of the analyses conducted in Chapters 3 and 4, favored 4-face and 4-side cooling designs over the other alternatives. The 4-face cooling yielded superior thermal properties over 1-face and 2-face cooling cases. Considering the 4-side contact cooling, introducing the 4-side contact holder had the minimum thermal resistance in addition to holding the benefits of 4-face cooling. For this reason, the experimental setup has been constructed to utilize the 4-side contact cooling.

#### 5.1. Design of the TEC Experimental Setup

In the design of the experimental setup, there are optical considerations in addition to the thermal constraints and thermal performance requirements. One of the limitations on the crystal cooling design with TEC is the distance between the optical path axis, and the boundary condition applied surface. The optical path axis is concentric with the center axis of the laser crystal slab, and the boundary condition applied area is the TEC contact surface with the crystal holder. The distance between the two is limited to a minimum value of 27 mm due to the architecture of the laser cavity and the dimensions of the optics and optical holders used in the cavity. The objective of the cavity design, illustrated in Figure 5.1, is to minimize the optical path. As the laser system should operate at harsh temperature ranges, such as  $-40^{\circ}\text{C}$  to  $+60^{\circ}\text{C}$ , the usage of a TEC with

relatively large dimensions compared to the dimensions of the laser cavity is required.

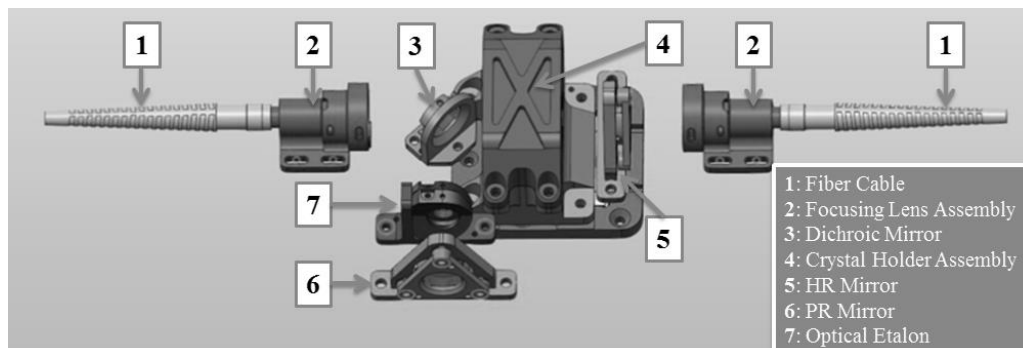


Figure 5.1 The Cavity Design of the Double-End-Pumped Tm:YLF System

The asymmetric cooling for the TEC application has been selected for its benefit of requiring only one heat sink. On the other hand, the symmetric case requires two heat sinks that are parallel to each other which affects the device architecture significantly. The selection of TEC is also due to convenience related reasons, such as reliability, design simplicity and compactness compared to other alternatives of active cooling for the temperature range specified above.

One of the early stage design problems was the assembly of the laser slab inside the holder. The limitations forced the holder to be much bulkier when compared to the very small laser crystal. The assembly of a small laser crystal directly into a large holder may result in either not enough or too much pressure on the thermal interface material used between the laser crystal slab and the laser crystal holder. The former causes low thermal contact because of the assembly bolts being too far away from the crystal to hold the crystal holder assembly together. On the other hand, the latter leads to fracture of the laser crystal slab due to unwanted internal stresses generated by overusing of the assembly bolts for both holding the assembly, and fine-tuning the pressure on the thermal pads placed on the crystal.

To overcome the mentioned problems, two stage crystal holders showed in Figure 5.2 have been used. The heat flux values in the first stage are far greater than those of the second stage, and the superior thermal conductivity of copper is benefitted mostly in close proximity of the laser crystal slab. Due to the weight concern, only the first stage crystal holders are made of copper. The first crystal holders with the crystal are then assembled to the second stage crystal holders where the heat flux values are significantly less. The second stage holders are made of relatively lightweight aluminum alloy. The design involves symmetric cooling with two TEC modules as shown in Figure 5.2. Asymmetric cooling can also be employed with the same setup by bypassing one of the TEC modules.

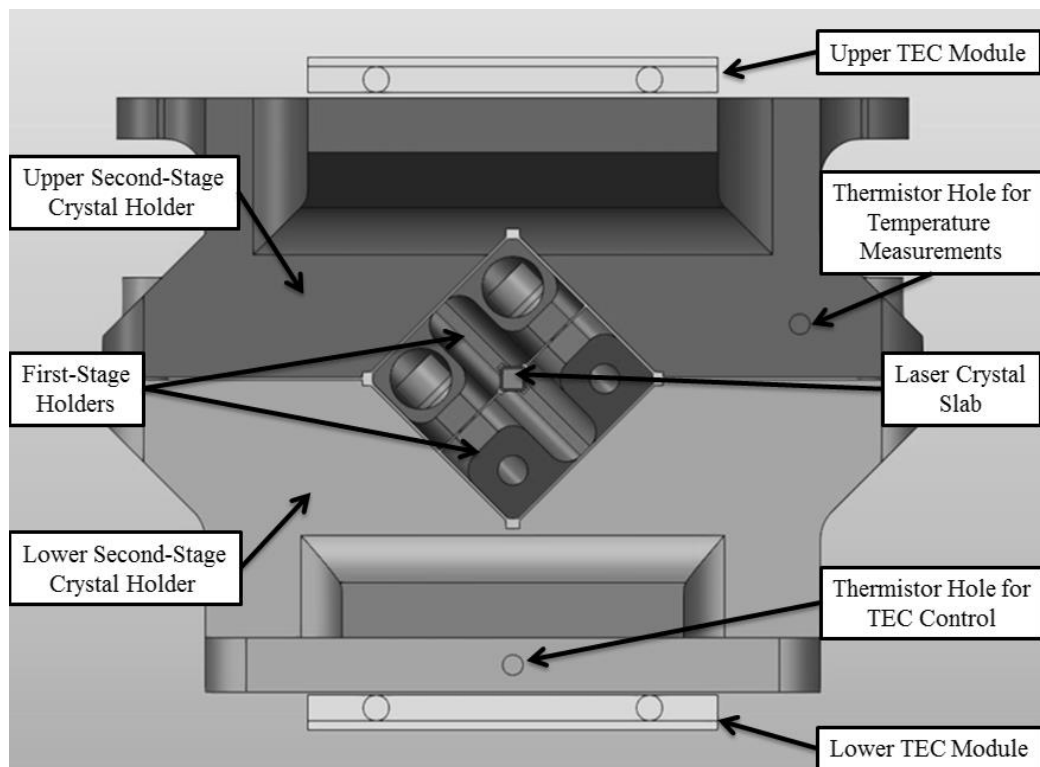


Figure 5.2 Experimental Laser Crystal Holder Design for the Thermoelectric Cooling

Another design concern in the experimental setup was the selection of thermal interface materials (TIMs) between the laser crystal slab and the first holder, and between the first and the second laser crystal slab holders. The TIM selection for the interface between the laser crystal slab and the first copper laser crystal holders should have the following properties in addition to low thermal resistance and low outgassing property which is required for use in laser devices. TIM material must be optic friendly, as assembling and disassembling with laser slab should be easy and should leave no contaminants on the surfaces. For this case, INDIUM Corporation's soft metal alloy TIMs have been selected. Since their composition is made out of soft metal alloy, they are easy to wrap around the laser crystal slab and can easily be disassembled from it. They leave no trace or contaminants from the crystal surface when disassembled or when it is assembled. Standard TIMs have been used to wrap the laser crystal, and heat-spring TIMs have been used on the interface between the two first stage laser crystal holders. Heat-spring TIMs offer better thermal impedance values for smaller applied pressure values and more reusability. INDIUM TIMs have downsides such as the cost and the high pressure dependence of their thermal resistance ( $0.12 \text{ cm}^2 \cdot ^\circ\text{C}/\text{W}$  at 70 psi and  $0.07 \text{ cm}^2 \cdot ^\circ\text{C}/\text{W}$  at 130 psi). An irregular pressure distribution on INDIUM TIM can cause very irregular thermal interface resistance distribution. INDIUM TIM has been selected mostly for its very low thermal resistance which is crucial in laser and holder contact due to very high heat fluxes, and its ease of assembly. For the interface between the first and the second crystal holders and between both holders of second stage, LAIRD Corporation's T-Pli 210 TIM has been selected, since it has good thermal resistance which is mostly independent of the pressure applied onto it after a certain low pressure value ( $0.09 \text{ cm}^2 \cdot ^\circ\text{C}/\text{W}$  at 70 psi and  $0.09 \text{ cm}^2 \cdot ^\circ\text{C}/\text{W}$  at 130 psi). Besides, it is cost-effective when compared to INDIUM TIMs.

A numerical analysis of the TEC system has been conducted using the same mesh system on the crystal and applying contact thermal resistances. As the boundary condition, the TEC surface is approximated to be at  $0^\circ\text{C}$  constant

temperature just as in the previous cases. The temperature profile results of the end surface are plotted in Figure 5.3. Even though, the distance between optical path and cooling surface was larger than that of conceptual cases, TEC experimental setup outperformed aluminum conceptual design in the simulation presented in Figure 5.3. This is mainly due to the fact that maximum heat flux in the holder occurs at the close proximity of the laser slab and the TEC experimental setup utilizes copper first-stage holders.

A brief transient analysis on this case has been performed as well, to have an idea about the transient behavior of the system. Again a constant temperature boundary condition has been applied which represents a very ideal TEC and TEC controller. The system achieved thermal equilibrium in about 2 seconds, which was very close to the time in the crystal only analysis, due to the fact that the holders act as great heat capacitances.

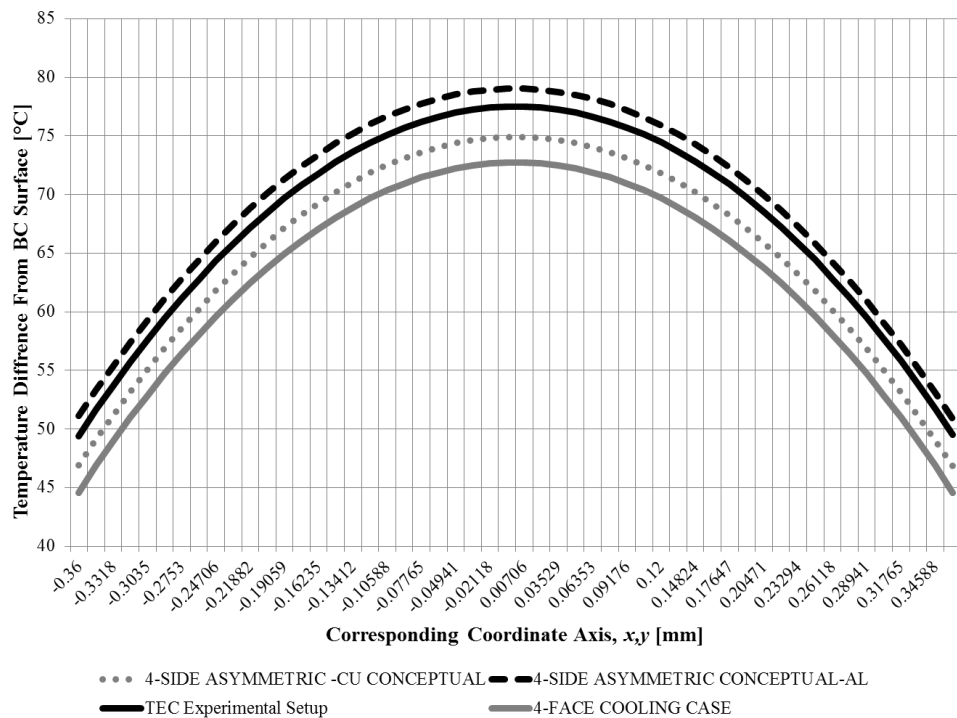


Figure 5.3 Comparison of the Numerical and Experimental Results for the End Surface Temperature Profiles: 4-Side Asymmetrically Cooled Crystal with Al and Cu Holders, 4-Face Cooled Crystal

## 5.2. Design of the Water-Cooled Experimental Setup

A symmetrical water cooled system has been designed to compare the results with the TEC system. The system resembles the TEC cooled setup and may be seen in Figure 5.4. Fluid channels have been placed in the second stage aluminum holders to cool the laser indirectly by cooling the first stage crystal holder.

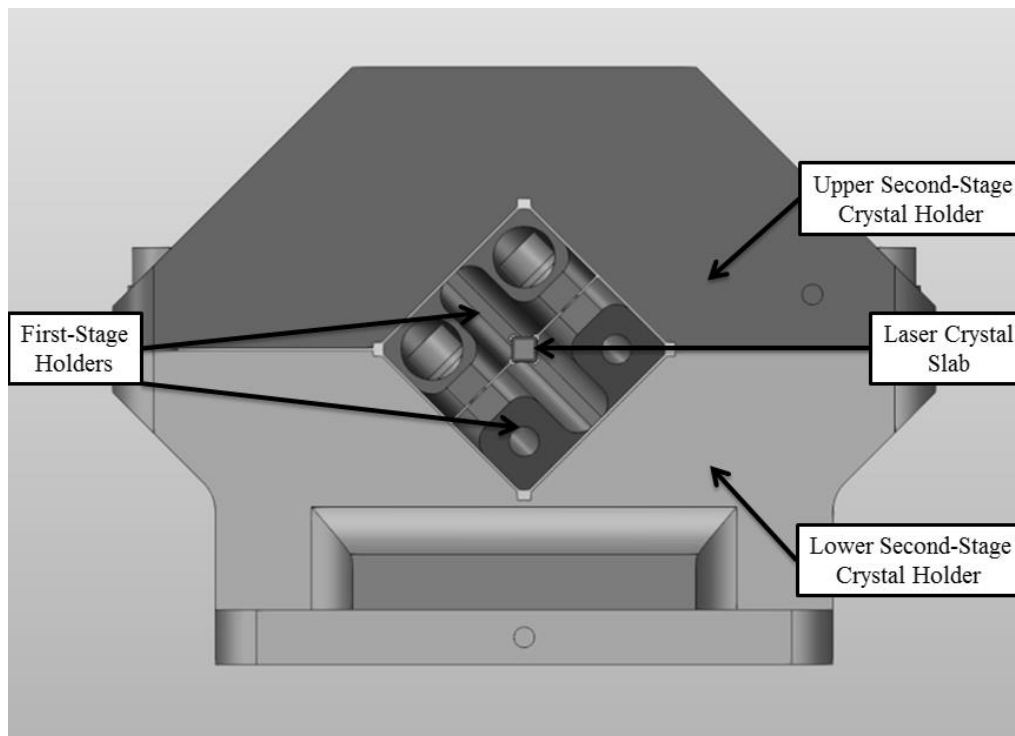


Figure 5.4 Experimental Laser Crystal Holder Design for Water Cooling

The flow of water in the cooling channels in the holder assembly is shown in Figure 5.5. Uniform water cooling has been aimed in the design, and both the inlet and the outlet have been placed at the upper surface of the holder, so that the piping of the cooling system does not interfere with the optical path and other optical components.

To obtain symmetric water cooling, the temperature difference between the inlet and the outlet of the system is required to be less than 0.5°C i.e.  $\Delta T \leq 0.5^\circ\text{C}$ . The required fluid flow for this temperature difference can be calculated using a simplified steady flow energy balance as

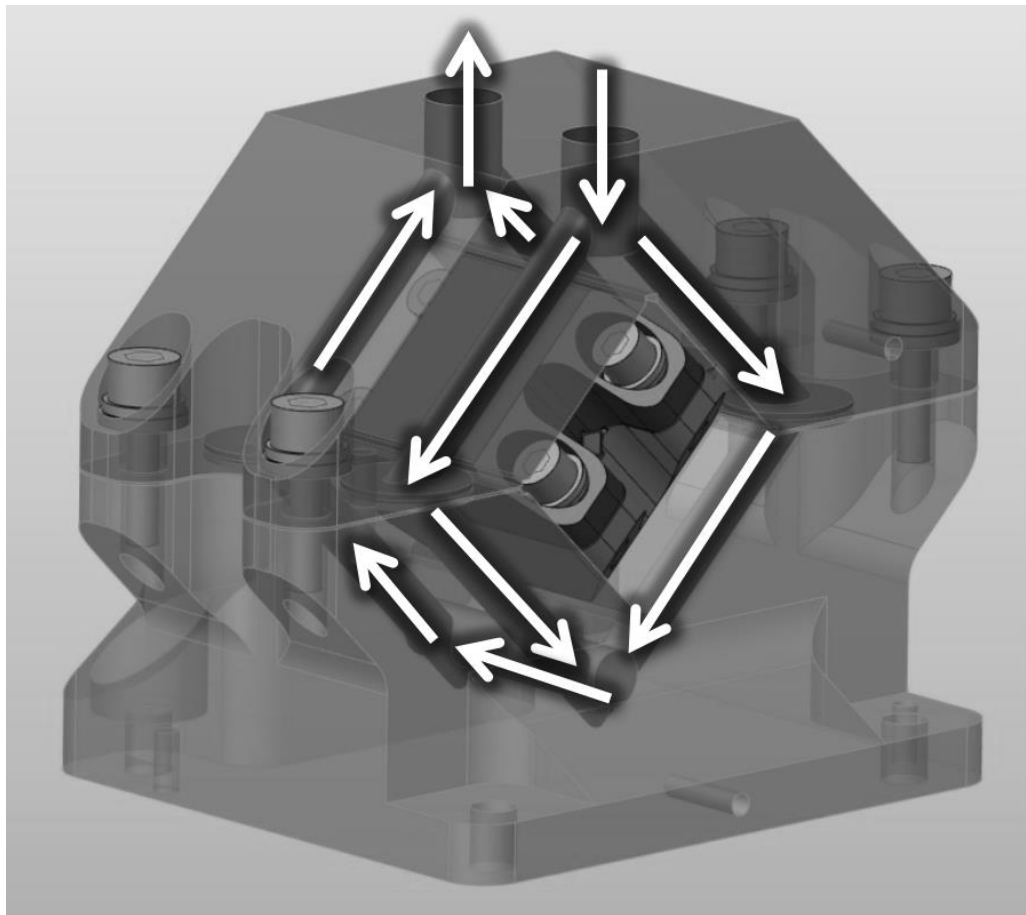


Figure 5.5 Crystal Holders for the Water Cooling Setup and the Path of the Cooling Water

$$\dot{q} = \dot{m}c_p(T_{out} - T_{in}) = \rho\dot{V}c_p\Delta T \quad (5.1)$$

where  $\dot{q}$  is the heat discharged to the fluid,  $\dot{m}$  and  $\dot{V}$  are the fluid mass flow rate and the volumetric flow rate,  $c_p$  is specific heat of the fluid at constant pressure

and  $\Delta T$  is the temperature difference of the flow outlet and inlet. Using (5.1), the required water flow rate has been found as

$$\begin{aligned}\dot{V} &= \frac{\dot{q}}{\rho c_p \Delta T} = \frac{20.1 \text{ W}}{\left(\frac{10^3 \text{ kg}}{\text{m}^3}\right) \cdot \left(4.185 \frac{10^3 \text{ J}}{\text{kg} \cdot ^\circ\text{C}}\right) \cdot (0.5^\circ\text{C})} \\ &= 9.56 \cdot 10^{-6} \text{ m}^3/\text{s} = 0.58 \text{ L/min}\end{aligned}\quad (5.2)$$

Then, the volumetric flow rates higher than 0.58 L/min will yield temperature differences less than 0.5°C. For this setup  $\dot{V} = 1 \text{ L/min}$  has been selected which results in a temperature difference of 0.3°C.

The water flow channels inside the holder are circular with a diameter of  $D = 3 \text{ mm}$ . The average speed of the flow have been calculated as

$$\bar{v} = \frac{\dot{V}}{\pi D^2/4} = \frac{1.667 \cdot 10^{-5} \text{ m}^3/\text{s}}{7.068 \text{ m}^2} = 2.358 \text{ m/s}\quad (5.3)$$

Water at 15°C, which is the experimental cooling temperature of the system, has a dynamic viscosity of  $\mu = 0.00114 \text{ Pa} \cdot \text{s}$  and a Prandtl Number of  $Pr = 8.2$ . The Reynolds number for the flow have been evaluated as

$$\overline{Re}_D = \frac{\rho \bar{v} D}{\mu} = \frac{\frac{10^3 \text{ kg}}{\text{m}^3} \cdot 2.358 \frac{\text{m}}{\text{s}} \cdot 3 \cdot 10^{-3} \text{ m}}{0.00114 \text{ Pa} \cdot \text{s}} \cong 6200\quad (5.4)$$

Since  $Re_D > 2300$ , the flow is not laminar. Assuming a surface roughness of  $k_s = 1 \mu\text{m}$  and a relative roughness of  $k_s/D = 3.33 \cdot 10^{-4}$ . From the Moody chart, [56, 57], with  $k_s/D$  and  $Re_D$  values, the friction factor has been found as  $f = 0.01$ .

As a rough estimate, using the relation proposed by Dittus and Boelter [58], the Nusselt Number,  $Nu_D$  has been calculated as

$$\overline{Nu}_D = \frac{\bar{h} D}{k} = 0.023 \cdot \overline{Re}_D^{0.8} \cdot Pr^{0.4} = 0.023 \cdot 6200^{0.8} \cdot 8.2^{0.4} = 57.74\quad (5.5)$$

Then the average convective heat transfer coefficient has been calculated as

$$\bar{h} = \frac{\overline{Nu} \cdot k}{D} = 11547 \text{ W/m}^2 \cdot \text{K} \quad (5.6)$$

This is a relatively large convection coefficient for single-phase flow, and is due to tiny cooling channels and high average flow velocities.

When Gnielinski [59] relation is used, the average Nusselt number is evaluated as  $\overline{Nu}_D = 56.85$ , which is very close to that obtained using the Dittus and Boelter [58] relation.

For the finite element analysis  $\bar{h} = 11547 \text{ W/m}^2 \cdot \text{K}$  has been used on the channel surfaces with a fluid temperature of 0°C for the ease of comparison with the TEC experimental setup and the previous conceptual holders. The objective here is to determine only the difference between the crystal temperature and the temperature listed as the boundary condition.

The end surface temperature profile for the water cooled experimental setup is given in Figure 5.6 along with the profile for the TEC experimental setup and the 4-face cooling case.

From the simulations, it can be observed that both TEC and water cooled experimental systems provide very close results. Water cooling yielded slightly lower temperatures mainly due to the fact that the cooling channels are closer to the laser crystal than the TEC surface.

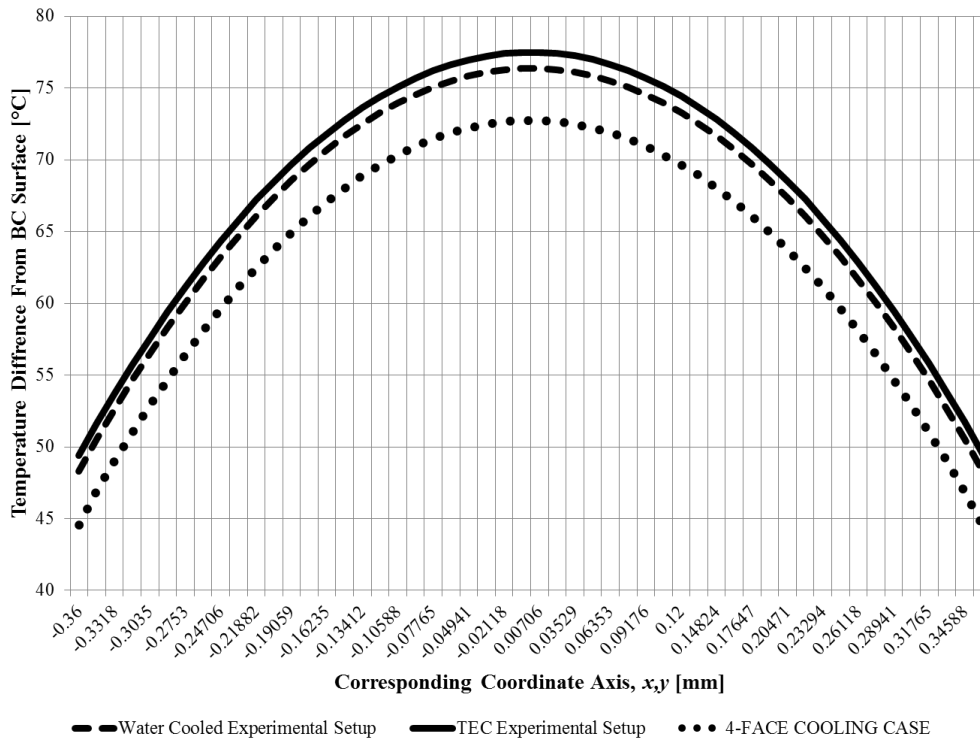


Figure 5.6 Comparison of the Numerically Obtained End Surface Temperature Profiles for the Water Cooled and Thermoelectrically Cooled Experimental Setups with 4-Face Cooling

### 5.3. Assembly and the Components of the TEC Experimental System

The assembly of the laser crystal holder has been conducted on a bench where a HEPA filter system continuously pumps clean dust- and particle-free air. The components for the assembly are given in Figure 5.7.

All the mechanical components used in the assembly have been cleaned from the debris, dust and organic contaminants by a supersonic cleaner system. Deionized water and industrial detergent have been used in the cleaning of the mechanical components of the assembly.

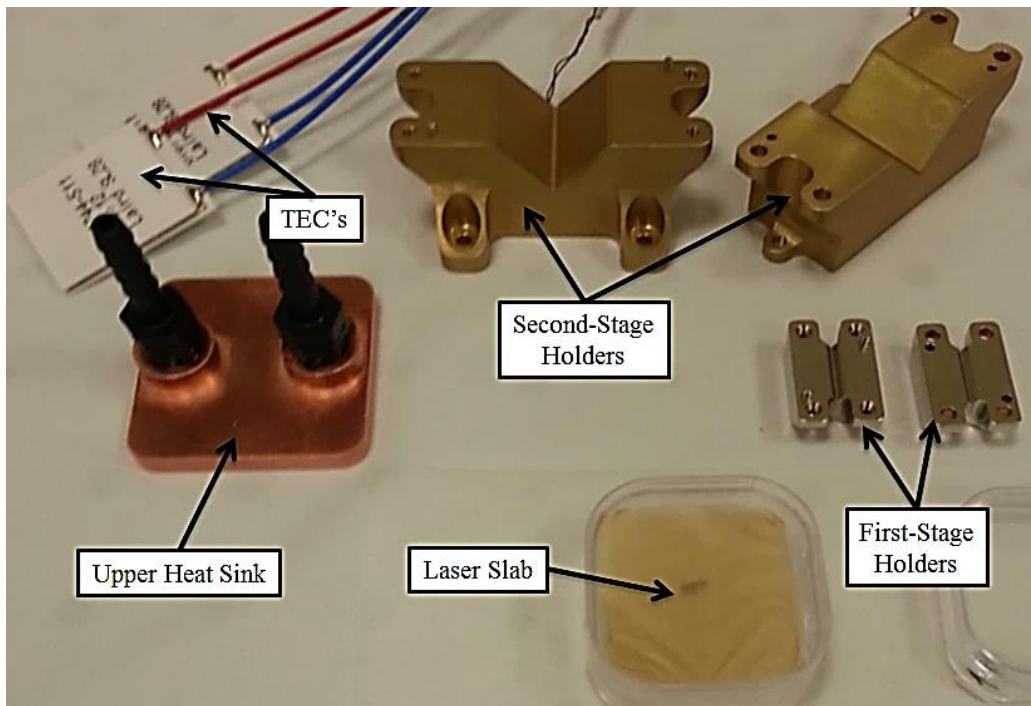


Figure 5.7 The Components of the Laser Crystal Holder Assembly for Thermoelectric Cooling Setup

The first step in the assembly was to wrap the indium TIM around the laser crystal. The handling of the laser crystal is very important since the end-surfaces of the slab should be free of contaminants and the optical coating should not be damaged while assembling. Tweezers with soft tips have been used in handling the crystal and absolutely no contact has been made with the end-surfaces. Figure 5.8 shows the laser crystal slab wrapped in indium TIM.

The crystal has then been mounted on one of the first-stage holders paying attention to the marking on the side-surface of the slab that indicated the polarization axis. The second first-stage holder has been assembled by two guide pins and four assembly bolts. A torque-wrench has been used for the tightening of the bolts, to obtain uniform pressure distribution on the crystal and to prevent over-tightening of the bolts which may yield undesired stresses on the laser

crystal. Indium heat-spring TIMs have been used on the interface between the two first-stage holders. The first-stage holder assembly is given in Figure 5.9.

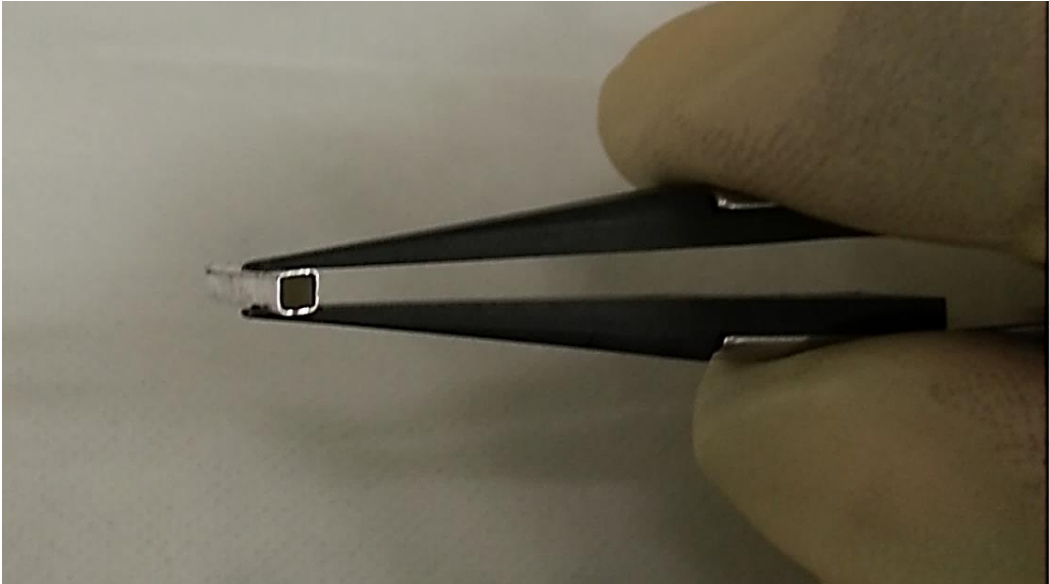


Figure 5.8 Tm:YLF Laser Crystal Slab Wrapped in Indium TIM



Figure 5.9 The Assembly of the First-Stage Holders

The first-stage holder assembly has then be mounted on the second-stage holders and Tpli-210 TIM of Laird Company has been used in this assembly process. Two thermistors have been glued on each of the second-stage holders by using a thermally conductive bonding agent. These thermistors have been used as the feedback mechanism of the TEC controller. The final assembly of the crystal holders without the mounting of the TECs is shown in Figure 5.10.

The crystal holder assembly has been mounted on the base system which also acts as the heat sink of the TEC mounted at the bottom side of the crystal holder assembly. The Tm:YLF experimental system may be seen in Figure 5.11.

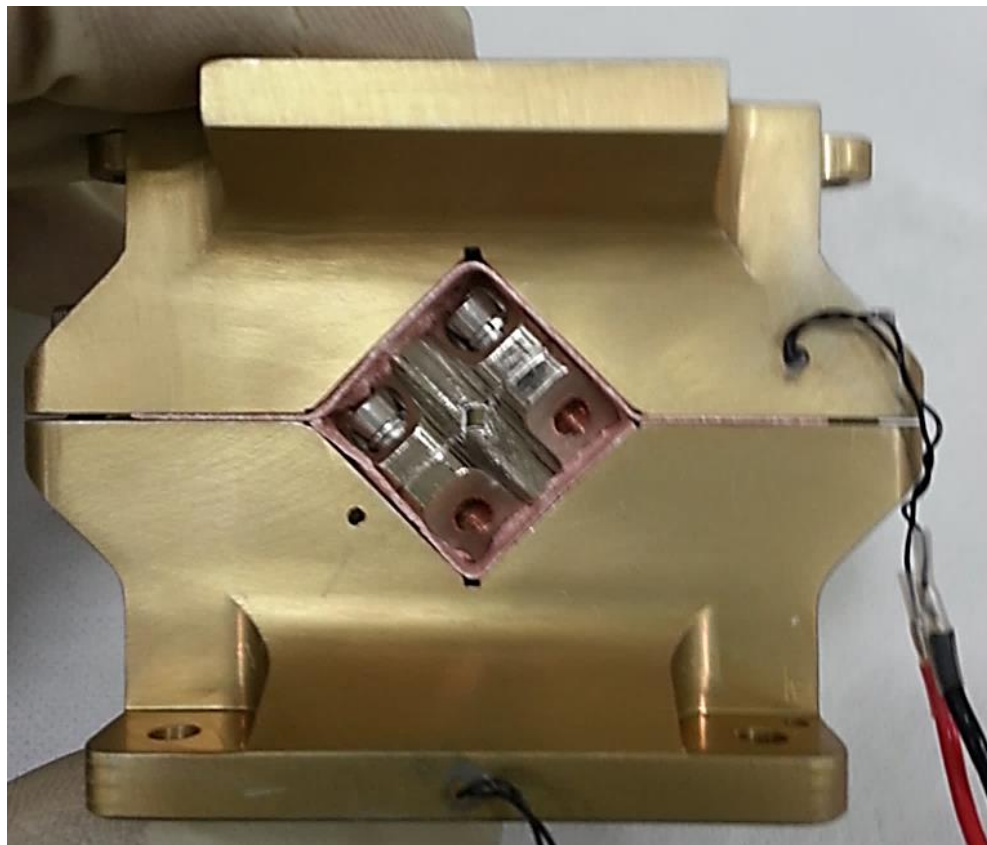


Figure 5.10 The Assembled Crystal Holders

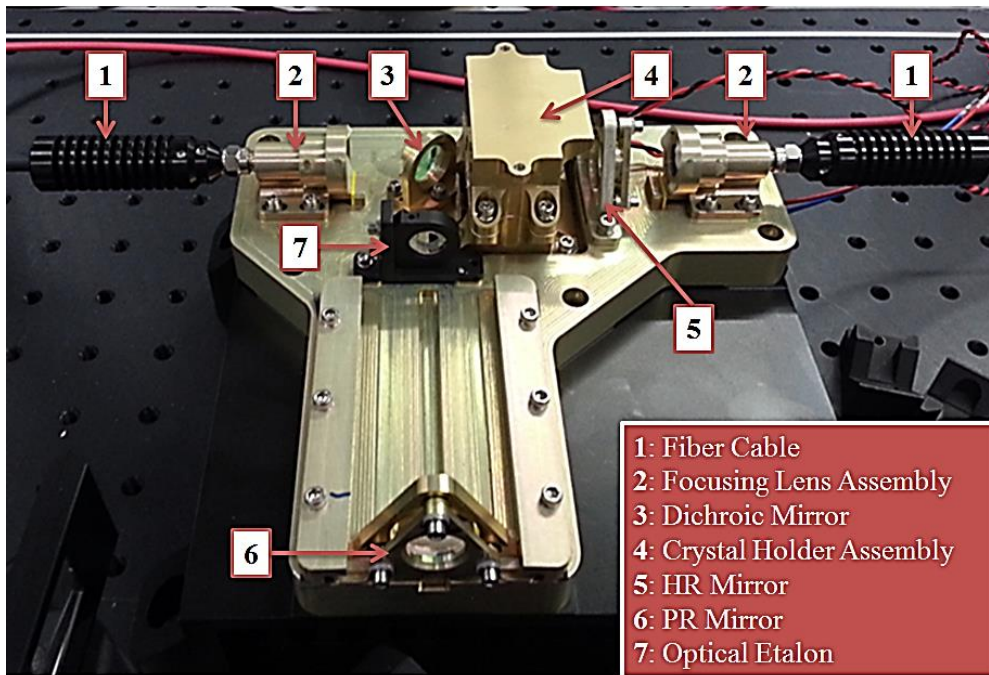


Figure 5.11 Experimental Setup for the Asymmetrical Thermoelectric Cooling System

For symmetrical cooling, an identical TEC has been mounted between the upper cooling surface of the holder assembly and a mini-channel heat sink manufactured by Curamik Electronics GmbH. This heat sink has been placed in closed-loop with a pump and a fluid-to-air heat exchanger assembly. The experimental setup with symmetrical TEC system is shown in Figure 5.12.

The diodes by DILAS GmbH used to pump the Tm:YLF system have been mounted on a cold plate which is cooled by a Neslab ThermoFlex900 chiller. The precise temperature control has been satisfied by TECs. A precise temperature control on the diodes was required since variations in diode operation temperatures result in shifts in the pump wavelength, hence, decreased output power of the laser. The diodes mounted on the cold plate are shown in Figure 5.13.

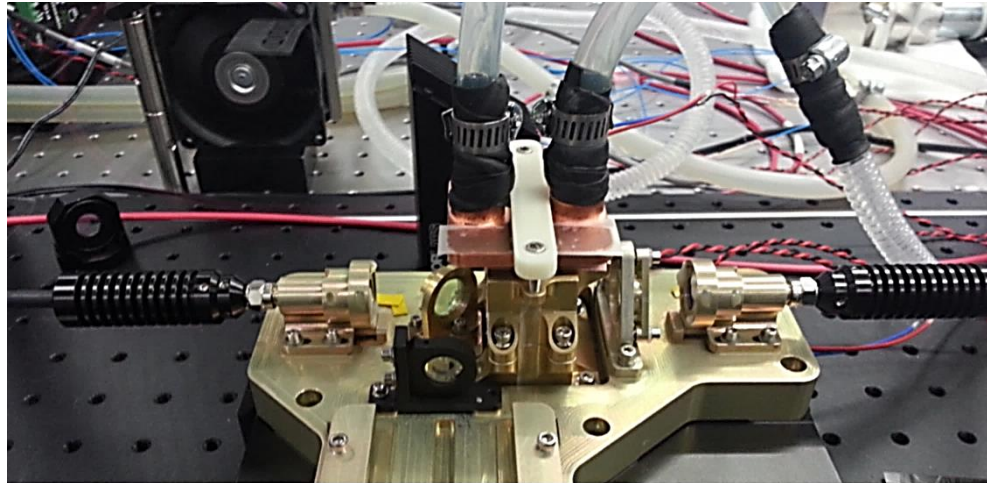


Figure 5.12 Experimental Setup for the Symmetrical Thermoelectrically Cooled System

All the TECs used in the experiments have been controlled using PTC 10 K-CH Temperature Controllers manufactured by Wavelength Electronics. These control modules have been powered by external power supplies according to the maximum operational current and voltage requirements of the TECs. Due to the high absorptivity of water vapor around  $2\ \mu\text{m}$  spectrum, the Tm:YLF cavity has been enclosed in a Plexiglas casing and was purged continuously by dry air of  $-50^\circ\text{C}$  dew point.

A FLIR T335 Thermal Imaging Camera has been used for surface temperature measurements. Since the metallic surfaces in this experiment are reflective in the infrared region, the infrared emission from the surroundings affected the readings. To overcome this problem, Scotch® 810 Magic™ Tapes were used on the surfaces. They provided no significant reflectivity and due to their matte finish yielded good temperature readings. The emissivity of these tapes has been calculated as about 0.80 by placing them on a temperature controlled surface at  $15^\circ\text{C}$ , and iterating the emissivity value setting of the camera till it measured the same value as the thermistor on the control surface.

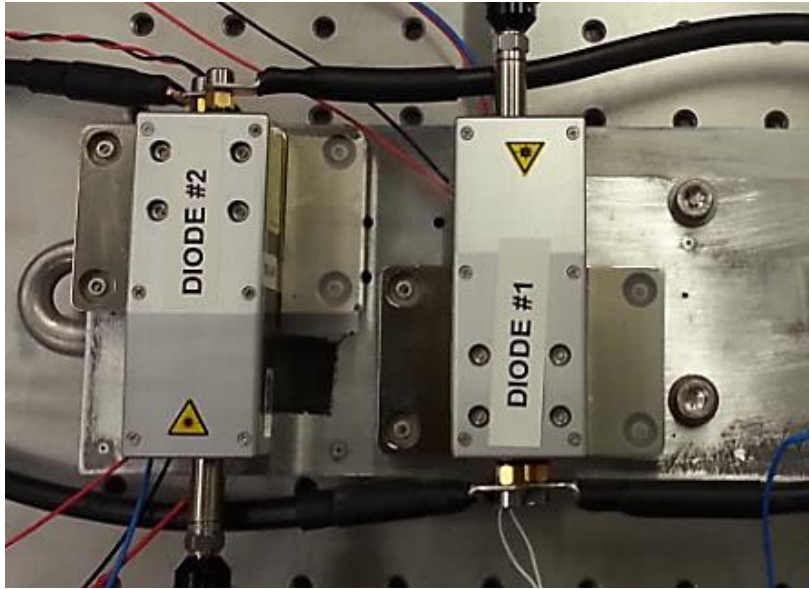


Figure 5.13 793 nm Pump Diodes

Another problem encountered for the temperature measurements by the thermal imaging camera was that the Plexiglas is opaque in the infrared region, meaning that temperature reading through Plexiglas casing was impossible. So the camera has been aligned as shown in Figure 5.14 through the opening marked by a double-sided arrow on the casing.

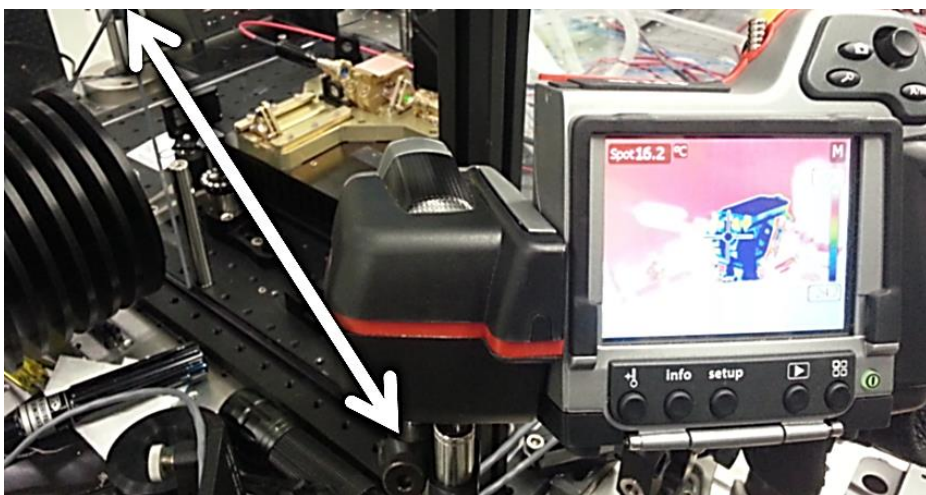


Figure 5.14 Thermal Imaging Camera and the Experimental Setup

The output power of the laser has been measured using Powemax PM150 and Fieldmax II Laser Power/Energy Meters produced by Coherent Lasers. The laser beam profiles have been measured by using NanoScan2 by Ophir Photonics.

## **5.4. Experimental Results from the TEC Setup**

### **5.4.1. Experimental Data**

Using the experimental system explained in detail in the previous section, the operational temperature readings of the mini-channel heat sink, the upper and lower second stage holders, the bottom heat sink, the output power of the laser and the currents used by the TECs have been obtained for both symmetrical and asymmetrical cooling cases with increasing diode supply current. The experimental readings taken from the setup are presented in Tables 5.1 and 5.2.

The data have been obtained by adjusting the electrical current supplied to the pumping diodes. First, the temperature readings have been taken from the system when there was no heat load on the laser crystal (zero supplied current to the pumping diodes) and the TECs were operational. The TEC controllers have been adjusted so that the temperature feedback from the thermistors on the assembly yielded 15°C.

The lasing occurred when the supply current of the diode was about 15 A. For supply currents up to 15 A, leaked pumping powers of about 1 to 20 mW could be observed by the laser power energy meter. At 15 A supply current, the lasing initiated and the power reading jumped to reasonable values. Thus, other than the zero supply current, the experimental data have been recorded starting from 15 A supply current.

Table 5.1 Measurements from the Symmetrically Cooled TEC Setup

<b>Diode Supply Current (A)</b>	0	15	20	25	30	35	40	45
<b>Temperature of Second-Stage Holder, Upper (°C)</b>	15.5	15.3	15.5	15.8	16.1	16.1	17.2	17.7
<b>Temperature of Second-Stage Holder, Lower (°C)</b>	15.3	15.5	15.6	15.7	15.8	16.1	16.5	16.6
<b>Temperature of Mini-Channel Heat Sink (°C)</b>	28.1	28.6	29.1	29.5	30.3	30.6	33.6	35.7
<b>Temperature of Bottom Heat Sink (°C)</b>	27.6	27.8	28	28	28.2	28.6	29.4	30.4
<b>Laser Output Power (W)</b>	0	1.51	4.31	7.12	9.99	13.08	15.6	16.8
<b>TEC Current, Upper (A)</b>	0.6	1.3	1.7	2	1.9	1.2	0.8	1
<b>TEC Current, Lower (A)</b>	0.6	0.8	0.95	1.08	1.22	1.36	1.6	2

Table 5.2 Measurements from the Asymmetrically Cooled TEC Setup

<b>Diode Supply Current (A)</b>	0	15	20	25	30
<b>Temperature of Second-Stage Holder, Upper (°C)</b>	15.8	17	17.9	18.6	20.6
<b>Temperature of Second-Stage Holder, Upper, Obtained from Thermistor (°C)</b>	15.7	16.8	17.5	18.3	20.0
<b>Temperature of Second-Stage Holder, Lower (°C)</b>	15.6	16.8	17.0	17.2	17.9
<b>Temperature of Bottom Heat Sink (°C)</b>	29	29.3	30	30.7	34.8
<b>Laser Output Power (W)</b>	0	1.47	4.2	6.92	9.64
<b>TEC Current, Lower (A)</b>	0.8	1.7	2.23	2.92	5

At each measuring step, enough settling time has been given so that system could attain thermal equilibrium. In thermal equilibrium, the temperature data of the second-stage holders and the heat sinks have been noted. In addition to the temperature data, supply currents to TECs, as well as the output laser power have been recorded.

The first important point observed from the experiments is that there exists a temperature offset of the crystal holders from the set value of 15°C especially for higher pumping powers for both cooling cases. This is mainly due to the fact that the thermistor of the feedback mechanism being located in close proximity of the first-stage holders, close to the laser crystal slab. On the other hand, the temperature readings have been taken from the outer surfaces of the second-stage holders due to the laser and pump beam interference in close proximity of the laser slab. There exists a thermal resistance between the temperature controlled zone by the TEC and the temperature measured zone which causes increased temperature difference from the set temperature with increased heat load (i.e. increased pumping power). This effect was more crucial for asymmetric cooling case due to higher thermal resistance for that case.

As may be observed from Table 5.2, a maximum of 30 A diode supply current has been measured since the system attained the 5 A current supply limit in asymmetrical cooling. The main reason for the diode supply current limitation is the lack of forced convection at the bottom heat sink. The function of the Tm:YLF system is to pump a Ho:YAG system, and the optical path of the Tm:YLF and Ho:YAG systems had to be at the same level. For this reason, a fan could not be assembled below the heat sink as intended. The lack of forced convection yielded higher temperature differences between the cold and the hot sides of the TEC which in return reduced the operational efficiency of the TEC.

Although the lower heat sink was not supported by a fan to initiate forced convection, for the symmetrical cooling system, the measured heat sink

temperatures are found to be in a reasonable range since a sufficient heat exchanger and fan support has been supplied to the upper mini-channel heat sink.

During the experiments, it has been observed that the upper TEC underperforms while letting the lower TEC overperform to compensate, even though both TECs' controllers and the feedback mechanisms were identical. This was mainly due to the difference in the heat sink types and the slow reaction time of the PI controller used in the TEC. In some cases, it has been observed that the upper TEC was switched to heat harvester mode, while the lower TEC took over the whole heat load, leading to an unbalanced cooling system. At higher pumping powers, current supplied to the upper TEC has been observed to oscillate for this reason. A better designed TEC controller may overcome this problem.

Considering the laser output levels, since the system was not fully optimized optically, the results yielded relatively low slope efficiency, which is a close-to-linear curve obtained by plotting laser output versus the pump power. As expected, symmetric cooling yielded slightly better output powers due to low average holder and crystal temperatures which confirms the numerical results.

In the asymmetrical cooling, the temperature data obtained from the thermal imaging camera has been compared and validated with the thermistor data of the second TEC control system. The obtained thermistor resistance data was converted to temperature by using the temperature-electrical resistance relation supplied by the manufacturer. It has been observed that the thermistor data is in good agreement with the temperature data obtained from the thermal imaging camera.

#### **5.4.2. Experimental Heat Load Determination**

At steady-state, the heat discharged by the TEC is equal to the addition of the heat load on the laser slab, the unwanted heat inputs to the system due to natural convection and radiation on the outer surfaces of the assembly, and the heat inputs from the mounted isolator plate. The heat inputs to the system due to natural convection have been simulated to be less than 0.5 W. The experimentally calculated heat discharged by the TEC, and the numerically estimated heat load on the slab are expected to be equal differing only by a constant offset due to unwanted heat inputs.

Since the heat load on the laser crystal slab and the unwanted heat inputs to the system are the same for both symmetrical and asymmetrical cooling cases, only the asymmetrical cooling calculations have been conducted.

A finite element analysis has been performed to obtain the steady-state thermal resistance at the bottom heat sink between the contact surface with the TEC (the hot side) and the surface on which the temperature data is taken. The thermal resistance has been found as 0.95 °C/W. Using this value and the estimated heat discharged on the heat sink using the TEC current-voltage data, the hot side surface of the TEC for asymmetrical cooling has been calculated. The results of the experimental measurements for the asymmetrical cooling are given in Table 5.3. A sample calculation is provided in Appendix D and the experimental error analysis is provided in Appendix E.

Table 5.3 Results of Asymmetrical Cooling Experiments

<b>Diode Supply Current (A)</b>	0.00	15.00	20.00	25.00
<b>Estimated Heat Load on Laser Slab (W)</b>	0.00	4.08	7.14	10.03
<b>Temperature of Second-Stage Holder, Upper, Obtained from Thermal Camera (°C)</b>	15.80	17.00	17.90	18.60
<b>Temperature of Second-Stage Holder, Upper, Obtained from Thermistor (°C)</b>	15.70	16.80	17.50	18.30
<b>Temperature Difference Between Thermistor and Thermal Camera Readings (°C)</b>	0.10	0.20	0.40	0.30
<b>Temperature of Second-Stage Holder, Lower, Obtained from Thermal Camera (°C)</b>	15.60	16.80	18.00	17.20
<b>Temperature of Bottom Heat Sink (°C)</b>	29.00	29.30	30.00	30.70
<b>Laser Output Power (W)</b>	0.00	1.47	4.20	6.92
<b>Calculated TEC Voltage (V)</b>	1.50	4.00	4.70	5.20
<b>TEC Current, Lower (A)</b>	0.80	1.70	2.23	2.92
<b>Heat Discharged by TEC Due to Electrical Conversion (W)</b>	1.20	6.80	10.48	15.18
<b>Total Heat Discharged by TEC to Heat Sink (W)</b>	1.20	10.88	17.62	25.21
<b>Calculated TEC Hot Side Temperature (°C)</b>	30.14	39.64	46.74	54.65
<b>Temperature Difference Between Hot and Cold Sides of TEC (°C)</b>	15.14	24.64	31.74	39.65
<b>Net Heat Discharged from Cold Side of TEC (W)</b>	1.10	5.30	8.50	11.10
<b>Difference Between Heat Discharged by TEC and Estimated Heat Load on Laser Slab (W)</b>	1.10	1.22	1.36	1.07

In the calculation of TEC variables, performance curves of the UT9-12-F2-3030 TEC by Laird which is given in Figure 5.15 have been utilized. Since the current supplied to the TEC and the temperature difference between the hot and cold sides were known, all the operational parameters could be identified.

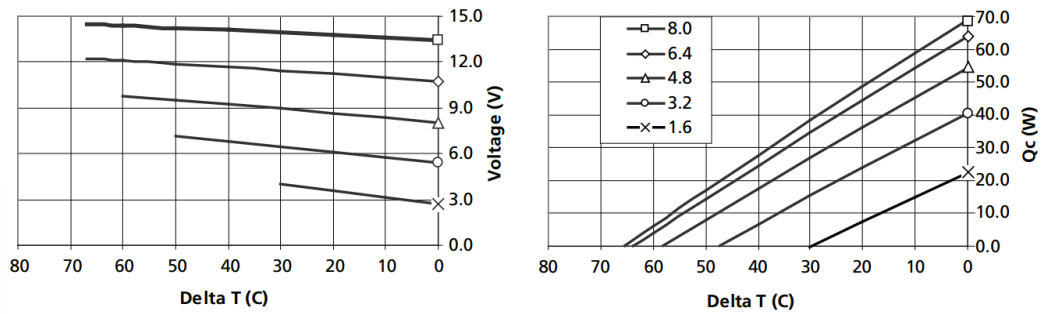


Figure 5.15 The Performance Curves of UT9-12-F2-3030 TEC by Laird [60]

As expected, the heat discharged by the TEC is equal to the estimated heat load on the laser slab plus a nearly constant offset value ranging from 1.07 to 1.36 W. This offset gives the scale of unwanted heat input to the system. The reason of the offset range may be due to calculation and measurement errors since there is no trend of this offset with increasing diode supply power. For the scope of the present study, it can be concluded that the estimated heat load on the laser slab and the heat discharged by the TEC are in good agreement.

As previously mentioned, the simulated heat input to the system was less than 0.5 W. However, the experimental results showed that these inputs were around 1 W. A very good insulator has been used on the assembly surface, and the radiation input was negligible since the assembly was in a plexiglas casing opaque to infrared with the maximum temperature inside the casing being about 30°C. The reason for the increase in the realized heat input value from the expected one is because of increased convection on the outer surface of the assembly due to dry air being pumped into the casing.

### 5.4.3. Laser Beam Profile

To obtain the laser profile, a single wedge has been used to decrease the laser power output on the beam profiler to overcome saturation effects. A part of the laser beam is reflected to the beam profiler as shown in Figure 5.16.

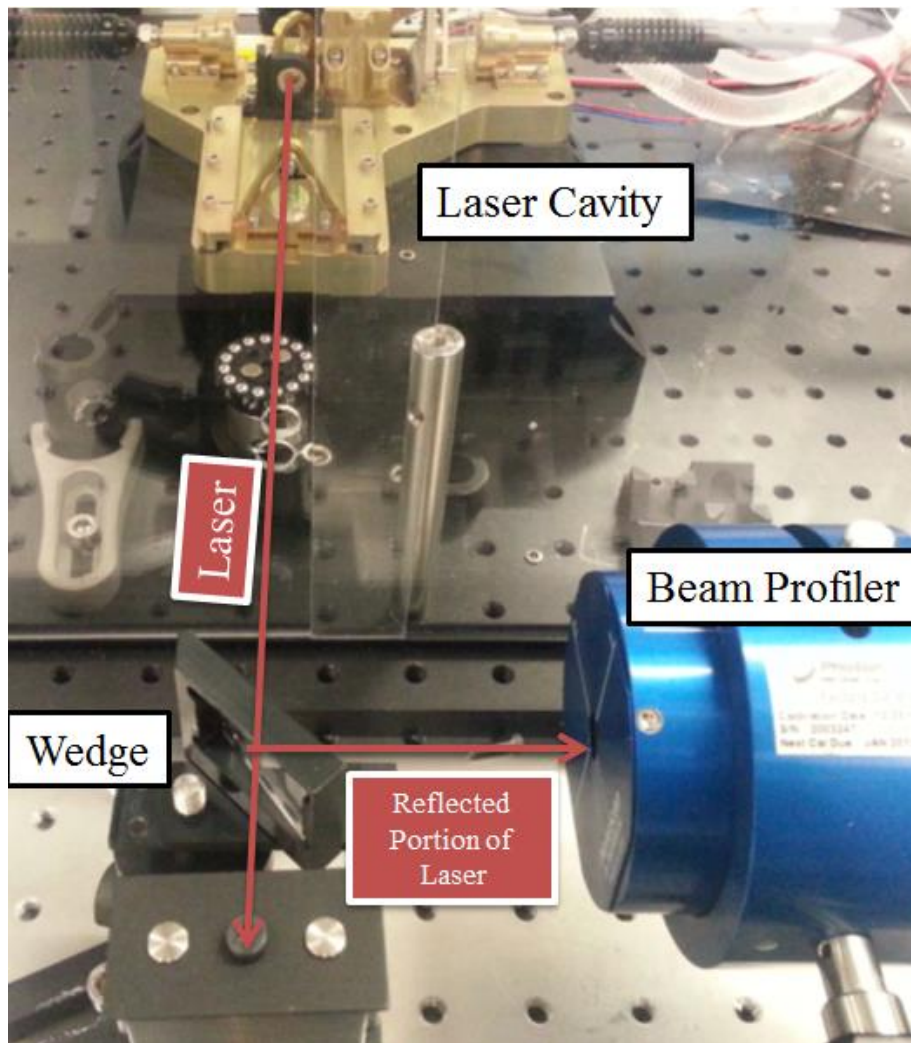


Figure 5.16 Setup for Obtaining the Laser Beam Profile

Since the resonator in this study is a stable spherical resonator structure, the laser is expected to be operating on fundamental traverse mode ( $TEM_{00}$  mode). The fundamental traverse mode is the lowest optical mode of the resonator, which

has Hermite-Gaussian profile. Also, since the laser is end-pumped, only the central region of the laser slab is illuminated by the pump, which excites only the lowest optical mode. Then, the beam profile is expected to be  $TEM_{00}$  (a Hermite-Gaussian Mode) as shown in Figure 5.17. .

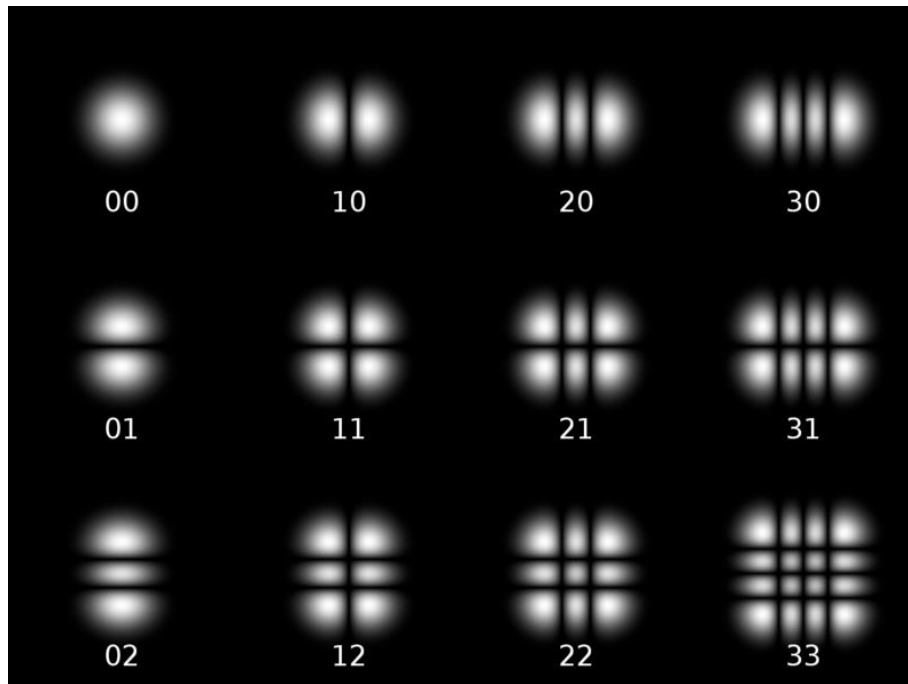


Figure 5.17 Rectangular Traverse Mode Patterns,  $TEM_{mn}$  [61]

The laser beam profiles have been measured for both symmetrical and asymmetrical cooling for a diode supply current of 25 A. This supply current has been selected since the TEC of asymmetrical cooling setup hits the maximum current of the used power supply above 25 A. The laser beam profiles for both symmetry cases are given in Figures 5.18 and 5.19. The beam profiles have been plotted and the beam parameters have been calculated using one hundred samples for each symmetry case.

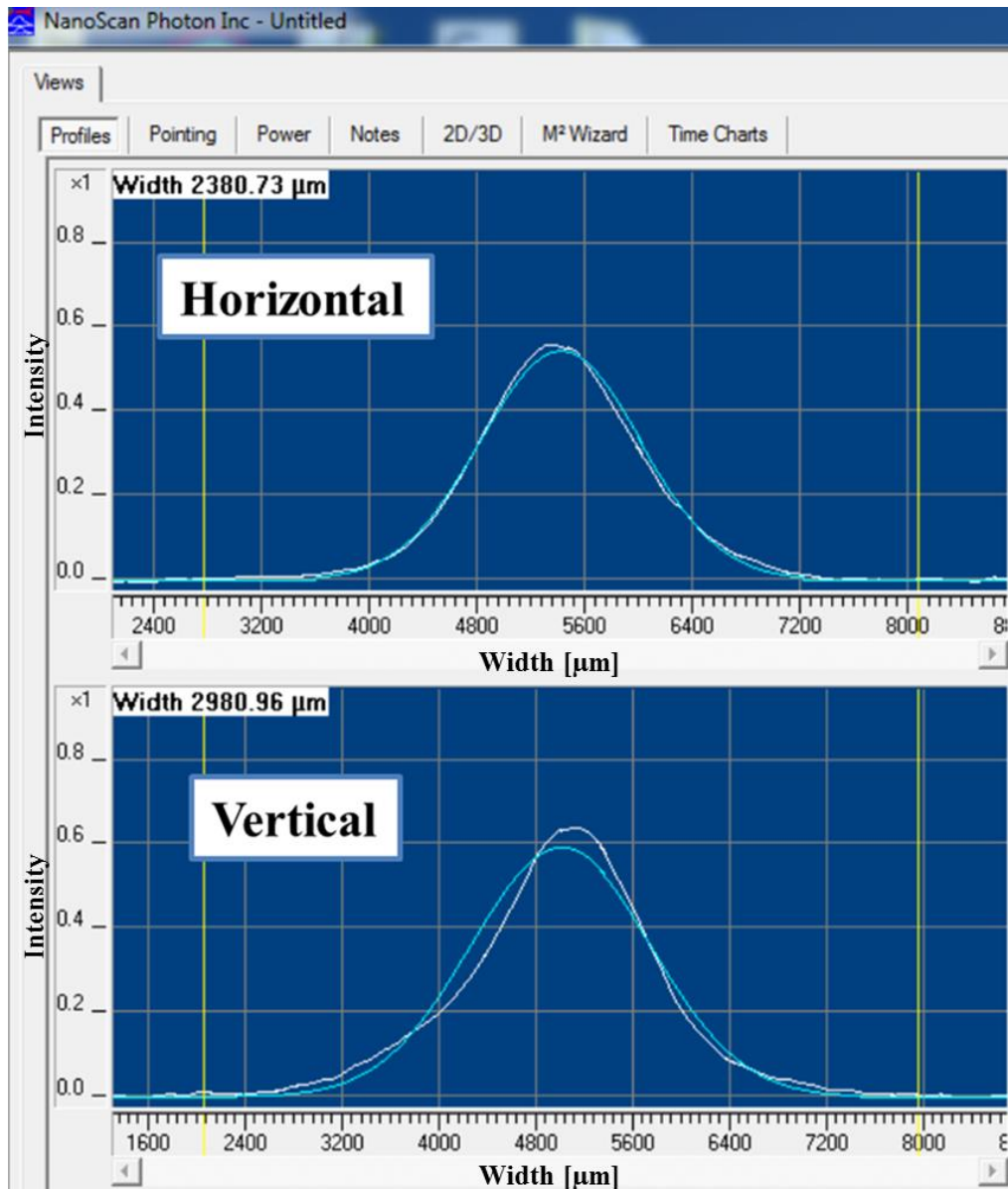


Figure 5.18 Laser Beam Profile for Asymmetrical Cooling with 25 A Diode Supply Current

Both asymmetrical and symmetrical cooling cases yielded very similar laser beam profiles. In both, the vertical and horizontal beam profiles were Hermite-Gaussian. The NanoScan software used with the beam profiler fits a Gaussian profile to the observed profile as may be observed in Figures 5.18 and 5.19.

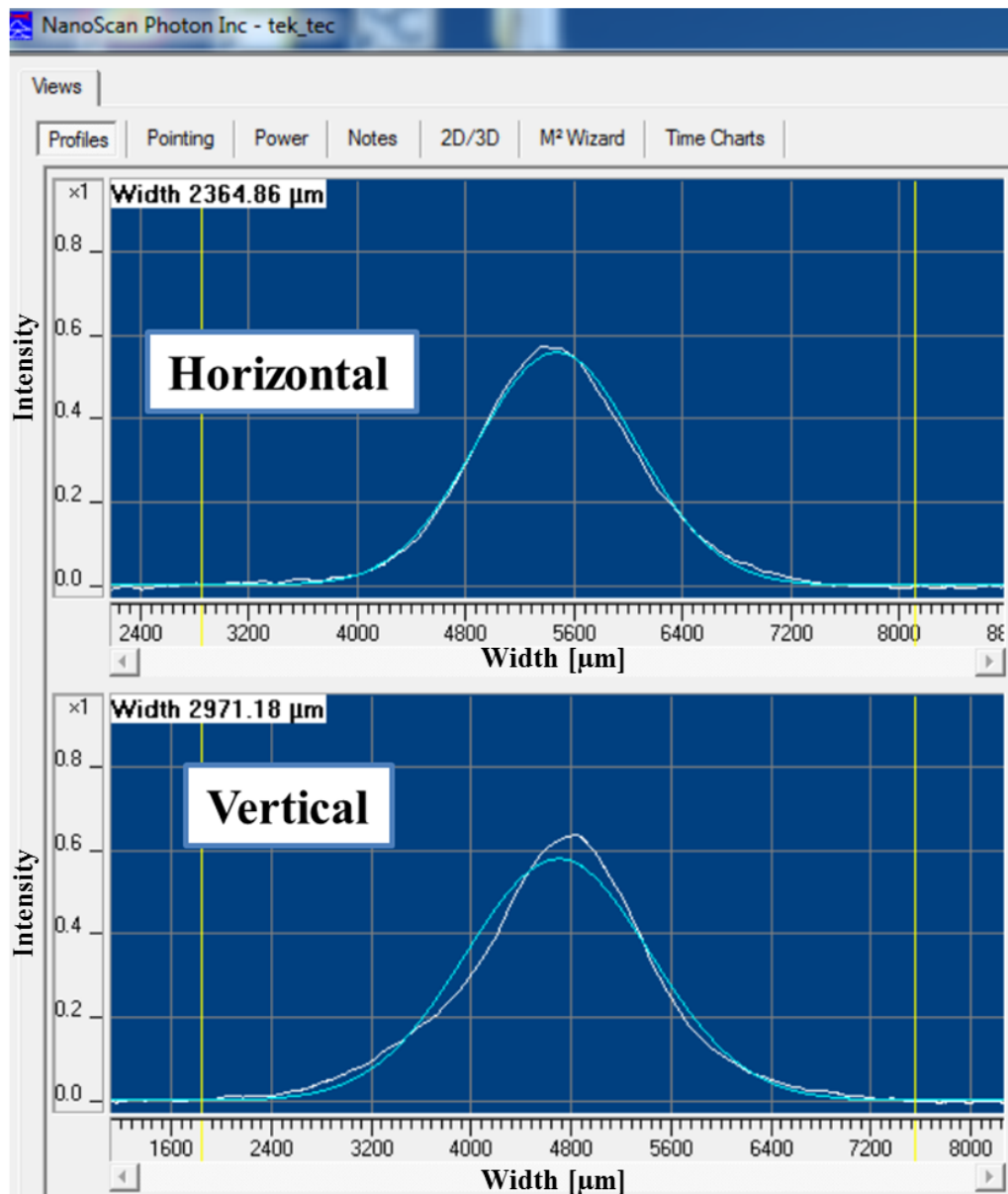


Figure 5.19 Laser Beam Profile for Symmetrical Cooling with 25 A Diode Supply Current

The white profiles represent the experimental data while blue profiles are the least-square Gaussian fits to the experimental data. At first glance, it can be said that symmetrical and asymmetrical cooling provide identical beam profiles and for both cases a negligible shift occurs in vertical beam profiles, while larger

shift is present for horizontal beam profiles. It can be concluded that these shifts are independent of the cooling symmetry.

The other data recorded by the beam profiler is given in Table 5.4. It should be noted that the measurements have been obtained by the beam profiler and the software for each symmetry case by taking one hundred samples of the beam.

Table 5.4 Laser Beam Profile Data for 25 A Diode Supply Current

Parameters	Symmetrical Cooling		Asymmetrical Cooling	
	Horizontal	Vertical	Horizontal	Vertical
<b>13.5% Width (<math>\mu\text{m}</math>)</b>	2370.52	2952.34	2380.6	2977.2
<b>Goodness of Gaussian Fit</b>	0.048	0.018	0.048	0.015
<b>Roughness of Gaussian Fit</b>	0.032	0.08	0.035	0.085

Even though, 13.5%, 10%, 5% and  $D_{4\sigma}$  beam widths have been measured with the beam profile software, only 13.5% beam widths are presented here. For  $\text{TEM}_{00}$  beams, this value yields  $1/e^2$  second moment beam radius. The NanoScan analysis software calculates 13.5% width by a moving-slit beam width analysis, also known as clip-level beam width analysis, which is illustrated in Figure 5.20. Full-width-half-max (FWHM) beam width is another width analysis method, which is not in the scope of the present study. The same procedure is used to determine 10% and 5% beam widths.

The vertical profile 13.5% beam width difference was found to be less than 1% and horizontal profile 13.5% beam width difference was found to be less than 0.5% for symmetric and asymmetric cooling conditions. This points out the fact that the asymmetrical 4-side cooling case yields very similar thermo-optical results as the symmetrical 4-side cooling, just as the simulations predicted.

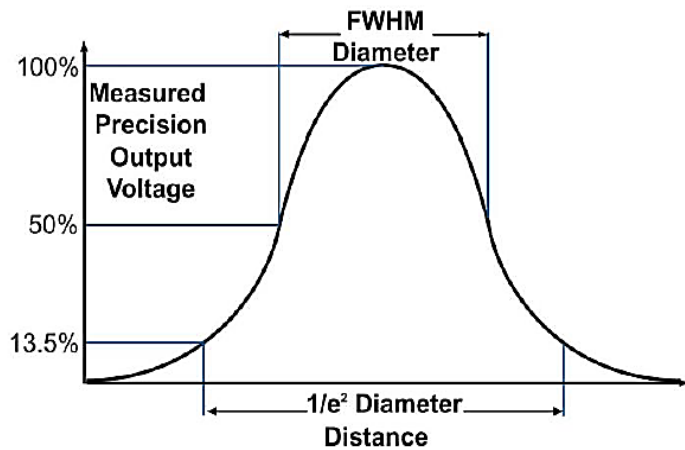


Figure 5.20 Moving-Slit Beam Width Analysis [62]

It was also observed that the beam width of the vertical profile measured by the laser beam profiler was in a good agreement with laser spot size variation simulations. However, the vertical profile width was about 20% higher than the horizontal beam width. The reason behind may be the problems in the precise alignment of the laser cavity. The difference may be decreased by fine tuning the laser resonator alignment. Another factor in this difference may be that one of the pump beams had a small vertical offset from the center axis of the laser slab, which caused thermal effects due to the asymmetrical conditions.

The goodness and roughness of the Gaussian fit have been calculated by the beam profiler software. These parameters provide insight about how good the least-square Gaussian fit is compared to the actual profile. The goodness of Gaussian fit is calculated using summed square of the residuals. A goodness value closer to zero indicates that the Gaussian fit has a smaller random error component, which yields a more useful fit for the predictions. Also it can be concluded that, a smaller goodness value means that the actual profile is closer to Gaussian profile. The data in Table 5.4 points out that the vertical laser beam profiles closer to Gaussian compared to horizontal profiles.

The roughness of the Gaussian fit is equal to the maximum of the ratio of the difference between the actual profile and the Gaussian fit, and the actual profile value at the difference point. The roughness can be taken as a measure of how coarse the laser beam profile was compared to the Gaussian fit. Again, the vertical profile had a higher roughness value than the horizontal profile, which were unaffected by the cooling symmetry.

Another important note in this section is that even though asymmetrical cooling case was planned to be conducted by simply bypassing the upper TEC, the thermal images of the system showed that there were losses due this assembled but electrically bypassed TEC. The upper TEC acted as an energy harvester. Hence, for the asymmetrical cooling, the upper TEC module has been disassembled.

### **5.5. Problems Encountered in the Water Cooled Experimental Setup**

Problems encountered in the cooling water sealing of the laser crystal holders prevented the experimentation of the water cooled system. The cooling water leaked through the contact of the two second-stage laser crystal holders. Even though silicone o-rings were used in the contact surfaces to prevent leakage, the dimensional tolerancing of the second-stage holders were prioritized to obtain uniform pressure distribution on the TIMs used between the first- and the second-stage holders. Therefore, the pressure applied on the sealing o-rings was proved to be insufficient. Tightening the torques on 4 assembly bolts of two second-stage holders above the set value yielded very small impact on the sealing while damaging the TIMs used.

Liquid o-rings have also been used instead of the silicone o-rings. They resulted in blocking the very small cooling channels of 3 mm diameter under the assembly load. This resulted in leakage in the fittings of the water cooling system due to increased pressure drop in the system.

Sealing through the same assembly surface or the same assembly mechanism with crystal holding and cooling water sealing simultaneously proved to be difficult since dimensioning and tolerancing can only be made for prioritizing one aspect. A better way can be to divert the cooling flow outside the holder assembly and use fittings to connect the cooling channels in the crystal holder and the cooling system piping.

Water cooled setup could not be experimented on since a very small water leakage near the laser crystal could have been catastrophic.



## CHAPTER 6

### CONCLUSIONS AND FUTURE RECOMMENDATIONS

#### 6.1. Summary and Conclusions

In this study, a thermal management system for a double end-pumped Tm:YLF laser crystal system has been developed. The objective of the study was to obtain a superior cooling geometry for a square cross-sectioned laser crystal slab in terms of the laser beam quality and efficiency with reduced thermal lensing effect. Simulations have been conducted to determine the thermal and thermo-optical effects on the laser crystal slab for the set pumping architecture. In addition, experiments have been performed to investigate the thermal and thermo-optical effects of the selected cooling geometry.

The first step in the present study was to determine the heat generation on the laser crystal slab due to the absorption of the pump beam. Heat generated through fast-axis ( $z$ -axis) which is also the pump beam propagation axis was determined from the absorptivity of the Tm:YLF laser crystal which is a function of the dopant level of Thulium in YLF host as well as the pumping structure. The heat generation profile on  $xy$ -plane is the profile of a pump beam through the laser crystal. A numerical analysis with ZEMAX software has been conducted to determine the pump incoherent irradiance profile and it was concluded that the illumination profile was between Gaussian and Top-Hat (uniform), closer to the top-hat profile and it was varying through the  $z$ -axis. Thermal analyses have been conducted for both Gaussian and top-hat profiles and the real case was debated to be in between these two results.

The next step was to design conceptual crystal holders for pre-determined cooling geometries. Since the end-surfaces of the laser slab are unavailable as cooling sites due to the presence of the pump and the laser beam, the remaining four side-surfaces were the only potential candidates as the heat discharging surfaces. Considering these four side-surfaces, 1-face cooling that only uses one side-surface for heat discharging, 2-face cooling that uses two parallel opposing side-surfaces, and lastly, 4-face cooling that uses all four side-surfaces have been selected as alternatives for the cooling geometry. The conceptual holder alternatives for these cooling geometries are selected as potential holders while keeping in mind the machinability, the ease of the assembly, the accuracy and the precision required from the assembly, and the cost.

In the third step, a steady-state thermal problem that only involves the laser crystal slab without the holders has been investigated. An analytical solution in the literature for single end-pumped laser crystal slabs with thermal conductivity being inversely proportional to the temperature, and Gaussian heat generation profile have been employed to validate the finite element model in terms of the temperature profiles and the thermal lens radii.

After the validation of the finite element model, the same master mesh system with the same discretization have been used for the thermal simulations of 1-face, 2-face and 4-face cooling of the laser crystal slab for both Gaussian and uniform heat generation profiles. The results indicated that both maximum and average temperatures in the laser crystal slab and the difference between horizontal and vertical temperature profiles decreased as the number of heat discharge surfaces increased. The 4-face cooling alternative has been shown to be superior to the 1-face and 2-face cooling geometries in terms of the thermal and thermo-optical properties.

In the following step, FEM simulations of the composite systems including the crystal slab as well as the cooled crystal holders corresponding to different face cooling cases have been conducted. Aluminum and copper crystal holders have

been used in the simulations. Constant temperature boundary conditions have been applied at the holder surfaces. The temperature profiles of the composite systems have been compared with the face cooling cases where the boundary conditions are applied directly on the crystal surfaces. In addition to the superior properties of the 4-face cooling, 4-side contact cooling crystal holders introduced the minimum thermal resistances to the system, making it more favorable.

In the light of the information obtained through these analyses, 4-side contact cooling case has been selected for the cooling system of the laboratory setup. Thermoelectric cooling modules have been used to obtain constant temperature boundary conditions. In the design of the experimental laser crystal holders, optical and mechanical limitations prevented the realization of the most efficient thermal design. To overcome these limitations, a two-stage crystal holder design has been considered. Even though the distance between the optical path and the cooling surface was larger than that of the conceptual cases, this experimental design outperformed the aluminum conceptual design in the FEM simulations.

A water cooled experimental setup has also been designed with the same architecture. Flow channels have been drilled on the second-stage holders and the convective heat transfer coefficient has been calculated. In addition, a finite element simulation has been performed for obtaining the temperature profiles. The simulation results yielded a very similar temperature profile on the laser crystal slab as that obtained for the TEC case, but the average and maximum temperatures have been lower than those in the TEC case. The reasons for the lower temperatures with water cooling may be stated as (1) the fact that the cooling channels were closer to the laser crystal compared to the surface with TEC application, (2) convection mode of heat transfer dominates solid state cooling.

The next step in the study was the assembly of the experimental holders and the setup. Details of the assembly process, the experimental equipment, remarks on

crystal handling, cleaning of the mechanics and the usage of TIM's have been presented.

The experimental results obtained with the TEC setup indicated a very successful performance of the designed cooling system. Both the symmetric and asymmetric cooling cases yielded very similar results in terms of the laser power output and the beam profile. This result was expected as the simulations also indicated very similar thermal and thermo-optical effects of the asymmetrical and symmetrical cooling cases. The experimental heat load data on the TEC was in good agreement with the expected heat load on the laser crystal by an offset caused by the unwanted heat inputs. The vertical and horizontal beam profiles were both in TEM<sub>00</sub> mode as required, but there was a slight, but noticeable distortion on the vertical profile. This is assumed to be due to the cavity alignment problems and thermo-optical effects caused by one pump being non-coaxial. The asymmetrical cooling in the experimental setup was concluded to be an equivalent cooling option to symmetrical cooling.

To conclude, the present study provided a suitable cooling system design for Tm-YLF laser crystal slabs. The design has been supported by analytical and numerical solutions, as well as by experiments. The simulations showed that for a unity aspect ratio laser crystal slab, 4-side cooling is superior to alternatives in every thermal and thermo-optical aspect. 4-side cooling of laser crystal slab has been realized in an experimental setup that requires precise optics and opto-mechanics with very precise crystal holder in terms of dimensional tolerancing. Also a method has been proposed to estimate the thermal effects of the crystal holder that can be used to improve the analytical and numerical solutions of the thermal problems in the literature considering only laser crystal slabs without holders.

## **6.2. Future Recommendations**

Since the optical design of the laser cavity used in this study was conducted before the thermal analysis, and the present study was initiated to determine the superior cooling geometry for a certain cavity design, all the solutions and comparisons are limited to the system described in the thesis. Different laser crystal slab dimensions with varying pumped zone dimensions may yield improved thermal and thermo-optical performance. A parametric analysis on the laser crystal dimensions and on the pumped zone dimensions may provide a better tool in the design of a double end-pumped laser cavity.

The steady-state thermal analyses have been performed by the approximation of TEC contact surface acting as a constant temperature surface. This may hold true for holders with relatively high thermal conductivity. In reality, however, TECs work in a control setup where the controller of the TEC tries to hold the thermistor feedback in the set temperature. In the most practical cases, the thermistor is placed in or near the body whose temperature is desired to be controlled. In the present work, the thermistor was located in the second-stage holder in close proximity of the first stage holder and near the cooling surface. The temperature profiles obtained from the simulations should be corrected using this information, especially for the holders with low thermal conductivity.

The transient analysis of the real system is very dependent on the controller parameters of the TEC. Simulations here were for an ideal TEC and TEC controller. An analysis including the controller effects and the feedback mechanism may yield different and more accurate results since the analysis done in this study was to obtain only superficial knowledge about the settling time of the system.

The structural analysis to determine the thermal stresses on the laser crystal slab has been conducted in this thesis only for the face cooling cases. An analysis considering a composite system with the crystal and its holder may yield different results depending on the TIMs used, torques applied on the assembly

bolt, assembly structure, temperature profile on the holder and more. Such an analysis can provide valuable information on the effects of the holder and the assembly on the laser crystal slab.

The temperature profile of the end-surfaces of the laser crystal slab may be investigated by isolating a path that filters out the laser beam and the pump wavelength but not the infrared radiation wavelengths caused by the thermal radiation of the end-surfaces from the optical path. A thermal camera, with a suitable lens mounted on this path can detect and show the temperature profile of the end-surface of the laser crystal slab. This will require though a complex coating and expensive optical components.

The offset between the pump beam axis and the central axis of the laser crystal slab prevented the analyses of some results related to the laser beam profile during the experimental study. These effects can be predicted by using a modified finite element model with vertical and horizontal offset on the central axis of the heat generated zone (cylinder). Also in addition to offsetting the heat generated cylinder in the laser crystal slab in the  $x$  and  $y$  coordinates, the axis can be tilted in the  $xz$ -plane and/or  $yz$ -plane.

The water cooled setup could not be experimented due to the water leakage problem. Applying cooling channel sealing and precise assembly of the first-stage holders to second-stage holders proved to be problematic. A water cooled setup can be designed with separate interfaces for sealing and the assembly of the crystal holders to overcome the cooling water sealing problems. Dividing the flow into two outside the holder assembly, and attaching these two separate cooling lines to the two second-stage holders would yield both symmetric water cooling on the first stage coolers and can provide better sealing.

## REFERENCES

- [1] "Laser Guide," [Online]. Available: <http://marketplace.idexop.com/store/SupportDocuments/LaserGuideWEB.pdf>. [Accessed 6 April 2014].
- [2] E. Simpson, "The basic principles of laser technology, uses and safety measures in anaesthesia," *Anaesthesia Tutorial of the Week*, vol. 255, pp. 1-9, 19 March 2012.
- [3] M. M. Tilleman, "Analysis of temperature and thermo-optical properties in optical materials. 1: cylindrical geometry," *Optical Materials*, vol. 33, pp. 48-57, 2010.
- [4] J. M. Eggleston, T. J. Kane, K. Kuhn, J. Unternahrer and R. L. Byer, "The slab geometry laser-part I: theory," *IEEE Journal of Quantum Electronics*, Vols. QE-20, no. 3, pp. 289-301, 1984.
- [5] T. J. Kane, J. M. Eggleston and R. L. Byer, "The slab geometry laser-part II: thermal effects in a finite slab," *IEEE Journal of Quantum Electronics*, Vols. QE-21, no. 8, pp. 1195-1210, 1985.
- [6] M. Karszewski, S. Erhard, T. Rupp and A. Giesen, "Efficient high-power TEM<sub>00</sub> mode operation of diode-pumped Yb:YAG thin disk lasers," *OSA TOPS Advanced Solid State Laser*, vol. 34, pp. 70-77, 2000.

- [7] A. Giesen and J. Speiser, "Fifteen years of work on thin-disk lasers: results and scaling laws," *IEEE Journal of Selected Topics in Quantum Electronics*, vol. 13, no. 3, pp. 598-609, 2007.
- [8] W. Koechner, in *Solid-State Laser Engineering*, 6th ed., New York, Springer, 2006.
- [9] R. Weber, "Cooling schemes for longitudinally diode laser-pumped Nd:YAG rods," *IEEE Journal of Quantum Electronics*, vol. 34, pp. 1046-1053, 1998.
- [10] J. K. Jabczynski, J. Jagus, W. Zendzian and J. Kwiatkowski, "Thermo-optic effects in solid state lasers end-pumped by fiber coupled diodes," *Opto-Electronics Review*, vol. 13, no. 1, pp. 69-74, 2005.
- [11] S. Fan, X. Zhang, Q. Wang, S. Li, S. Ding and F. Su, "More precise determination of thermal lens focal length for end-pumped solid-state lasers," *Opt. Com.*, vol. 266, pp. 620-626, 2006.
- [12] I. Moshe and S. Jackel , "Influence of birefringence-induced bifocusing on optical beams," *J. Opt. Soc. Am. B.*, vol. 22, pp. 1228-1235, 2005.
- [13] I. Moshe, S. Jackel and A. Meir, "Production of radially or azimuthally polarized beams in solid-state lasers and the elimination of thermally induced birefringence effects," *Opt. Lett.*, vol. 28, pp. 807-809, 2003.
- [14] M. S. Roth, E. W. Wyss, H. Glur and H. P. Weber, "Generation of radially polarized beams in a Nd:YAG laser with self-adaptive

overcompensation of the thermal lens," *Opt. Lett.*, vol. 30, pp. 1665-1667, 2005.

- [15] S. Toroghi, M. Aas and A. K. Jafari, "Numerical calculation of temperature-dependent absorption in end pumped Yb:YAG thin disk laser," in *Laser and Fiber-Optical Networks Modeling*, Alushta, Crimea, 2008.
- [16] "Gradient-index Lens," WikipediaWeb, 2007. [Online]. Available: <http://en.wikipedia.org/wiki/File:Grin-lens.png>. [Accessed 1 March 2013].
- [17] B. Bendow, P. D. Gianino, Y. F. Tsay and S. S. Mitra, "Pressure and stress dependence of the refractive index of transparent crystals.," *Appl. Opt.*, vol. 13, no. 10, pp. 2382-96, 1974.
- [18] M. M. Tilleman, "Analysis of thermal effects in laser materials, 2: disk and slab geometry," *Optical Materials*, vol. 33, pp. 363-374, 2011.
- [19] P. Elahi and S. Morshedi, "The double-end-pumped cubic Nd:YVO4 laser: temperature distribution and thermal stress," *Pramana Journal of Physics*, vol. 74, no. 1, pp. 67-74, 2010.
- [20] P. Elahi and S. Morshedi, "Calculation of temperature distribution and thermo-optical effects in double-end-pumped slab laser," *Journal of Engineering Physics and Thermophysics*, vol. 84, no. 6, pp. 1224-1230, 2011.

- [21] F. Huang, N. Jiang, Y. Wang, W. Dong and Y. Niu, "Calculation and comparison of thermal effect in laser diode pumped slab lasers with different pumping structures," SPIE Digital Library, Shijiazhuang, 2008.
- [22] Y. F. Lü, X. H. Zhang, X. D. Yin, J. Xia, A. F. Zhang and J. Q. Lin, "Highly efficient continuous-wave intracavity frequency-doubled Nd:YVO<sub>4</sub>-LBO laser at 457 nm under diode pumping into the emitting level 4F<sub>3/2</sub>," *Appl. Phys. B*, vol. 99, no. 1-2, pp. 115-119, 2010.
- [23] Y. T. Chang, Y. P. Huang, K. W. Su and Y. F. Chen, "Comparison of thermal lensing effects between single-end and double-end diffusion-bonded Nd:YVO<sub>4</sub> crystals for 4F<sub>3/2</sub>→4I<sub>11/2</sub> and 4F<sub>3/2</sub>→4I<sub>13/2</sub> transitions," *Optics Express*, vol. 16, no. 25, pp. 21155-21160, 2008.
- [24] F. Song, C. Zhang, X. Ding, J. Xu and G. Zhang, "Determination of thermal focal length and pumping radius in gain medium in laser-diode-pumped Nd:YVO<sub>4</sub> lasers," *Applied Physics Letters*, vol. 81, no. 12, pp. 2145 - 2147, 2002.
- [25] Y. Ren-Peng, Y. Xin, C. De-Ying, C. Fei, L. Xu-Dong, M. Yu-Fei and Y. Jun-Hua, "The thermal effect in diode-end-pumped continuous-wave 914-nm Nd:YVO<sub>4</sub> laser," *Chin. Phys. B*, vol. 21, no. 2, pp. 1-7, 2012.
- [26] J. Didierjean, E. Hérault, F. Balembois and P. Georges, "ResearchGate," 16 June 2014. [Online]. Available: [http://www.researchgate.net/publication/228720549\\_Comparison\\_of\\_absolute\\_temperature\\_measurements\\_in\\_diode-end-pumped\\_laser\\_crystals\\_with\\_FEA\\_simulations](http://www.researchgate.net/publication/228720549_Comparison_of_absolute_temperature_measurements_in_diode-end-pumped_laser_crystals_with_FEA_simulations). [Accessed 21 June

2014].

- [27] T. Y. Fan, "Heat generation in Nd: YAG and Yb: YAG," *IEEE J. Quantum Electron*, vol. 29, pp. 1457-1459, 1993.
- [28] C. Pfistner, H. P. Weber, S. Merazzi and R. Gruber, "Thermal beam distortions in end-pumped Nd:YAG, Nd: GSGG, and Nd: YLF Rods," *IEEE J. Quantum Electronics*, vol. 30, pp. 1605-1614, 1994.
- [29] M. P. MacDonald, T. Graf, J. E. Balmer and H. P. Weber, "Reducing thermal lensing in diode-pumped laser rods," *Opt. Commun.*, vol. 78, p. 383–393, 2000.
- [30] W. Koechner, "Absorbed pumped power, thermal profile and stresses in a cw pumped Nd:YAG crystal," *Appl.Opt.*, vol. 9, pp. 1429-1434, 1970.
- [31] A. K. Cousins, "Temperature and thermal stress scaling in finite-length endpumped laser rods," *IEEE Journal of Quantum Electronics*, vol. 28, pp. 1057-1069, 1992.
- [32] D. C. Brown, "Ultahigh-average power diode-pumped Nd:YAG and Yb:YAG lasers," *IEEE J. Quantum Electron*, vol. 33, pp. 861-873, 1997.
- [33] M. Sovizi and R. Massudi, "Thermal distribution calculation in diode pumped Nd:YAG rod by boundary element method," *Opt. Laser.Thec.*, vol. 39, pp. 46-52, 2007.

- [34] G. L. Bourdet and H. Yu, "Longitudinal temperature distribution in an endpumped solid-state amplifier medium: application to a high average power diode pumped Yb: YAG thin disk amplifier.," *Appl. Opt.*, vol. 46, pp. 6033-6041, 2007.
- [35] K. Shibib, M. M. Tahir and H. I. Qatta, "Analytical model of transient temperature and thermal stress in continuous wave double-end-pumped laser rod: thermal stress minimization study," *Pramana Journal of Physics*, vol. 79, no. 2, pp. 287-297, 2012.
- [36] U. O. Farrukh, A. M. Buoncristiani and C. E. Byvik, "An analysis of the temperature distribution in finite solid-state laser rods," *IEEE Journal of Quantum Electronics*, vol. 24, pp. 2253-2263, 1988.
- [37] H. Ogilvy, M. J. Withford, P. Dekker and J. A. Piper, "Efficient diode double-end-pumped Nd:YVO<sub>4</sub> laser operating at 1342 nm," *Opt. Express*, vol. 11, no. 19, p. 2411–2415, 2003.
- [38] R. T. Howard, "Even illumination from fiber-optic-coupled laser diodes," *NASA Tech Briefs*, p. 29, October 2006.
- [39] O. Homburg, D. Hauschild, F. Kubacki and V. Lissotschenko, "Efficient beam shaping for high-power laser applications," [Online]. Available: <http://www.limo.de/fileadmin/PDF/limopaper28.pdf>. [Accessed 14 June 2014].
- [40] E. H. Bernhardt, A. Forbes, C. Bollig and M. J. D. Esser, "Estimation of thermal fracture limits in quasi–continuous–wave end–pumped lasers

- through a time-dependent analytical model," *Optics Express*, vol. 16, no. 15, pp. 11115-11123, 2008.
- [41] T. Graf, E. Wyss, M. Roth and H. P. Weber, "Laser resonator with balanced thermal lenses," *Opt. Commun.*, vol. 190, p. 327–331, 2001.
- [42] Y. Ai-Yum, H. Wei, L. Hui-Qing, B. Yong, L. Xue-Chun, G. Ai-Cong, K. Yu-Peng, C. Da-Fu and X. Zu-Yan, "Reducing thermal effect in end-diode-pumped laser crystal by using a novel resonator," *Chin. Phys. Lett.*, vol. 3, p. 607–610, 2005.
- [43] Z. Ma, D. Li, J. Gao, N. We and D. Keming, "Thermal effects of the diode end-pumped Nd:YVO<sub>4</sub> slab," *Opt. Commun.*, vol. 275, pp. 179-185, 2007.
- [44] P. A. Budni, M. L. Lemons, J. R. Mosto and E. P. Chicklis, "High-power/high-brightness diode-pumped 1.9- $\mu\text{m}$  thulium and resonantly pumped 2.1- $\mu\text{m}$  holmium lasers," *IEEE J. Sel. Top. Quantum Electron.*, vol. 6, no. 4, pp. 629 - 635, 2000.
- [45] S. So, J. I. Mackenzie, D. P. Shepherd, W. A. Clarkson, J. G. Betterton and E. K. Gorton, "A power-scaling strategy for longitudinally diode-pumped Tm:YLF lasers," *Applied Physics B*, vol. 84, pp. 389-393, 2006.
- [46] A. Dergachev, K. Wall and P. F. Moulton, "A CW side-pumped Tm:YLF," *OSA Trends in Optics and Photonics*, vol. 68, pp. 343-346, 2002.

- [47] M. Schellhorn, "High-powered diode-pumped Tm:YLF laser," *Applied Physics B*, vol. 91, pp. 71-74, 2008.
- [48] B. M. Walsh, "Review of Tm and Ho materials; spectroscopy and lasers," in *International Laser Physics Workshop*, Trondheim, 2008.
- [49] X. Peng, L. Xu and A. Asundi, "High-power efficient continuous-wave TEM<sub>00</sub> intracavity frequency-doubled diode pumped Nd:YLF laser," *Appl. Opt.*, vol. 44, p. 800–807, 2005.
- [50] R. Paschotta, "Quantum Efficiency," RP Photonics Consulting GmbH, [Online]. Available: [http://www.rp-photonics.com/quantum\\_efficiency.html](http://www.rp-photonics.com/quantum_efficiency.html). [Accessed 14 April 2014].
- [51] V. Ashoori, M. Shayganmanesh and S. Radmard, "Heat generation and removal in solid state lasers," in *An Overview of Heat Transfer Phenomena*, InTech, 2012, pp. 341-376.
- [52] Y. Yüksel, "Thermoelectric cooling of a pulsed mode 1064 nm diode pumped Nd:YAG laser," M.S. thesis, Mech. Eng., METU, Ankara, 2010.
- [53] K. Sezgin, "Pumping chamber design in diode-pumped solid-state lasers for maximum efficiency and minimum optical distortion," M.S. thesis, EE Eng., METU, Ankara, 2013.
- [54] M. Bass and C. DeCusatis, *Optics Vol. 1: Geometrical and Physical Optics, Polarized Light, Components and Instruments*, 3rd ed., New

York: McGraw Hill, 2009.

- [55] B. M. Walsh, *Spectroscopy and excitation dynamics of the trivalent lanthanides Tm(3+) and Ho(3+) in LiYF4*, M.S. Thesis, 1995.
- [56] A. Bejan, *Convection Heat Transfer*, 2nd ed., New York: Wiley, 1995.
- [57] L. F. Moody, "Friction factors for pipe flow," *Transactions of the ASME*, vol. 66, no. 8, pp. 671-684, 1944.
- [58] F. W. Dittus and L. M. K. Boelter, "Heat transfer in automobile radiators of the tubular type," *Univ. Calif. Publ. Eng.*, vol. 2, no. 13, pp. 443-461, 1930.
- [59] V. Gnielinski, "New equations for heat and mass transfer in turbulent pipe and channel flow," *Int. Chem. Eng.*, vol. 16, pp. 359-368, 1976.
- [60] "UltraTEC Series UT8-12-F2-3030 Thermoelectric Module," Laird Technologies, [Online]. Available: <http://www.lairdtech.com/DownloadAsset.aspx?id=3168>. [Accessed 14 June 2014].
- [61] "Hermite-Gaussian Modes," OPI Online Courses, [Online]. Available: [http://www.optique-ingenieur.org/en/courses/OPI\\_ang\\_M01\\_C03/co/Contenu\\_13.html](http://www.optique-ingenieur.org/en/courses/OPI_ang_M01_C03/co/Contenu_13.html). [Accessed 14 June 2014].

- [62] "Ophir-Spiricon Laser Measurement and Beam Profilers," 2013. [Online]. Available: <http://www.ophiropt.com/laser-measurement-instruments/beam-profilers/services/manuals>. [Accessed 21 August 2014].
- [63] M. Sabaieian, H. Nadgaran and L. Mousave, "Analytical solution of the heat equation in a longitudinally pumped cubic solid-state laser," *Applied Optics*, vol. 47, no. 13, pp. 2317-2325, 2008.
- [64] L. A. Pomeranz, P. A. Budni, M. L. Lemons, C. A. Miller, J. R. Mosto, T. M. Pollak and E. P. Chicklis, "Power scaling performance of Tm:YLF and Tm:YALO lasers," *OSA Trends in Optics and Photonics*, vol. 26, p. 458, 1999.

# APPENDIX A

## DATA SHEET OF DIODE PUMPS

M1F2S12-793.2-35C-T25-SS2.13

**DILAS**

The diode laser company.

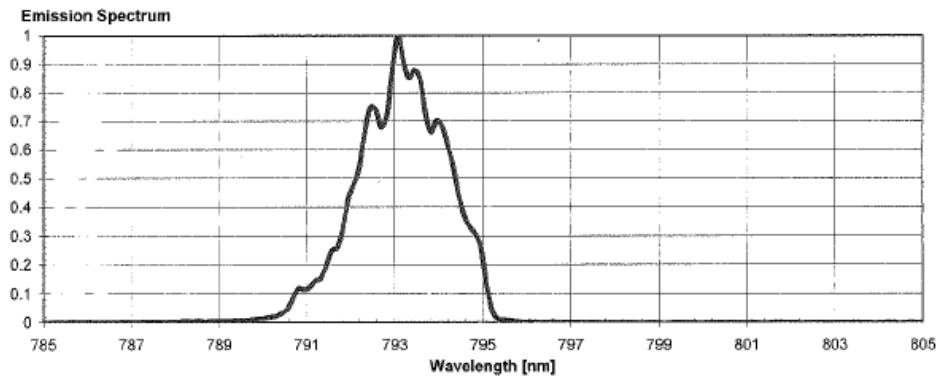
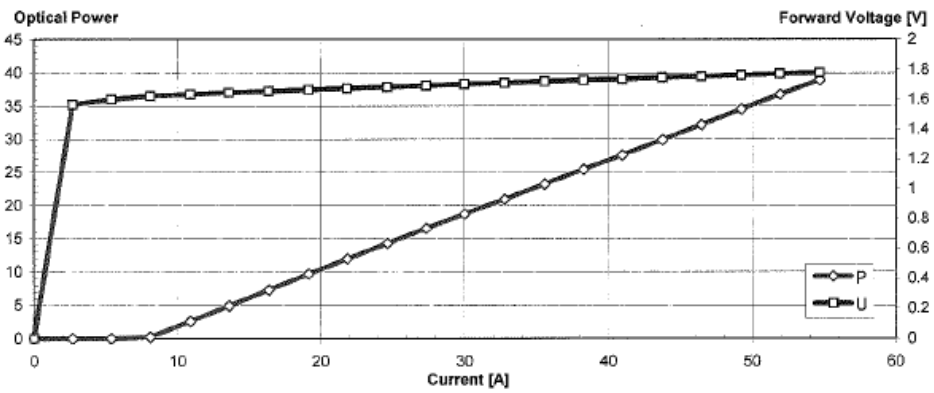
903058

3/15/2013

### Continuous Wave-Operation

Measurement No.: 18201/18911

<b>P (55A)</b>	39.1 W	<b>Central Wavelength</b>	793.4 nm
<b>I (35W)</b>	49.9 A	<b>Peak Wavelength</b>	793.1 nm
<b>Threshold</b>	7.7 A	<b>Line width (FW90%)</b>	3.3 nm
<b>Slope</b>	0.84 W/A	<b>Line width (FWHM)</b>	2.2 nm
<b>Overall Efficiency</b>	39.8 %	<b>Temperature</b>	25.0 °C
<b>Uf</b>	1.8 V	<b>Current</b>	49.8 A
<b>Ue</b>	1.6 V		
<b>Rs</b>	2.8 mOhm		



## APPENDIX B

### INCOHERENT IRRADIANCE PLOTTED IN THE X-AXIS

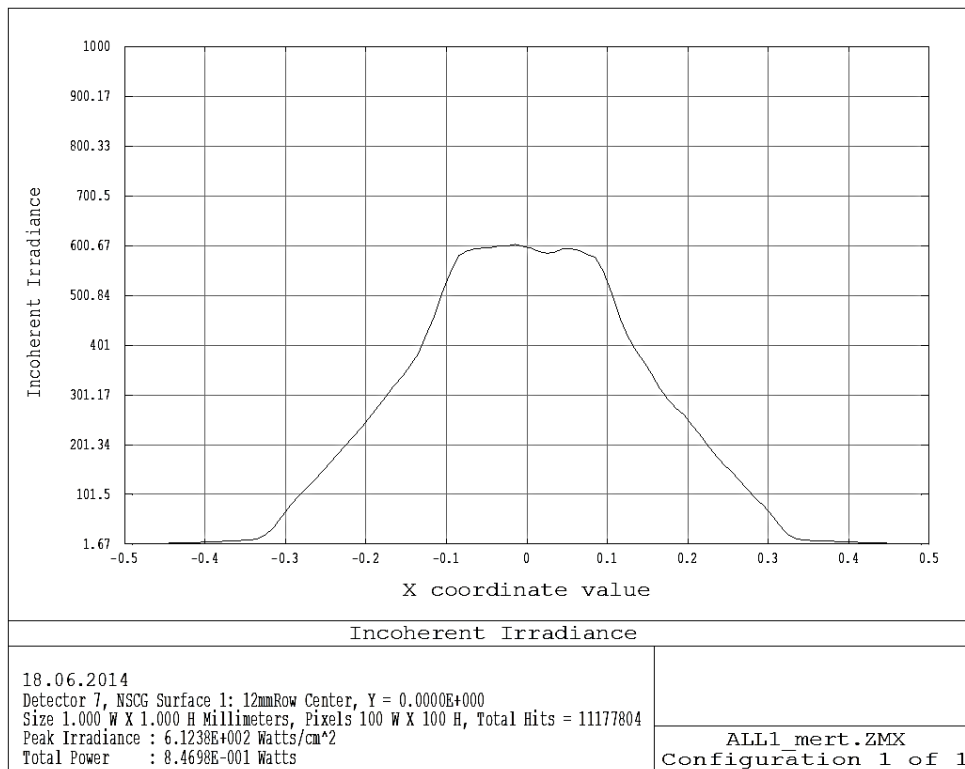


Figure B.1 Incoherent Irradiance on Laser Crystal at the End Surfaces,  $z = 0$  and 12 mm

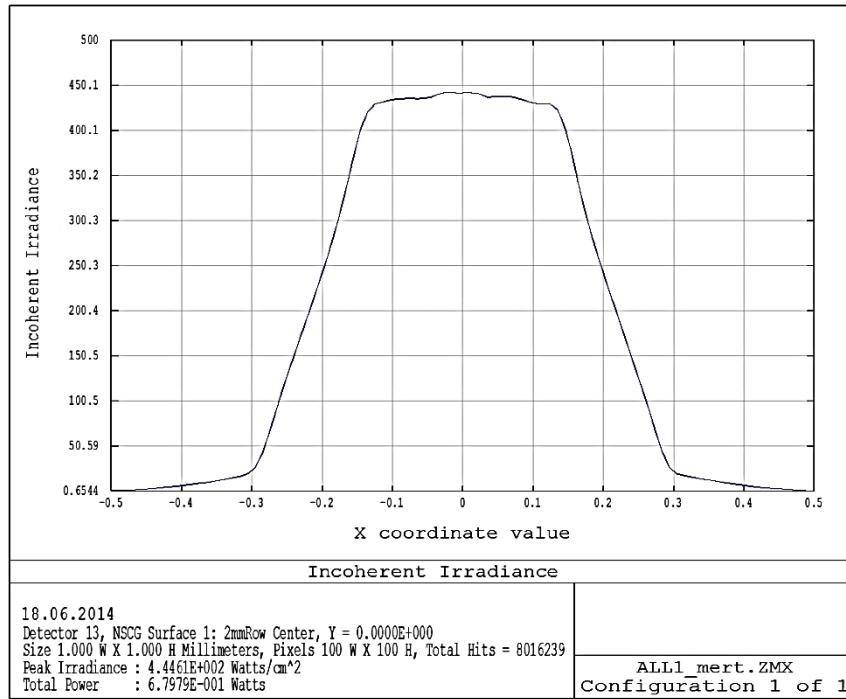


Figure B.2 Incoherent Irradiance on Laser Crystal at  $z = 2$  mm and 10 mm

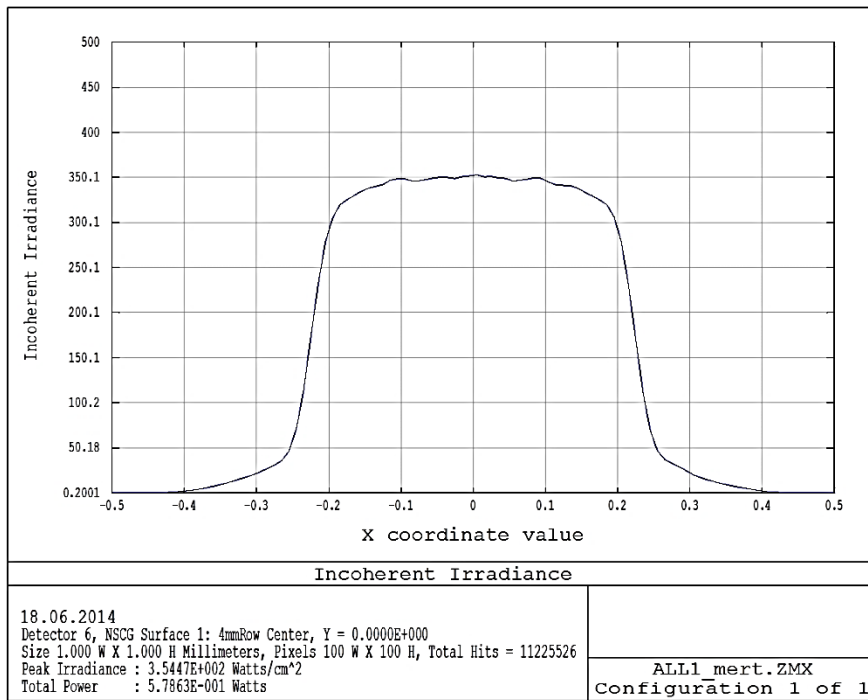


Figure B.3 Incoherent Irradiance on Laser Crystal at  $z = 4$  mm and 8 mm

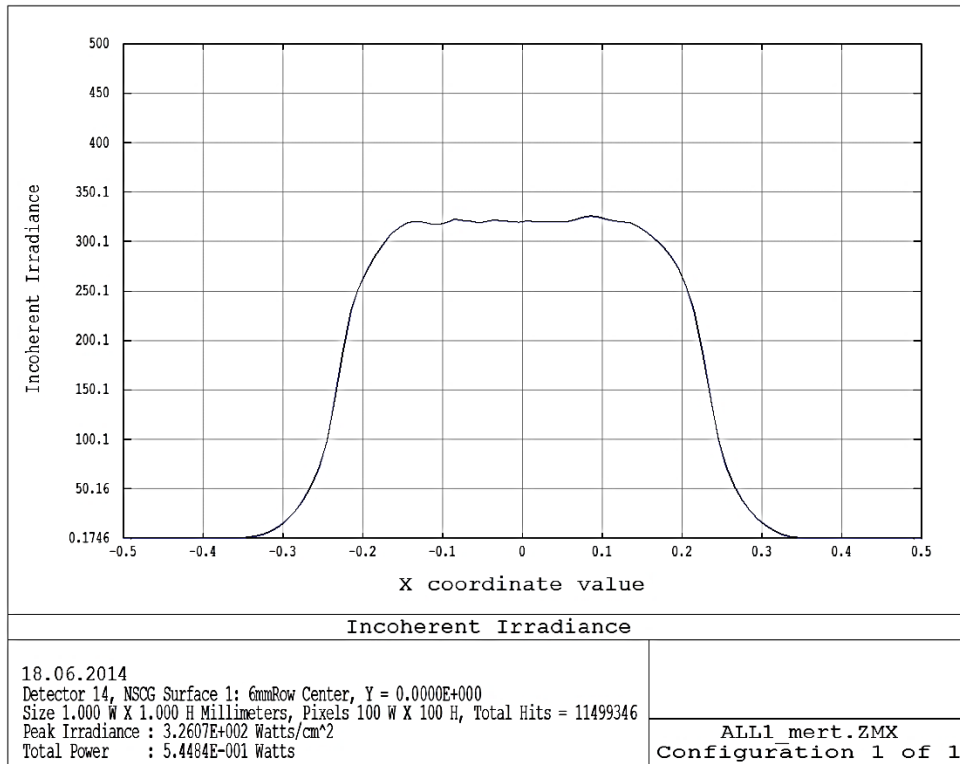


Figure B.4 Incoherent Irradiance on Laser Crystal at the Middle Surface  $z = 6$   
mm

## APPENDIX C

### MATLAB CODE FOR THE ANALYTICAL SOLUTION

```

clc; clear all;
N=15;
teta=0;
Pabs=10/0.43;
alfa=153;
rp=0.36*10^-3;
a=1.5*10^-3;
b=1.5*10^-3;
L=12*10^-3;
k0=6;
T0=300;
K=k0*T0;
zc=0;
z=0;x=0;y=0;
for n=0:N
    pn=(n+0.5)*(pi/a);
    Fn=exp(-(1/8)*(pn*rp)^2)*(erf(a/(sqrt(2)*rp)));
    for k=0:N
        Fn=Fn+exp(-(1/8)*(pn*rp)^2)*((2*sqrt(2)/pi)*(a/rp)*exp(-
(0.5*a/rp)^2)*(exp(-0.25*k^2)/(k^2+2*(a/rp)^2))*(1-
cos(pn*a)*cosh((k*pn*rp)/(2*sqrt(2)))));
    end
    for m=0:N
        qm=(m+0.5)*(pi/b);
        Fm=exp(-(1/8)*(qm*rp)^2)*(erf(b/(sqrt(2)*rp)));
        for k=0:N
            Fm=Fm+exp(-(1/8)*(qm*rp)^2)*((2*sqrt(2)/pi)*(b/rp)*exp(-
(0.5*b/rp)^2)*(exp(-0.25*k^2)/(k^2+2*(b/rp)^2))*(1-
cos(qm*b)*cosh((k*qm*rp)/(2*sqrt(2)))));
        end
        beta=sqrt(pn^2+qm^2);
        teta=teta+(
(0.25*(Pabs*alfa^2*exp(alfa*(zc)))/(a*b*K))/(1-exp(-
alfa*L))*Fn*Fm*cos(pn*x)*cos(qm*y)/(beta*cosh((beta)*L))
)*((alfa^2-beta^2)^-1)*
(cosh((beta)*(L-z))-exp(-alfa*L)*cosh((beta)*z)
- (beta*exp(-
alfa*z)/alfa)*sinh((beta)*L) );
    end
end
(exp(teta)*300)-300

```

## APPENDIX D

### SAMPLE CALCULATION OF THE EXPERIMENTAL RESULTS

A sample of experimental calculations presented in Table 5.3 from the measurements in Table 5.2 for a diode supply current of 20 A is presented here.

Using the optical power vs. supply current data of the diode pump presented in Appendix A, for a diode supply current of 20 A, the optical pumping power of a single diode is 10.5 W. For two identical pump diode systems and the experimental value of the fraction of the absorbed pumping power converted into heat as 0.34, and assuming that the Tm:YLF crystal absorbs all the incident pumping power, the estimated heat load on the laser slab is calculated as

$$Q = 2 \cdot 10.5 \text{ W} \cdot 0.34 = 7.14 \text{ W.} \quad (\text{D.1})$$

A finite element analysis has been conducted to obtain the steady-state thermal resistance for the bottom heat sink between the contact surface with TEC (the hot side surface of the TEC) and the surface at which temperature data were obtained. The thermal resistance has been found as 0.95°C/W. Using this value and the estimated heat discharged to the heat sink with the estimated heat load on the crystal, the temperature of the hot side surface of the TEC (heat sink side) can be calculated.

Since  $Q_C$ , the net heat discharged from the cold side of the TEC, is known and is assumed to be equal to the estimated heat load on the crystal, and since the current supplied to the TEC is also known, the operational point of the TEC can be determined from the performance graphs presented in Figure 5.15. From this

figure, and using  $Q_C$  with the current supplied, the TEC voltage ( $V_{TEC}$ ) is found to be 4.7 V.

Applying the conservation of energy requirement on the TEC at the steady-state operation, the heat discharged to the hot side,  $Q_H$  (heat discharged to the heat sink) is equal to

$$Q_H = Q_C + V_{TEC} \cdot I_{TEC} = (7.14 + 4.7 \cdot 2.23) \text{ W} = 17.62 \text{ W}. \quad (\text{D.2})$$

At this step,  $Q_C$  is considered as an estimated heat load on the laser slab. It should be noted that the expected  $Q_C$  value is a little higher than the estimated heat load on the laser slab by an offset caused by the heat input to the laser slab holder assembly due to natural convection at the surfaces, and heat input from the insulated mounting face of the assembly.

The hot side surface temperature of the TEC ( $T_{Hot-Side}$ ) can be calculated using  $Q_H$ , the temperature measured on the heat sink, and the steady-state thermal resistance between the hot side surface of the TEC and the surface at which the temperature is measured, ( $R_{HS}$ ) as

$$T_{Hot-Side} = (R_{HS} \cdot Q_H) + T_{measured} = (0.95 \cdot 17.62)^\circ\text{C} + 30^\circ\text{C} = 46.74^\circ\text{C}. \quad (\text{D.3})$$

Since the TEC controller sets the cold side temperature to 15°C for all cases, the temperature difference between the hot and cold sides of the TEC can be found by subtracting 15°C from the calculated  $T_{Hot-Side}$  as

$$\Delta T = T_{Hot-Side} - 15^\circ\text{C} = (46.74 - 15)^\circ\text{C} = 31.74^\circ\text{C}. \quad (\text{D.4})$$

Since  $\Delta T$  of the TEC is calculated and the electrical current supplied to the TEC is known, the heat discharged from the cold side of the TEC ( $Q_C$ ) can be found by extrapolating the performance plots given in Figure 5.15. Only certain current values are plotted in  $\Delta T$  vs.  $Q_C$  diagram of Figure 5.15. Hence, interpolation is required. For  $\Delta T = 31^\circ\text{C}$ , the TEC current and the corresponding  $Q_C$  are listed in Table D.1.

Table D.1 Current and Discharged Heat Data for the TEC at 31°C Temperature Difference

<b>Current Supplied to TEC (A)</b>	1.6	3.2	4.8	6.4
<b>Net Heat Discharged from Cold Side of TEC (W)</b>	0	18	26	33

To the data in Table D.1 a third order polynomial can be fitted and the  $Q_C$  value for 2.23 A can be interpolated. The third order polynomial for this case is

$$Q_C(I) = (0.366I^3 - 5.469I^2 + 30.94I - 37) \text{ W}, \quad (\text{D.5})$$

$$Q_C(2.23) = 8.52 \text{ W}. \quad (\text{D.6})$$

## APPENDIX E

### EXPERIMENTAL ERROR ANALYSIS

The accuracy of the sensors used in the experiments was taken from the datasheets provided by the manufacturers. The thermistors are of ANSI Standard Type T with  $\pm 1.0^\circ\text{C}$  (or  $\pm 0.75\%$ ) accuracy. The accuracy of FLIR T335 Thermal Imaging Camera is stated as the greater of  $\pm 2.0^\circ\text{C}$  or  $\pm 2.0\%$  in  $^\circ\text{C}$ .

The Powemax PM150 Energy Sensor has a measurement accuracy of  $\sqrt{U^2 + W^2}$  where  $U$  is the percent calibration accuracy and it is equal to 2.0% for this model.  $W$  is the wavelength accuracy and for 1908 nm it is equal to 2.0%. Using these values the error in Powemax PM150 energy sensor is found to be  $\pm 2.8\%$ .

The power supplies used for diodes and TEC's are calibrated and assumed to have no display errors.

The formulation for the propagation of independent errors are

$$\Delta y = \sqrt{(\Delta x_1)^2 + (\Delta x_2)^2} \quad \text{for } y = x_1 + x_2 \text{ or } y = x_1 - x_2 \quad (\text{E.1})$$

$$\frac{\Delta y}{y} = \sqrt{\left(\frac{\Delta x_1}{x_1}\right)^2 + \left(\frac{\Delta x_2}{x_2}\right)^2} \quad \text{for } y = x_1 x_2 \text{ or } y = x_1/x_2 \quad (\text{E.2})$$

$$\frac{\Delta y}{y} = n \frac{\Delta x}{x} \quad \text{for } y = x^n \quad (\text{E.3})$$

Using the given information, the error analysis for the measured temperature data given in Table 5.3 can be calculated since all the errors are independent. The measurement error values are given in Table E.1.

Table E.1 Temperature Measurement Errors in Asymmetrical Cooling Experiments

Diode Supply Current (A)	0	15	20	25
Temperature of Second-Stage Holder, Upper, Obtained from Thermal Camera (°C)	15.8 ± 2.0	17.0 ± 2.0	17.9 ± 2.0	18.6 ± 2.0
Temperature of Second-Stage Holder, Upper, Obtained from Thermistor (°C)	15.7 ± 1.0	16.8 ± 1.0	17.5 ± 1.0	18.3 ± 1.0
Temperature Difference Between Thermistor and Thermal Camera Readings (°C)	0.1 ± 2.2	0.2 ± 2.2	0.4 ± 2.2	0.3 ± 2.2
Temperature of Second-Stage Holder, Lower, Obtained from Thermal Camera (°C)	15.6 ± 2.0	16.8 ± 2.0	18 ± 2.0	17.2 ± 2.0
Temperature of Bottom Heat Sink (°C)	29 ± 2.0	29.3 ± 2.0	30 ± 2.0	30.7 ± 2.0

From the error analysis presented in Table E.1, it can be seen that the temperature difference between the thermistor and thermal imaging camera readings is within the error limits. All the experimental calculation steps are provided in Appendix D. To calculate the error in the estimated heat load on the laser slab, a 2% data reading error of the performance graph presented in Appendix A for the optical pumping power is assumed. For 20 A diode supply current and using (D.1) and (E.1), the estimated heat load on the laser slab is

$$Q = 2 \cdot (10.5 \pm 0.2) \text{ W} \cdot 0.34 = 7.14 \mp 0.14 \text{ W}. \quad (\text{E.4})$$

The uncertainty in the laser output power was calculated as  $\pm 2.8\%$  previously. For a laser output of 4.20 W, the uncertainty is found as  $\pm 0.12 \text{ W}$ .

The TEC voltage is taken from the TEC performance charts given in Figure 5.15 for the estimated heat load on the laser slab and the current supplied to the TEC. For these performance chart readings the error is assumed to be  $\pm 5.0\%$ . Then the voltage calculation of 4.70 V has an estimated error of  $\pm 0.24$  V.

The formula for the heat discharged by the TEC due to electrical conversion is given in (D.2). By using (E.1) the error for this case becomes

$$Q_{H\_Electrical} = [(4.7 \mp 0.24) \cdot 2.23]W = 10.48 \mp 0.55 \text{ W.} \quad (\text{E.5})$$

Similarly, the error for the total heat discharged to the heat sink is

$$Q_H = (10.48 \mp 0.55) + (7.14 \mp 0.14) = 17.62 \mp 0.57 \text{ W.} \quad (\text{E.6})$$

Using (D.3) and (E.1-2) the error for the hot side surface temperature of the TEC is calculated as

$$T_{HS} = [0.95 \cdot (17.62 \mp 0.57)]^\circ\text{C} + (30 \pm 2.0)^\circ\text{C} = 46.74 \mp 2.07^\circ\text{C.} \quad (\text{E.7})$$

Using (D.4) and (E.1) the error in the temperature difference between the hot and cold sides of the TEC is

$$\Delta T = (46.74 \mp 2.07) - (15.0 \mp 1.0)^\circ\text{C} = 31.74 \mp 2.30^\circ\text{C.} \quad (\text{E.8})$$

From Figure 5.15, it can be observed that  $Q_C$  is a linear function of  $\Delta T$  ( $Q_C = m \cdot \Delta T$ ) for a constant TEC current. For the current values considered, the slope of this function,  $m$  varies between -0.73 and -0.83. A constant slope value of  $m = -0.78$  and an error of 6.4% are considered. By using (E.2), the errors in  $\Delta T$  and  $m$ , and the error for the net heat discharged by TEC may be calculated as

$$\frac{\Delta Q_C}{Q_C} = \sqrt{\left(\frac{2.30}{31.74}\right)^2 + \left(\frac{0.05}{0.78}\right)^2} = 9.7\%, \quad (\text{E.9})$$

$$Q_C = 8.50 \mp 0.82 \text{ W.} \quad (\text{E.10})$$

Using (E.1) the error in the difference between the heat discharged by the TEC and the estimated heat load on the laser slab is

$$Q_{C\_Difference} = (8.50 \mp 0.82) - (7.14 \mp 0.14) = 1.36 \mp 0.83 \quad (\text{E.11})$$

The same procedure is applied to evaluate the uncertainties in all calculations. The results are presented in Table E.2.

Table E.2 Uncertainty in the Results of Asymmetrical Cooling Experiments

<b>Diode Supply Current (A)</b>	0	15	20	25
<b>Estimated Heat Load on Laser Slab (W)</b>	0	4.08 ± 0.08	7.14 ± 0.14	10.03 ± 0.20
<b>Laser Output Power (W)</b>	0	1.47 ± 0.04	4.2 ± 0.12	6.92 ± 0.19
<b>Calculated TEC Voltage (V)</b>	1.5 ± 0.08	4.0 ± 0.20	4.7 ± 0.24	5.2 ± 0.26
<b>Heat Discharged by TEC Due to Electrical Conversion (W)</b>	1.2 ± 0.23	6.8 ± 0.47	10.48 ± 0.55	15.18 ± 0.60
<b>Total Heat Discharged by TEC to Heat Sink (W)</b>	1.2 ± 0.27	10.88 ± 0.49	17.62 ± 0.57	25.21 ± 0.62
<b>Calculated TEC Hot Side Temperature (°C)</b>	30.14 ± 2.01	39.64 ± 2.05	46.74 ± 2.07	54.65 ± 2.08
<b>Temperature Difference Between Hot and Cold Sides of TEC (°C)</b>	15.14 ± 2.25	24.64 ± 2.28	31.74 ± 2.30	39.65 ± 2.31
<b>Net Heat Discharged from Cold Side of TEC (W)</b>	1.1 ± 0.1	5.3 ± 0.5	8.5 ± 0.8	11.1 ± 1.1
<b>Difference Between Heat Discharged by TEC and Estimated Heat Load on Laser Slab (W)</b>	1.1 ± 0.1	1.22 ± 0.50	1.36 ± 0.83	1.07 ± 1.13

It should be noted that the variation of the difference between the heat discharged by the TEC and the estimated heat load on the laser slab is well within the error limits.